NANO/BIOSENSORS BASED ON LARGE-AREA GRAPHENE

Pedro Ducos Ruiz

A DISSERTATION

in

Physics and Astronomy

Presented to the Faculties of the University of Pennsylvania in
Partial Fulfillment of the Requirements for the
Degree of Doctor of Philosophy
2017

Supervisor of Dissertation	Graduate Group Chairperson
_____	_____
Alan T. Johnson Professor of Physics	Ravi Sheth Professor of Physics

Dissertation Committee:

Cherrie Kagan
Committee Chair
Professor of Electrical and Systems Engineering

Marija Drnric Professor of Physics	Jay Kikkawa Professor of Physics	Justin Khoury Professor of Physics

LARGE AREA GRAPHENE BASED NANO/BIO HYBRID DEVICES FOR SENSING APPLICATIONS

To family; the one that is still here, the one that is gone, and the one that is to come.

ACKNOWLEDGEMENTS

It is my pleasure to acknowledge here all those who were instrumental in my doctoral education.

First and foremost, I would like to thank my advisor, Prof. Charlie Johnson, for his continued support and guidance throughout my research career. He granted me a great deal of freedom to fully experiment and pursue my research interests. He helped me grow from a physics student to a scientist gaining the necessary confidence in the process. During the time, I have spent at the University of Pennsylvania, both during my Master and my Doctoral degrees, I acquired knowledge and wisdom that will inform my decisions for many years.

Second, I would like to acknowledge all my collaborators and lab mates. My first mentor, Dr. Mitch Lerner. He taught me how to properly do day-to-day lab work and started me on the research path that led me to continue to a doctoral degree after my Masters. From him I started on nanofabrication, graphene transistors and antibody sensors. Dr. Matthew Robinson formerly at Fox Chase Cancer Center for providing state-of-the-art biomaterials. Dr. Gang Hee Han for his guidance on graphene growth, large scale graphene sheets of excellent quality would have never been possible without his tutelage. Dr. Madeline Diaz who worked together with me on antibody detection sensors, her expertise in chemistry made the process much easier. Dr. Zhaoli Gao, who helped me overcome the problems for multiplexing

detection of Lyme disease. Dr. Dustin Brisson and Dr. Damien Lekkas for their collaboration during the Lyme disease project. Dr. Nick Kybert and Carl Naylor, for their continued humor, support, and friendship without which the experience would have been a lot less enjoyable. As well as all other members from the Johnson group through the years Ramya Vishnubhotla, Chris Kehayas, Jingley Ping, John Qi, Sung Ju Hong, Ali Esfandiar, Rajatesh Guidibande, Jeremy Yodh, Alex Crook, and Ryan Mendoza, I was very lucky to share a room with some of the most talented people I have ever met. Finally, undergraduates that and master's students I had the privilege of mentoring Yichen Lu, Jonathan Zauberman, Jahnelle Jordan, Rodrigo Rodriguez, and Ashwin Amurthur.

I would like to thank as well those at Penn and Philadelphia who made my time here much more enjoyable. The Latin American contingent, Santiago Segarra, Santiago Paternain, Fernando Gama, and Andrea Contigniani. The Philadelphia Gryphons Rugby club, for their friendship and support on and off the field, specially to Anthony Chieco for almost forcing me to try out Rugby. And, all my classmates that got me through long studying nights during both my Master's and Doctoral degrees.

I want to thank my parents Dr. Monica Ruiz and Pedro Ducos Andrade without their support none of this would have been possible. My grandfather Atahualpa who always was my greatest inspiration, I would have never started in the sciences without him. My brother Pablo, for always believing in me even when

I didn’t do so myself. Finally, I want to thank my future wife, Amy, the source of my drive and my strength. You got me through the finish line, I have more to thank you than you will ever know.

ABSTRACT

NANO/BIOSENSORS BASED ON LARGE-AREA GRAPHENE

Pedro Ducos

A.T. Charlie Johnson

Two dimensional materials have properties that make them ideal for applications in chemical and biomolecular sensing. Their high surface/volume ratio implies that all atoms are exposed to the environment, in contrast to three dimensional materials with most atoms shielded from interactions inside the bulk. Graphene additionally has an extremely high carrier mobility, even at ambient temperature and pressure, which makes it ideal as a transduction device. The work presented in this thesis describes large-scale fabrication of Graphene Field Effect Transistors (GFETs), their physical and chemical characterization, and their application as biomolecular sensors. Initially, work was focused on developing an easily scalable fabrication process. A large-area graphene growth, transfer and photolithography process was developed that allowed the scaling of production of devices from a few devices per single transfer in a chip, to over a thousand devices per transfer in a full wafer of fabrication. Two approaches to biomolecules sensing were then investigated, through nanoparticles and through chemical linkers.

Gold and platinum Nanoparticles were used as intermediary agents to immobilize a biomolecule. First, gold nanoparticles were monodispersed and

functionalized with thiolated probe DNA to yield DNA biosensors with a detection limit of 1 nM and high specificity against noncomplementary DNA. Second, devices are modified with platinum nanoparticles and functionalized with thiolated genetically engineered scFv HER3 antibodies to realize a HER3 biosensor. Sensors retain the high affinity from the scFv fragment and show a detection limit of 300 pM.

We then show covalent and non-covalent chemical linkers between graphene and antibodies. The chemical linker 1-pyrenebutanoic acid succinimidyl ester (pyrene) stacks to the graphene by Van der Waals interaction, being a completely non-covalent interaction. The linker 4-Azide-2,3,5,6-tetrafluorobenzoic acid, succinimidyl ester (azide) is a photoactivated perfluorophenyl azide that covalently binds to graphene. A comparison is shown for genetically engineered scFv HER3 antibodies and show a low detection limit of 10 nM and 100 pM for the pyrene and azide, respectively. Finally, we use the azide linker to demonstrate a large-scale fabrication of a multiplexed array for Lyme disease. Simultaneous detection of a mixture of two target proteins of the Lyme disease bacterium (*Borrelia burgdorferi*), this is done by separating the antibodies corresponding to each target in the mixture to different regions of the chip. We show we can differentiate concentrations of the two targets.

TABLE OF CONTENTS

ACKNOWLEDGEMENTS iv

ABSTRACT vii

LIST OF FIGURES xiii

1 OVERVIEW 1

2 INTRODUCTION TO GRAPHENE AND BIOMOLECULES 5

2.1 GRAPHENE 5

2.1.1 Band Structure of Graphene 7

2.1.2 Graphene Field Effect Transistors 9

2.1.3 Carrier Density 10

2.1.4 Dirac Voltage 11

2.1.5 Carrier Mobility 12

2.1.6 Contact Resistance 14

2.2 BIOMOLECULES 17

2.2.1 Immunoglobulins 18

2.2.2 Deoxyribonucleic Acid 20

2.2.3 Hill-Langmuir Model 21

2.2.4 NHS ester/Amine Chemistry 23

2.3 SUMMARY 24

3 EXPERIMENTAL METHODS 25

3.1 CHARACTERIZATION METHODS 25

3.1.1 Electrical Measurement 25

3.1.2 Atomic Force Microscope 27
3.1.3 Scanning Electron Microscope 29
3.1.4 X-Ray Photoelectron Spectroscopy 30
3.1.5 Raman Spectroscopy 32
3.2 GRAPHENE PROCESSING 34
3.2.1 Chemical Vapor Deposition 34
3.2.2 Electrolysis Driven Transfer 38
3.3 FABRICATION METHODS 40
3.3.1 Laser Lithography 40
3.3.2 Photolithography 42
3.3.3 Physical Vapor Deposition 43
3.3.4 Reactive Ion Etching 45
3.3.5 Annealing 46
3.4 FUNCTIONALIZATION 48
3.4.1 Azide Functionalization 48
3.4.2 Pyrene Functionalization 49
3.4.3 Nanoparticle Mediated Functionalization 50
3.5 SENSING 52
3.6 SUMMARY 53
4 NANOPARTICLE BASED SENSORS 54
4.1 INTRODUCTION 55
4.2 MONODISPERSE GOLD NP MODIFIED GFET FOUR PROBE ARRAYS FOR ssDNA DETECTION 56

4.2.1 Abstract 56
4.2.2 Introduction 56
4.2.3 Materials and Methods 57
4.2.4 Results and Discussion 62
4.2.5 Conclusion 71
4.3 PLATINUM NP MODIFIED NANOHYBRID GFET ARRAY FOR THE DETECTION OF BREAST CANCER BIOMARKER 72
4.3.1 Abstract 72
4.3.2 Introduction 73
4.3.3 Results and Discussion 75
4.3.4 Conclusion 85
4.3.5 Experimental Section 86
4.4 SUMMARY 88
5 ANTIBODY/ANTIGEN BIOSENSORS 89
5.1 INTRODUCTION 90
5.2 COVALENT/NONCOVALENT FUNCTIONALIZATION OF GFET ARRAYS FOR BREAST CANCER BIOMARKER DETECTION 91
5.2.1 Abstract 91
5.2.2 Introduction 92
5.2.3 Methods 94
5.2.4 Results and Discussion 96
5.2.5 Conclusion 103

5.3 SENSOR FABRICATION FOR MULTIPLEXED DETECTION OF LYME DISEASE BIOMARKER PROTEINS 104
5.3.1 Abstract 104
5.3.2 Introduction 104
5.3.3 Methods 107
5.3.4 AFM, Raman Spectroscopy, and Electrical Measurement: 110
5.3.5 Results 112
5.3.6 Conclusion 119
5.4 SUMMARY 120
6 CONCLUSIONS 121
6.1 SUMMARY 121
6.2 RESEARCH PROSPECTS 125
6.2.1 Monodisperse Nanoparticles 125
6.2.2 Linker Density 130
6.2.3 Engineered Biomolecules 133
6.2.4 On-Chip Processing 136
A. APPENDIX: RECIPES 137
A.1. GRAPHENE GROWTH 137
A.2. METALIZATION PHOTOLITHOGRAPHY 138
A.3. GRAPHENE PHOTOLITHOGRAPHY 140
A.4. CHEMICAL LINKERS 141
A.5. PROTEIN IMMOBILIZATION 142
BIBLIOGRAPHY 144

LIST OF FIGURES

Figure 2.1: (a) Bravais lattice of graphene with unit cell (dashed line) and primitive vectors a1 and $a2$. Carbon atoms i and j_1 are the atom basis. Atoms j_n are first and second nearest neighbors of atom i. (b) Brillouin zone for the reciprocal lattice with primitive vectors $b1$ and $b2$. K and K′ are the irreducible wave vector points in the Brillouin zone, Γ and M represent significant wave vectors in the reciprocal space.[13] 6

Figure 2.2: (a) Calculated dispersion for graphene in the Brillouin zone. This is the solution to a first order tight-binding model. In red, the Fermi Energy level. The valence and conduction band are below and above the Fermi level, respectively. (b) Projection of the dispersion along the wave vector path K → Γ → M → K.[1-3] .. 8

Figure 2.3: Schematic of a Graphene Field Effect Transistor (GFET). Indicated are the three terminals source, drain and gate. The channel is separated from the gate by an insulating layer. A bias voltage is applied to measure the current through the channel, this current changes with carrier density which is a function of the gate voltage. 9

Figure 2.4: Dispersion around the Dirac Cone for graphene. (a) Depleted electrons, are taken from the valence band (b) Neutrality point, electrns occupy states up to the fermi level. (c) Injected electrons, are placed on the conduction band. 11

Figure 2.5: (a) Pinning effect of a graphene-metal contact, the Dirac cone has shifted from the fermi energy (E_F) to now match the work function difference. (b) Doping effect near the edge between the exposed and the unexposed graphene. Pinned and unpinned Dirac cones are shown as well as the depletion region (L_B). (c) p-n junction of the around the graphene edge. Once the Fermi level increases enough (by increasing the gate voltage) both Dirac cones can be n conducting forming an n-n region. Similarly, for decreasing Fermi level forming the p-p junction.[6] 15

Figure 2.6: Contact resistance as a function of gate voltage for several metals. Insert shows the layout of the experiment.[6] 16

Figure 2.7: Computer generated immunoglobulin. Annotated the two different chains of the antibody and the binding regions.[4] 19

Figure 2.8: Computer generated image of a Deoxyribonucleic Acid (DNA) structure. T-A and C-G base pairs are highlighted.[5] 20

Figure 2.9: NHS ester/Amine reaction. Reaction is optimal close to neutral pH. Amide bond is formed and a hydroxysuccinimide are released.[7] 23

Figure 3.1: Connection schematic for electrical characterization of GFETs for (a) two-probe configuration, V_g is gate voltage, V_b is the bias voltage, and I is the measured current (b) four-probe configuration, V_g is gate voltage, I_b is the bias current, and V is the measured voltage. 26

Figure 3.2: Parallel electrical characterization setup. Two Keithley source meters, a probe card, a switching matrix, the probe station, and a controller computer are shown. 27

Figure 3.3: Diagram of AFM operation. Piezoelectric sensor controls the oscillation, movement in the horizontal plane and the height. A feedback loop keeps the measured force constant. 28

Figure 3.4: (a) Schematic of a Scanning Electron Microscope. Electron gun generates the stream of electrons; a series of electromagnetic condensers and apertures focus the beam to a small point on the sample. The whole system is under vacuum. (b) SEM image of an AFM tip.[2-3] 30

Figure 3.5: Diagram of XPS operation. An X-ray beam shines to the sample and excites photoelectrons that are detected. The measured energy spectra of the photoelectrons depends on the sample composition. 31

Figure 3.6: (a) Diagram of the graphene furnace used. MFC controllers are used to regulate the gas flow into the chamber. A vacuum pump maintains low pressure in the chamber and helps to remove reaction by-products. Methane gas is used as a precursor, Hydrogen gas as a regulator and Argon gas as a carrier. (b) Diagram of the growth recipe. Argon flow in blue, hydrogen flow in red, methane flow in black. Temperature profile in orange. (c) Picture of a copper foil with monolayer graphene as grown. Water droplets can easily form on the surface due to its hydrophobicity. 36

Figure 3.7: (a) SEM image of large scale graphene recipes. Inserts show a zoomed image of the same sample. Parameters as used for smaller scale growth (left), and after optimizing parameters (right) (b) Raman spectra for the unoptimized (left) and optimized (right) recipes. Peaks are normalized with the G peak, and have the same vertical scale. 38

Figure 3.8: Schematic for electrolysis driven transfer. Copper foil is spin coated with PMMA. A bias is applied between the foil and a metal anode, that generates bubbles that mechanically separate the Graphene/PMMA from the copper foil. A substrate is used to scoop the Graphene/PMMA and acetone is used to remove the PMMA. 39

Figure 3.9: Schematic of the photolithography process (a) for a wafer to print an array of metal contacts to define the GFET source/drain (b) wafer after metallization, treatment and graphene transfer to define the GFET channel. 43

Figure 3.10: Process for electrode metalization. Wafer with resist after photolithography is placed on the chamber and a layer of Cr/Au is evaporated. The resist is cleaned by an appropriate solvent to remove excess metal from the depositon. 44

Figure 3.11: Reactive Ion Etching process. Wafer after graphene transfer and photolithography is exposed to oxygen plasma. Graphene is removed by plasma ions on the uncovered regions. Lift-Off removes the resist and leaves the graphene channel exposed. 46

Figure 3.12: XPS Spectra of PMMA-transferred CVD graphene: (a) before annealing, and after annealing at (b) 200ºC, (c) 250ºC (d) 300ºC. The binding energy of the sp^2 carbon bonds (gray) is asigned at 284.4 eV for all curves. Other chemical shifts are atributed to the carbons in the PMMA structure (red, blue, green) respectively.[10] 47

Figure 3.13: Diagram of an annealing furnace. A chip (or set of chips) are loaded into the tube chamber, close to the center of the heating zone. A constant flow of 1000 sccm Ar and 250 sccm H2 is applied. The furnace is heated to 225oC and the samples are annealed for 1 hour. 48

Figure 3.14: (top) Light (or thermal) activated decomposition of an Azide to a Nitrene (bottom) Cycloaddition of Nitrene onto graphene to form a covalent bond.[8] 49

Figure 3.15: AB π-π stacking of a pyrene molecule with graphene. The interaction is similar to the interlayer stacking of graphene sheets..... 50

Figure 3.16: Density Functional Theory (DFT) computations for the noble metal – thiol complex bonding, for copper (left), silver (middle) and gold (right). All show some degree of covalence, copper is most polarized and gold is least polarized.[9] 51

Figure 3.17: (a) Electrical response of a single GFET array. Resistance is measured as a function of gate voltage. (b) Dirac voltage, and (c) mobility; of all devices fabricated in a wafer calculated by mathematical modelling. 52

Figure 4.1: (a) Schematic showing the AuNp-GFET fabrication process. A gold layer is deposited onto CVD graphene. The gold-graphene layer is coated with PMMA and transferred. GFET channels are patterned using photolithography followed by oxygen plasma etching. Finally, the photoresist is removed, and the array is annealed to form AuNPs on the graphene. (b) Schematic of the four-probe conductivity-gate voltage measurement set up. (c) Optical micrograph showing an individual four-probed GFET device. Inset: Optical image of a chip with 24 Au-GFET devices. (d) Optical image of a 4-inch wafer with 9 electrode arrays and a transferred graphene monolayer that covers the full region defined by the arrays (dashed line). 61

Figure 4.2: Measurements of photoresist contamination on graphene after photolithographic processing. (a) AFM images of the Gr-FET surface after photolithography and thermal annealing. The bilayer process results in low surface contamination (top image), and single layer process leaves significant residue on the surface (bottom image). Scale bar is 100 nm. Vertical color scale is 5 nm. (b) σ-Vg curve of Gr-FETs fabricated using and a single layer (red). (c-d) XPS spectra of the C1s regions for the samples processed using PMGI/S1813 (panel c) and S1813 (panel d). Both spectra are normalized to Peak 1. Peaks 2-4 are significantly reduced

in the spectrum from the sample processed using PMGI/S1813, indicating a lower level of chemical contamination. 63

Figure 4.3: (a) SEM image of graphene after thermal evaporation of a gold layer shows the formation of small (~2 Å thick) Au clusters. (b) SEM image showing the four-probe AuNP-GFET, where gold electrodes contact the graphene from below. (c) SEM image of the highlighted area in (b), showing a uniform distribution of AuNPs. The number density is approximately 400/μm2, consistent with the AFM characterization 66

Figure 4.4: (left) Raman spectrum of graphene after photolithographic processing using bilayer PMGI/S1813. (right) Raman spectrum of AuNP-Gr hybrid layer after bubble transfer onto the SiO2 substrate and thermal annealing. 66

Figure 4.5: (a) AFM image showing the formation of uniform AuNPs on graphene after annealing. The corresponding AFM line scan is shown below the AFM image. (b) AuNP size distribution. The AuNP diameter is 5.3 ± 1.2 nm. Histograms of (c) hole mobility and (d) Dirac voltage with Gaussian fits (black curve) of AuNP-Gr-FETs based on three separate arrays, with 24 devices each. . 67

Figure 4.6: (a) Schematic of the AuNP-GFET DNA biosensor. (b) σ-Vg curves after chemical functionalization and exposure to target cDNA. After functionalization with probe DNA and Tween-20 blocker, exposure to 100 nM cDNA leads to a Dirac voltage shift of 13.6 V (green to red). (c) Sensor response as a function of cDNA concentration. The limit of detection is 1 nM. 69

Figure 4.7: Schematic representation of fabrication process for an array of 52 GFETs. Metallization of contacts is done through photolithography patterning and a Cr/Au evaporation. Graphene is transferred by “bubbling” to the metallized wafer, and by a second round of photolithography and plasma etch the graphene channels are defined. Each array has a total of 52 GFET devices. 75

Figure 4.8: Raman spectra of CVD graphene transferred to Si/SiO_2 wafer. G peak is centered at 1580 cm^{-1} and the 2D band at 2670 cm^{-1}, with an IG/I2D intensity ratio of 0.6 and negligible D intensity, indicative of good quality, monolayer graphene. 76

Figure 4.9: (a) TEM image of the PtNP-Gr structure. Inset: Size distribution of Pt nanoparticles, with an average size of about 1.8-2.4 nm. (b) SEM of a PtNP-Gr nanohybrid FET, 100 000X magnification and 10.0 kV accelerating voltage. 77

Figure 4.10: Diagram of the fabrication process for scFv-functionalized PtNP-GFET arrays. Graphene is transferred to a metalized wafer. Pyrene-NH2 is used to immobilize PtNP near the graphene surface. 78

Figure 4.11: Atomic force microscopy image of a) graphene, b) PtNP-graphene hybrid, and c) scFv/PtNP-graphene, all on Si/SiO2. d) AFM line scans for each step in the fabrication (e) Particle height histograms of PtNP/GFETs, and scFv-functionalized PtNP/GFETs. 79

Figure 4.12: Electrical characteristics of GFET devices at different stages of surface modification, with a representative set of 52 I–Vg curves in each case. (a) As-fabricated GFET, (b) after electrode passivation with MCH, (c) PtNP/GFET hybrid, and (d) scFv-PtNP/GFET nanohybrid device. Insets show histograms of carrier mobility and Dirac voltage along with Gaussian fits (black curves). 80

Figure 4.13: (a) Current–gate voltage (I–Vg) characteristics of a representative GFET device after fabrication and after each successive surface modification leading to formation of anti-HER3 scFv functionalized PtNP/GFET and on exposure to 300 ng/mL HER3 in PBS. (b) The sensing performance of the device against 30 ng/mL HER3; Insets: (upper left) shows sensor response to 300 fg/mL HER3, and (upper right) sensor response to PBS (without antigen). 82

Figure 4.14: Response of the PtNP biosensor showing Dirac voltage shift (ΔV) response as a function of HER3 concentration (300 fg/mL to 300 ng/mL). The data is fitted to a Hill-Langmuir model (red curve); Inset: Comparison of device responses for various control experiments. Fully prepared biosensor to target HER3 at 30 ng/mL (light blue bar). Fully prepared biosensor to negative controls plain PBS buffer (red bar) and non-complementary protein marker osteopontin (OPN; dark blue bar). Also shown is the response in a negative control experiment where a device prepared without the scFv antibody was exposed to the target HER3 at 30 ng/mL (green bar). 83

Figure 5.1: Chemical structure of pyrene-NHS (left) and azide-NHS (right). Both have an [N-hydroxysuccinimide, ester] group, active for amine reactions. ... 93

Figure 5.2: Functionalization strategies for creating Her3-ECD binding sensor. First, the graphene is functionalized with Azide-NHS or Pyrene-NHS. The NHS active groups recognize the primary amine of scFv-A5 receptor protein to form an amide bond. The unmodified NHS groups are blocked with ethanolamine and then the devices are exposed to a Her3-ECD solution. 96

Figure 5.3: Performance characteristics of annealed Graphene-FET array: (A) AFM image 4x4 μm, z=10 nm; (B) Raman Spectra; (C-E) I-V response of 100 G-FET devices, 0.1 V and histograms of Dirac voltage and hole mobility. 97

Figure 5.4: Atomic Force Microscopy (AFM) images and height histograms of scFv-A5 receptor proteins (gold dots) decorating the G-FET surface with: (A-B) Pyrene-NHS and (C-D) Azide-NHS, 3.3 x 3.3μm, z = 5 nm. There is a factor of 4 difference in the protein attachment density between the Azide-NHS and the Pyrene-NHS. The height histograms of AFM features show a peak around 2.5 nm and 5.5 nm for Pyrene-NHS and Azide-NHS, respectively. 99

Figure 5.5: Raman spectra of GFET before (blue) and after (red) exposure to Azide-NHS and after scFv-A5 (green). The strongly enhanced D-band near 1360 cm^{-1} after the functionalization indicates formation of numerous binding sites on the graphene surface. 100

Figure 5.6: I-V_g curves in forward gate sweep after successive functionalization steps of GFET modified with: (A) Pyrene-NHS and (B) Azide-NHS. Note the Dirac voltage shift to positive values after exposure to a solution of scFv-A5, blocking step and Her3-ECD. 101

Figure 5.7: Sensor response (Dirac voltage shift) as a function of HER3-ECD concentration. Each point consists of 25 statistically significant devices for (A) Pyrene-NHS and (B) Azide-NHS. 102

Figure 5.8: (a) Schematic of the GFET fabrication process. (b) Schematic of the electrical probe to characterize graphene devices. (c) Optical Image of a single GFET device. Silicon Oxide (Oxide) regions and graphene are differentiated by a difference in contrast. (d) Optical Image of a 4" wafer after completing fabrication. Process is done at the wafer scale. 109

Figure 5.9: (a) Raman spectrum for a fully patterned GFET channel. The G/2D ratio is 0.33 and D/G ratio is 0.16, in agreement with low defect monolayer graphene. (b) Graphene resistance as a function of gate voltage with subtracted linear baseline for an entire array of GFET. Device yield is 98%. (c-d) Histogram of the Dirac voltage (panel c) and mobility (panel d) for a total of 1100 GFET devices (11 arrays of 100 devices each) from a single fabrication process. 113

Figure 5.10: (a) Schematic for the binding chemistry of the linker molecule and the antibody protein. (b) AFM images of graphene at various steps in the

process. Left: As-transferred graphene. Middle: After azide attachment. Right: After antibody immobilization. 115

Figure 5.11: (a) Schematic of antibody/target binding. (b) R-Vg characteristic shows a shift after exposure to the target. Azide/antibody curve (black) is the reference and it shifts towards the target curve (red). (c-f) Concentration dependent responses (relative to buffer) of antibody/target pairs fitted by Hill-Langmuir model of binding dynamics. (c) GroS-1 antibody, (d) groS-2 antibody, (e) flaB-1 antibody, (f) flaB-2 antibody. 116

Figure 5.12: Relative to buffer Dirac shift for two sets of arrays. Insert shows a schematic of the multiplexed array. Each array is functionalized with groS-1 antibody on the top section of the array and with flab-1 on the bottom section of the array. A mixture of groS target (30 ng/mL in 0.75 mM dialysis buffer) and flaB target (3000 ng/mL in 0.75 mM dialysis buffer) is sensed by the entire chip. An accumulated histogram of the responses (relative to buffer) for both chips is shown, top section in blue and bottom section in green. 118

Figure 6.1: Variation of the Au nanodot area deduced from SEM images (a) and of the nanodot heights deduced from AFM measurements (b). All data have been taken after thermal annealing of Au island films on Si substrates in Ar for 1 h at various temperatures.[11] 126

Figure 6.2: SEM and AFM images of a honeycomb Au mask prior to annealing (a) and SEM and AFM images of annealed Au island films on Si

substrates in Ar for 1 h, and variation of the area distribution of Au nanoparticles depending on annealing temperature: (b) 400, (c) 600, (d) 800, and (e) 1000 °C.[11] 127

Figure 6.3: SEM images of hexagonal arrays of Au nanodots fabricated by annealing at 1000 °C in Ar atmosphere for 1 h. The diameter of the PS spheres was 1000 nm, and the thicknesses of the sputtered Au films varied: (a) 20 nm, (b) 100 nm, (c) 200 nm, and (d) 300 nm. Panel (e) shows the nanodot areas deduced from SEM data as a function of the thickness of the sputtered Au films measured by a quartz crystal microbalance.[11] 128

Figure 6.4: SEM images of Au nanodot arrays that formed after Au film sputtering (200 nm thick) through PS sphere shadow masks onto Si substrates and after annealing at 1000 °C for 1 h in different atmospheres: (a) Ar, (b) air, (c) N2, (d) mixture of Ar and H2, and (e) vacuum.[11] 129

Figure 6.5: (a) AFM line scans of (1) annealed graphene, (2) PBASE functionalized graphene, and (3) graphene functionalized with PBASE and aminated DNA. Inset: AFM images showing the scan lines plotted in the main figure. Scan lines are 2.5 μm. Z-scale 8 μm. (b) I−Vg characteristics for a typical GFET that was annealed, functionalized with PBASE, reacted with 22-mer aminated probe DNA, and exposed to 10 nM target DNA in deionized water.[12] 131

Figure 6.6: (a) Height profile of two linkage chemistry processes for azide-NHS taken by AFM. 2 min exposure (black-dashed) and 30 min exposure to 25

mW/cm^2 365 nm light. (b-c) AFM image of (b) 2 min exposure, and (c) 30 min exposure. 132

Figure 6.7: (a) R-Vg curves for two GFET devices (colored red and blue), dashed lines show devices before functionalization and solid lines show devices after azide-NHS/antibody functionalization. (b) Hill-Langmuir concentration dependent response for 2 min exposure (red) and for 30 min exposure (blue). 133

Figure 6.8: Average transduction by seven charged variants. (A) Lysozyme positions 83 and 119 were mutated to have positive (blue), neutral (yellow), or negative (red) charged side chains. The effective gating ΔVG by each variant varied from 135 to −205 mV, with a value of −34 mV for the neutral N = 0 variant. (B) For all variants, ΔVG is nearly proportional to N, with a slope of −85 ± 2 mV per unit charge. Raw data (open squares) shifted up +34 mV (solid squares) results in a response symmetric around zero. Error bars indicate three standard deviations as determined from n (indicated in parentheses) different devices fabricated with each particular variant.[16] 134

Figure 6.9: (A) Three-dimensional structures of AP273 and AP211. The motifs of AP273 can be folded into 2 kinds of structures, AP273-1 and AP273-2. (B,C) A docking model between AP273-1 and AFP protein. In particular, dC9, dC10, dT11, dA13, dA19, dC20 are in close contact with AFP. C, T and A represent the bases and the number represents the location of the base in the ssDNA sequence. (C) A 3-D interacting mode observed from two views.[15] 135

1 OVERVIEW

In recent years, there has been an increasing need for novel sensor technologies that are low cost, fast, and reliable for environmental and medical applications.[17-20] Nano/Bio hybrids provide the perfect solution for these technological needs. Biological molecules provide high affinity towards their specific target and two dimensional materials are an excellent transduction device for the sensed electrical signal. Recent scientific advances allow for these biomolecules to be tailored to specific sensing needs: synthesized deoxyoligonucleotides can be used for DNA priming,[21] and antibodies and single domain chains can be genetically engineered.[22, 23] Graphene has been used in a wide range of applications.[24-27] It is a single atom thick array of carbon atoms with a carrier density can be tuned with an electric field.[28] Graphene also shows very high mobility even at room temperature (100,000 cm^2/V-s for suspended graphene),[29, 30] and shows high flexibility and tensile strength.[31] In this work, we demonstrate large scale fabrication of clean, high yield Graphene Field Effect Transistor (GFET) arrays that show excellent electrical performance. We aim to build a toolset of scalable processes for fabrication of Nano/Bio hybrid devices with different biomolecules, and different binding mechanisms with the GFET arrays. Having a toolset of binding chemistries allows more biomolecules usable by this technology, and for a wider range of possible biological applications.

Chapter 2 explains the structure and properties of graphene, as well as useful concepts for biomolecules. A description of relevant properties of graphene like mobility, and Dirac voltage are briefly explained through band theory of solids. We relate these fundamental parameters to experimental methods like the dependence of resistance to the applied electric field. There is a summary of the theory of interactions with graphene by both Covalent and Non-Covalent methods. The main properties and relevant binding interactions of deoxyribonucleic acids (DNA), immunoglobulins (antibodies) and their fragment chains (scFv) are discussed.

Chapter 3 explores the functionality and methodology of each of the tools and processes used. First, we describe growth of graphene through chemical vapor deposition (CVD), as well as graphene transfer techniques, and graphene cleaning through chemical treatment or annealing. Then we explore fabrication methods such as mask fabrication, photolithography and thin film deposition, graphene etching, linker chemistries, and biomolecule attachment. Finally, we explain the tools used to characterize the sensor arrays like Atomic Force Microscopy (AFM), Scanning Electron Microscopy (SEM), Raman Spectroscopy, and Electric Characterization.

The following chapters describe the main experimental results. In chapter 4, we discuss nanoparticle aided functionalization of graphene devices. For the first experiment the GFETs are modified with platinum nanoparticles (PtNPs) to obtain a hybrid nanostructure suitable for attachment of HER3-specific, genetically engineered thiol-containing scFv. Physical and electrical characterization of the

arrays is carried out by electron microscopy, atomic force microscopy, Raman spectroscopy, and current–gate voltage measurements. A concentration-dependent response of the biosensor to HER3 antigen is found, with a dissociation constant of 800 pg/mL and a is 300 fg/mL limit of detection. For the second experiment the GFETs are modified with gold physical vapor deposition followed by thermal annealing to form monodisperse gold nanoparticles (AuNPs). Devices are in a four-probe configuration, with high carrier mobility (3590 ± 710 cm2 /V·s) and low unintended doping (Dirac voltages of 9.4 ± 2.7 V). The AuNP-Gr-FETs were readily functionalized with thiolated probe DNA to yield DNA biosensors with a detection limit of 1 nM and high specificity against noncomplementary DNA.

Chapter 5 discusses chemical linking of biomolecules to graphene devices to form Nano/Bio sensors. Initially we compare two different chemicals linking methods, with 1-pyrenebutanoic acid succinimidyl ester (pyrene-NHS) and 4-Azide-2,3,5,6-tetrafluorobenzoic acid, succinimidyl ester (azide-NHS) for covalent and non-covalent binding, respectively. We use a 100 device, two probe, array that show 2363 $\pm$ 87 cm^2/Vs mobility and -3.4 $\pm$ 0.3 V Dirac voltage. The recognition of the binding between Her3-ECD and scFv-A5 is shown as a concentration-dependent response in the Dirac voltage, with a detection limit of 3.1 pg/mL, a factor of 100x more sensitive than ELISA. Finally, we show the multiplexing potential of sensing arrays. We use a 100 device, two probe, array built on an HMDS treated SiO_2 wafer. Devices show high mobilities (4952 ± 1682 cm^2/V-s) and low charge doping (Dirac

voltage of 0.5019 ± 2.712 V), and high transistor yield (98%). Sensors are then functionalized with an engineered Lyme antibody protein by a photoactivated perfluorophenyl azide linker chemistry. Four different antibodies specific to two different targets (two antibodies for each target) were measured and show a concentration dependent response. A mixture of the targets is then measured where the antibodies are multiplexed at different regions of the sensor array, showing a distinct detection between the two components of the mixture.

A summary of the experimental results presented in this thesis and prospects for the future that this technology could allow are presented in chapter 6.

2 INTRODUCTION TO GRAPHENE AND BIOMOLECULES

Several applications require sensor technology that has high sensitivity and selectivity, while at the same time being fast and affordable. Applications such as environmental monitoring, and biomedical diagnostics are of special interest in later years.[32-35] Nano/Bio sensors combine the sensitive, highly selective synthetic biomolecules with the speed and cost of Nano materials. Graphene specifically is a particularly good candidate for sensing applications due its well understood carbon chemistry, high electrical properties, and surface to volume ratio.

It is important to understand both components of our Nano/Bio hybrid sensors. This chapter describes Graphene in the context of band theory of solids, the three terminal Graphene Field Effect Transistor, as well as the electrical characteristics of graphene. The chapter then discusses the structure of biomolecules, the functions of deoxyribonucleic acid (DNA) and Immunoglobulins (IgG) which are the two types of biomolecules we used on this thesis, and the binding chemistry in biomolecules.

2.1 GRAPHENE

Graphene is a carbon allotrope, where sp^2 hybridized carbon atoms are planarly arranged in a tightly bound hexagonal lattice.[36, 37] The unit cell for graphene (Figure 2.1a) is defined by a two atom basis with primitive translation vectors given in equation (2.1). Here $a_0 = 0.14\ (nm)$ is the interatomic distance between

carbon atoms. These primitive vectors form the Bravais lattice of graphene. These planar sheets can stack on top of each other with an interatomic distance of 0.33 (nm) to form graphite.

$$\begin{aligned} \vec{a}_1 &= \frac{a_0}{2}\left(\sqrt{3}\hat{\mathrm{x}} + \hat{\mathrm{y}}\right) \\ \vec{a}_2 &= \frac{a_0}{2}\left(-\sqrt{3}\hat{\mathrm{x}} + \hat{\mathrm{y}}\right) \end{aligned} \tag{2.1}$$

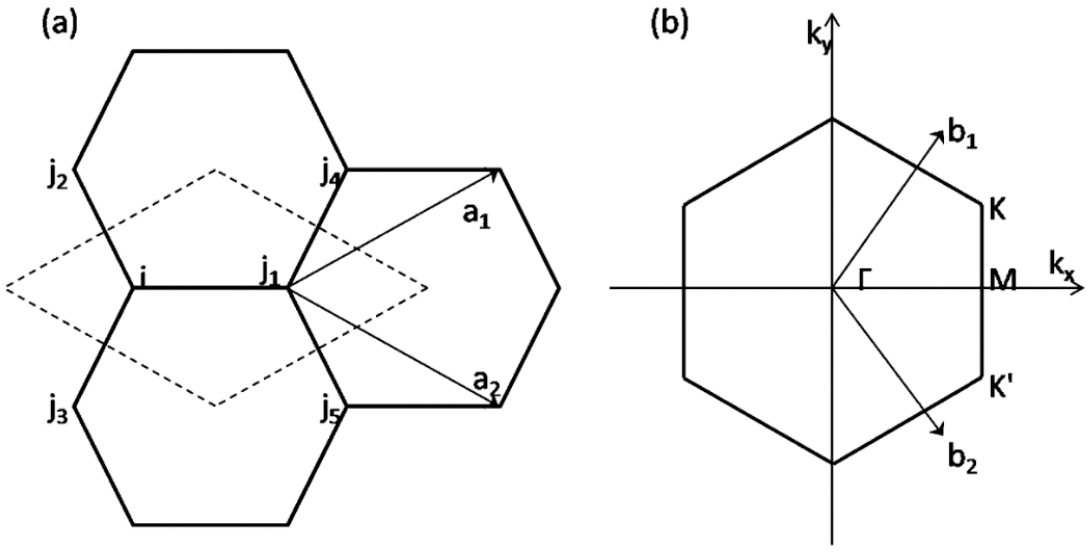

Figure 2.1: (a) Bravais lattice of graphene with unit cell (dashed line) and primitive vectors $\vec{a}_1$ and $\vec{a}_2$. Carbon atoms i and j_1 are the atom basis. Atoms j_n are first and second nearest neighbors of atom i. (b) Brillouin zone for the reciprocal lattice with primitive vectors $\vec{b}_1$ and $\vec{b}_2$. K and K′ are the irreducible wave vector points in the Brillouin zone, Γ and M represent significant wave vectors in the reciprocal space.[13]

It is useful to define the Brillouin zone, which is the primitive cell defined in reciprocal space (Fourier transform of the Bravais lattice). Two primitive vectors can be defined as in equation (2.2) for the Brillouin zone (Figure 2.1b). We can then

identify wave vectors that are of interest, Γ for the origin of the reciprocal space, K and K′ are the two irreducible points (each corresponding to the sub-lattices of the Bravais lattice) at the edge of the Brillouin zone, and M for the midpoint between the two irreducible points.

$$\begin{aligned} \vec{b}_1 &= \frac{2\pi}{a_0}\left(\frac{\sqrt{3}}{3}\hat{k}_x + \hat{k}_y\right) \\ \vec{b}_2 &= \frac{a_0}{2}\left(\frac{\sqrt{3}}{3}\hat{k}_x - \hat{k}_y\right) \end{aligned} \tag{2.2}$$

2.1.1 Band Structure of Graphene

The band structure of graphene was calculated theoretically using tight binding (or linear combination of atomic orbitals) model.[38, 39] Tight binding is a semi-empirical calculation method used to estimate band structure in theory of solids. For systems with low number of atoms in the unit cell, wave functions can be used to obtain an exact result. The general assumption is that electrons are tightly bound to the atom to which they belong and they have limited interaction to the surrounding potentials. We can then assign probability of interaction γ^n to the interaction with the n^{th} nearest neighbor, and solve a system of order n. Solving for graphene to the first order the dispersion is as shown in equation (2.3).

$$\varepsilon_{(\vec{k})} = \pm\gamma\sqrt{1 + 4\cos\left(\frac{\sqrt{3}k_x a_0}{2}\right)\cos\left(\frac{k_y a_0}{2}\right) + 4\cos^2\left(\frac{k_y a_0}{2}\right)} \qquad (2.3)$$

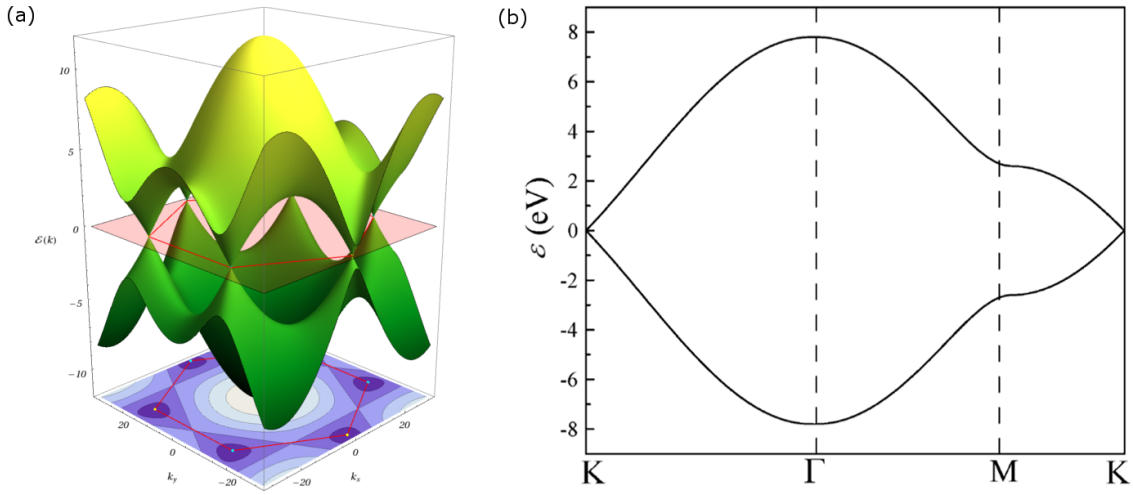

Figure 2.2: (a) Calculated dispersion for graphene in the Brillouin zone. This is the solution to a first order tight-binding model. In red, the Fermi Energy level. The valence and conduction band are below and above the Fermi level, respectively. (b) Projection of the dispersion along the wave vector path K → Γ → M → K.[1-3]

Graphene dispersion shows graphene is a zero-bandgap semiconductor with density of states equal to zero at the fermi energy.[38, 39] The conduction at valence bands have a null gap at the K and K′ points, called neutrality points. The value of the overlap integral (probability of interaction) can be calculated by density functional theory, and it equal to $\gamma = 2.5\ (eV)$.[40] This value is experimentally confirmed by scanning probe microscopy.[41] Figure 2.2a shows the complete dispersion inside the Brillouin zone, Figure 2.2b shows the projections along a specific wave vector path.

2.1.2 Graphene Field Effect Transistors

There is great interest in the integration of graphene devices with DC and RF applications[42, 43]. For all research in this thesis we used the three terminal Field Effect Transistor (FET). Graphene, due to its tunable carrier density, can be used in the main conducting channel of a FET. For Graphene Field Effect Transistors (GFET) an Electric Field can tune the carrier density, this is done by applying a voltage (Vg) to capacitively coupled terminal called *gate*. The current along the cannel can then be measured to have a dependence with the gate voltage due to the coupling with the carrier density in the cannel. The current is measured by applying a bias (V_b) to two terminals at each end of the graphene channel.

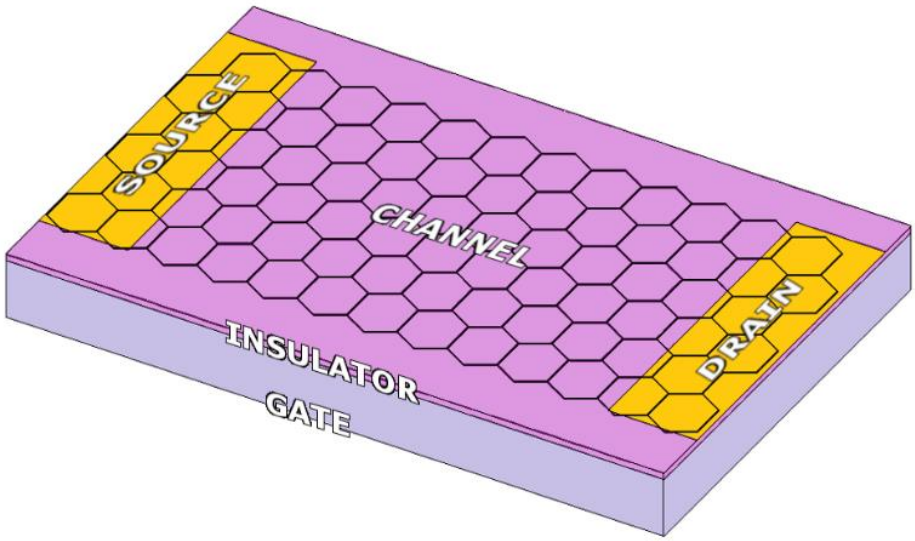

Figure 2.3: Schematic of a Graphene Field Effect Transistor (GFET). Indicated are the three terminals source, drain and gate. The channel is separated from the gate by an insulating layer. A bias voltage is applied to measure the current through the channel, this current changes with carrier density which is a function of the gate voltage.

2.1.3 Carrier Density

In the case of two dimensional materials such as Graphene, carrier density is defined as the number of electrons or holes per unit of area. Graphene is a material with tunable carrier density, then the doped carrier density (n^*) is the measure of carriers injected into the graphene channel due to an applied electric field and he residual carrier density (n_0) as the measure of the carriers that produce the minimum conductance. The residual carrier density for ideal graphene should be zero but it is not due to several factors such as interactions with the substrate, temperature, defects, among others. The total carrier density (n) can then be modeled as:[44, 45]

$$n = \sqrt{(n_0)^2 + (n^*)^2} \tag{2.4}$$

We then consider the source of carriers injected into the graphene. When a voltage is applied to the capacitively coupled gate of a GFET the generated electric field injects charge ($q^* = en^*$) to the graphene. Considering the coupling as that of a parallel plate capacitor, the injected charge density is $n^* = \frac{1}{e} CV^*$. Where V^* is the voltage difference with respect to the neutral voltage, and C is the total coupling capacitance. Equation (2.4) can be written as:

$$n = \frac{1}{e}\sqrt{(en_0)^2 + (CV^*)^2} \tag{2.5}$$

2.1.4 Dirac Voltage

Figure 2.2a shows the dispersion for graphene, that is the energy dependence with the momentum of electrons. The Fermi level is the energy such that all states above it are empty, for graphene at $0\,K$ temperature, its where the valence and conduction bands cross. Electrons being injected or depleted are going to fill up empty states close to the fermi level. The dispersion relation then depends only on wave vectors that around K or K'. here the dispersion can be shown to be linear, and it is commonly referred as a Dirac Cone,[38] show in Figure 2.4 for depleted electrons, at the neutrality point, and for injected electrons.

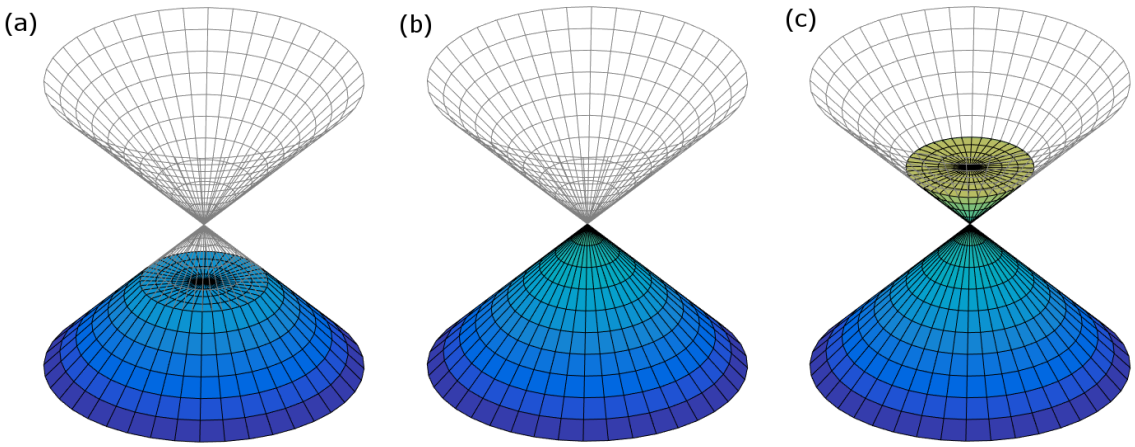

Figure 2.4: Dispersion around the Dirac Cone for graphene. (a) Depleted electrons, are taken from the valence band (b) Neutrality point, electrns occupy states up to the fermi level. (c) Injected electrons, are placed on the conduction band.

In a GFET we inject or deplete electrons by means of the capacitively coupled gate voltage (V_g). At $V^* = 0$ the energy is the fermi level (Figure 2.4b). Additionally, if the temperature is $0\,K$ the gate voltage should be equal to the

coupled voltage, that is $V_g = V^*$. There are two main factors that would alter the actual value of V^*, the interaction with the substrate, and temperature. Those effects amount to an additional constant Energy (if those parameters remain constant), or additional carriers at the neutrality point. Equation (2.6) can then be written as:

$$n = \frac{1}{e}\sqrt{(en_0)^2 + C^2\left(V_g - V_D\right)^2} \tag{2.6}$$

where V_D, is called the Dirac Voltage. And it is the constant energy added due to the interactions effects at room temperature. This is the voltage we will use to characterize our sensors. When the gate voltage is lower than the Dirac voltage we deplete electrons from the channel, and conduction is possible with electron vacancies (holes) in the valence band. When the gate voltage is higher than the Dirac voltage we inject electrons to the channel, and conduction is possible with electrons in the conduction band. Due to this dual conduction (with holes in the valence band and with electrons in the conduction band) graphene is said to be ambipolar.[37]

2.1.5 Carrier Mobility

Carrier mobility characterizes the movement of electrons when in the presence of a driving electric field. It is important to note that the driving electric field is different from the coupling electric field. Carrier mobility is defined as:

$$\vec{v} = \mu\vec{E} \tag{2.7}$$

where $\vec{v}$ is the velocity of electrons, μ is the mobility, and $\vec{E}$ is the electric field that drives the electron motion. Mobility is commonly measured using the hall-effect, where mobility is can be calculated by equation (2.8).[46] τ is the scattering time and $m^*$is the apparent mass (equation (2.9)). The mobility then depends on scattering effects, where factors affecting this scattering will in turn affect the mobility. Factors such as defects, substrate interactions, and temperature will decrease mobility. From the dispersion, we can calculate the apparent mass around the fermi energy to be zero. However, mass is not zero but a small value. This is the cause for the giant mobilities in graphene.[47] Factors that cause the neutral charge to be non-zero will cause the mobility to decrease.

$$\mu = \frac{e\tau}{m^*} \tag{2.8}$$

$$m^* = \frac{\hbar^2}{\frac{\partial^2 E}{\partial k^2}} \tag{2.9}$$

Typical mobilities of graphene range from 2,000 cm^2/V-s and 100,000 cm^2/V-s, depending on the different factors present during measurement.[48-52] Fore reference, typical mobility on electronic silicon based devices is ~1,000 cm^2/V-s.[53]

Current density ($\vec{J}$) can be calculated as the total charge density multiplied by the velocity of electrons. Equation (2.7) can then be written as:

$$\vec{J} = ne\mu\vec{E} = \sigma\vec{E} \tag{2.10}$$

σ is the conductivity of Graphene. Using equation (2.6) (defining W as the width and L as the length of the graphene channel) and $\sigma = ne\mu$ from equation (2.10) channel resistance can be calculated as:

$$R_{Ch} = \frac{1}{\mu\frac{W}{L}\sqrt{(en_0)^2 + C^2\left(V_g - V_D\right)^2}} \tag{2.11}$$

2.1.6 Contact Resistance

Equation (2.11) is the graphene channel resistance as a function of the gate voltage applied. It is important now that we consider the case of the interface between graphene and a metal contact, since it has been shown to depend on the gate voltage.[54] Ignoring the effects at the interface of graphene and metal can lead to errors when determining the mobility.[55, 56] There are two effects that dominate the graphene/metal interaction. The first one is work function pinning, the second one is contact doping.[6] Pinning is referred to a change in the work function of graphene to match due to the difference with that of the metal when they come into contact, since the work function of metals is not easily tuned the graphene is has its

work function pinned.[57] We can see this effect as in Figure 2.5a where the Dirac cone of graphene in contact with the Dirac cone of pristine graphene is increased in Energy. Doping occurs when graphene is only partly in contact with a metal, causing the increase in work function in the regions where there is contact and unchanged otherwise. There is a gradual change of the work function close to the edge between the exposed graphene and the graphene in contact with the metal, this region is the charge transfer region, (Figure 2.5b).[6]

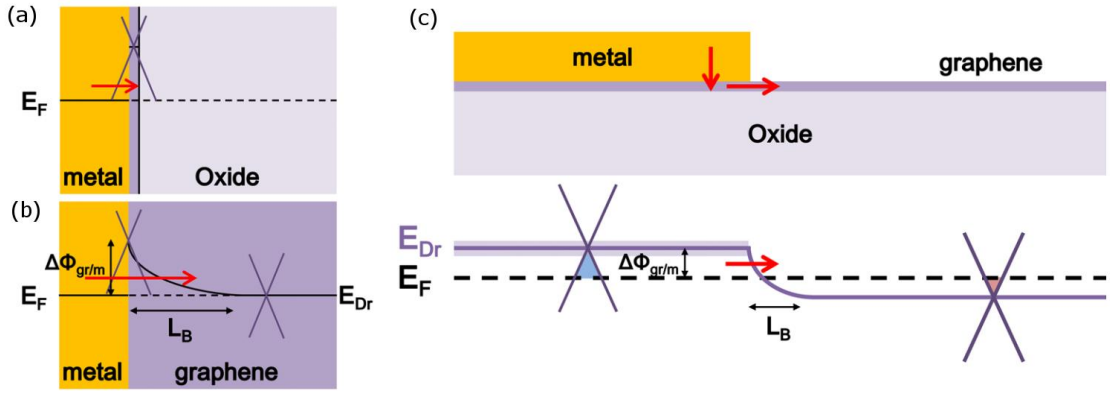

Figure 2.5: (a) Pinning effect of a graphene-metal contact, the Dirac cone has shifted from the fermi energy (E_F) to now match the work function difference. (b) Doping effect near the edge between the exposed and the unexposed graphene. Pinned and unpinned Dirac cones are shown as well as the depletion region (L_B). (c) p-n junction of the around the graphene edge. Once the Fermi level increases enough (by increasing the gate voltage) both Dirac cones can be n conducting forming an n-n region. Similarly, for decreasing Fermi level forming the p-p junction.[6]

Consider purely exposed graphene as an n-n junction for the electron branch and a p-p junction for the hole branch (Figure 2.5c). We can smoothly switch between these two regions by tuning the gate voltage and the transition point is the Dirac voltage. However, when graphene partly interfaces with a metal contact there

is a p-n junction with a depletion region between the n-n and the p-p.[58] This introduces an asymmetry with respect to the Dirac voltage, where the hole current is usually higher than the electron current.[6] Figure 2.6 shows the measured contact resistance for several metals as a function of gate voltage. In this thesis, we will model this effect by a linear response centered at the Dirac voltage. We can then write the total as the sum between the channel and the contact resistance.

$$R = \overbrace{R_0 + R_s\left(V_g - V_D\right)}^{Contact\ Resistance} + \overbrace{\frac{1}{\mu \frac{W}{L}\sqrt{(en_0)^2 + C^2\left(V_g - V_D\right)^2}}}^{Channel\ Resistance} \tag{2.12}$$

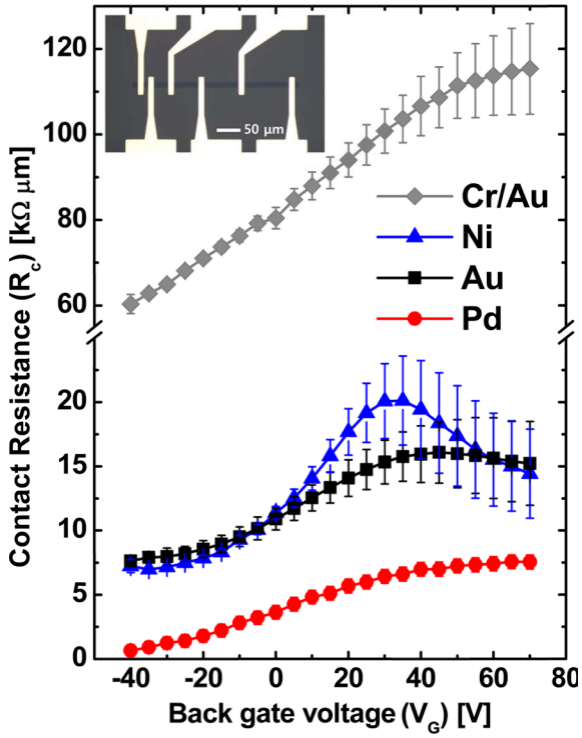

Figure 2.6: Contact resistance as a function of gate voltage for several metals. Insert shows the layout of the experiment.[6]

2.2 BIOMOLECULES

In general, biomolecules are any molecule that is present in living organisms. Structurally, they are polymeric chains made from fundamental structures called biomonomers. The four different types of biomonomers are amino acids, monosaccharides, isoprene, and nucleotides.[59] In this thesis, we will focus on Amino Acid and Nucleotides derived Structures.

Amino acids contain amine and carboxylic acid functional groups attached to a common carbon. There are twenty-one standard amino acids, five of have charged side chains, four are polar but uncharged on their sidechains, eight have a hydrophobic side chain, and the remaining four are special cases (one of which is strictly speaking not an amino acid). Some enzymes can modify the structure of these amino acids and the result would not be one of the standard twenty-one. One type of complex polymeric chains of amino acids is called protein. Proteins can do a vast array of functions in living organisms, due to the varying array of functions provided by amino acids. Their specific function is the result of the complex interactions between its components. This usually not only involves the order of the chain but also the specific folding it takes in equilibrium. When a protein loses functionality due to some external factor (*i.e.* pH, temperature) it is said to have denatured.

Nucleotides are phosphorylated nucleosides, that is a nucleoside that has gained a phosphate ($(PO_4)^{3-}$) group. Nucleosides are glycosylamines composed of a nucleobase and a 5-carbon sugar (either a ribose or a deoxyribose). There are five nucleobases, Adenine (A), Guanine (G), Thymine (T), Uracil (U), Cytosine (C). Depending on which 5-carbon sugar composes the nucleotide, the complex polymeric chains formed are called ribonucleic acid (RNA) or deoxyribonucleic acid (DNA).

2.2.1 Immunoglobulins

For sensing applications, a very prevalent biomolecule are antibodies. Sensing applications for antibodies have been demonstrated using immunoassay design, quantum dots, fiber optics, fluorescence, and others.[60-63] Antibodies are also called Immunoglobulins (Ig), they are large Y-shaped proteins (Figure 2.7) that is used by the immune system to identify and neutralize harmful agents in living organisms. There are different types of antibodies, most notably Immunoglobulin G (IgG) constitutes most the immune system. Structurally they are made of structural units called the heavy chain, light chain, and the variable fragment (scFv). There are different types of heavy chains but their function is to direct the appropriate immune response. Variable fragments are what allows antibodies the flexibility to identify a variety of diseases, this chain reacts specifically to a target molecule (antigen).[64, 65]

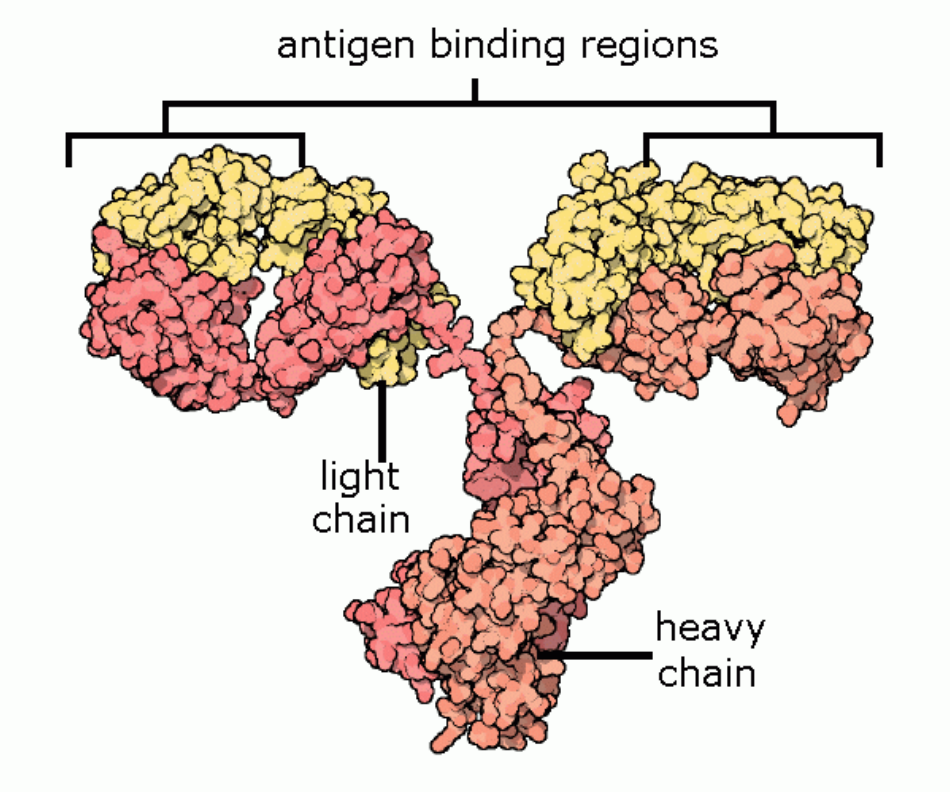

Figure 2.7: Computer generated immunoglobulin. Annotated the two different chains of the antibody and the binding regions.[4]

Antibodies are produced naturally by B-cells of the adaptive immune system.[64] It is possible to synthesize antibodies, both the entire IgG as well as the scFv by itself. An scFv has the same or better binding affinity than the complete IgG, with the benefit of being smaller size (25kDa for scFv compared to 150 kDa for IgG).[66] This is done by injecting an animal (typically mice, or rabbits) with the target protein and harvesting their B-line cells. Through purification and cellular cloning several copies of the cell can be tested. The genetic material can then be extracted to either synthesize the full IgG or the scFv.[67]

2.2.2 Deoxyribonucleic Acid

Deoxyribonucleic Acid (DNA) is the biomolecule that carries all genetic instructions of living organisms. Most DNA molecules consist of two polynucleotide chains, each chain is formed by a combination of the A, C, T, or G nucleotide bases bound together in a helix shaped structure (Figure 2.8). The 5-carbon sugar of the nucleotide in one chain is covalently bonded to the phosphate group in the other, causing only two nucleotide pairs to form T-A, and C-G. This means the same amount of biological information is stored in a single helix than in a double helix.

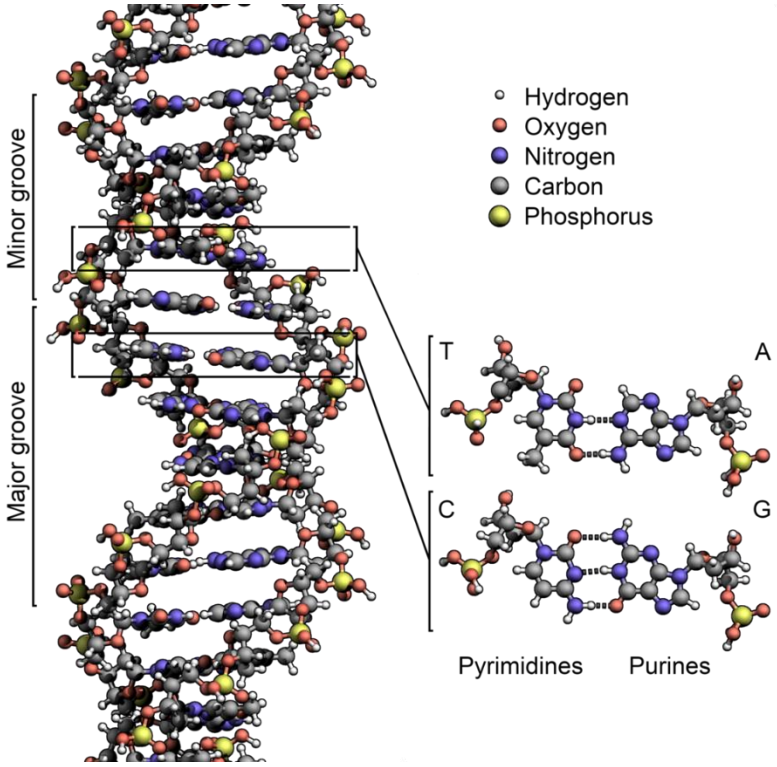

Figure 2.8: Computer generated image of a Deoxyribonucleic Acid (DNA) structure. T-A and C-G base pairs are highlighted.[5]

The main application of DNA in this thesis is to use one strand to detect its complement. Due to the nucleotide affinity, the entire chain is highly sensitive to its target even changing a few base pairs in the chain makes the binding probability decrease significantly.[12]

2.2.3 Hill-Langmuir Model

Antibody/Antigen or DNA complementary chain binding are complex interactions where one molecule gets adsorbed into another. The model used in this thesis is a Hill-Langmuir Model. The Langmuir adsorption model assumes the adsorbate behaves like an ideal gas at thermal equilibrium, which can be calculated using the partition function.[68, 69] For N adsorbates interacting with N_s binding sites, we can write the partition function ($Z_{(N)}$) as

$$Z_{(N)} = \zeta^N \frac{N_s!}{N!\,(N_s - N)!} \tag{2.13}$$

where ζ is the partition function for a single adsorbate to a single binding site. Here, the partition function is the number of ways N_s adsorbates (related to the sites) given a total number N. The gran canonical partition function ($\mathcal{Z}$) can then be calculated to be

$$\mathcal{Z} = \left(1 + \zeta e^{\frac{\mu}{k_B T}}\right)^{N_S} \tag{2.14}$$

here μ is the chemical potential, k_B the Boltzmann constant, and T the temperature. Calculating the Landau energy from equation (2.14 and using $\left(\frac{\partial L}{\partial \mu}\right)_{T,V} = -N$ we can calculate the ratio of adsorbates to binding sites.

$$\frac{N}{N_s} = \frac{\zeta e^{\frac{\mu}{k_B T}}}{1 + \zeta e^{\frac{\mu}{k_B T}}} \tag{2.15}$$

Since the model defines the adsorbates as an ideal gas in thermal equilibrium the chemical potential of the adsorbates μ equals the chemical potential of an ideal gas. Using the ideal gas law, equation (2.15 can be written as:

$$\frac{N}{N_s} = \frac{\frac{P}{P_0}}{1 + \frac{P}{P_0}} \tag{2.16}$$

$$P_0 \equiv \frac{k_B T}{\zeta}\left(\frac{m k_B T}{2\pi\hbar}\right)^{3/2} \tag{2.17}$$

P is the pressure of adsorption. When $P = P_0$, there are twice as many adsorption sites as available adsorbates. P_0 then is the pressure of adsorption where half the binding sites are occupied. The Hill coefficient n, that represents the effect of enhanced binding near similar ligands.[70] Using the Hill coefficient and write the ratio of pressures as the ratio of concentrations, equation (2.16 can is:

$$\frac{N}{N_s} = \frac{\left(\frac{[c]}{[K]}\right)^n}{1 + \left(\frac{[c]}{[K]}\right)^n} \tag{2.18}$$

$[c]$ is the concentration of the adsorbates (target), $[K]$ is the concentration for half occupation of binding sites, and n is the Hill coefficient.

2.2.4 NHS ester/Amine Chemistry

NHS esters are an amine specific functional group. The reaction involves the carboxylate ester reacting with the amine in biomolecules to form an amide bond (Figure 2.9). Hydrolysis of the NHS ester is a competing reaction and its rate is proportional to the pH. The half-life of NHS esters is estimated to be 4 to 5 hours at pH 7.0 and 0°C, but it decreases to only a few minutes above pH 8.0. It would decrease further at higher temperature.

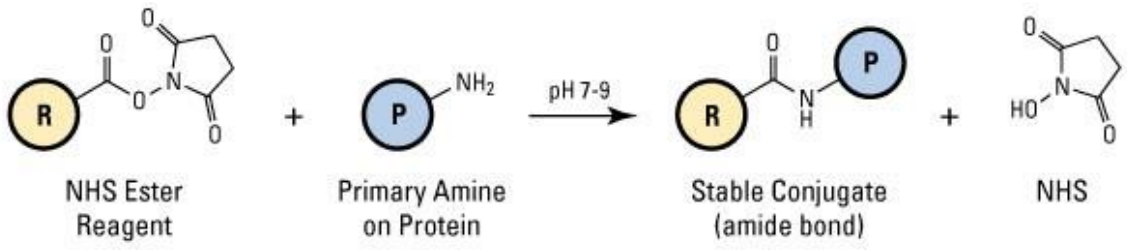

Figure 2.9: NHS ester/Amine reaction. Reaction is optimal close to neutral pH. Amide bond is formed and a hydroxysuccinimide are released.[7]

2.3 SUMMARY

In this chapter, we introduced the concepts for both parts that compose a Nano/bio hybrid sensor. We described the morphology of graphene and calculated the energy dispersion of graphene. We derived the resistance of a GFET device from first principles, defining the mobility, Dirac voltage and neutral charge density. We considered the effect of the interaction between a metal contact and graphene when fabricating our devices. Then we described the biomolecule structure and properties, specifically antibodies and DNA both used in this thesis. We used statistical mechanics to describe the binding dynamics between two complex molecules, as described by the Hill-Langmuir model. Finally, we described the chemistry of NHS-esters and amines in biomolecules used in linker molecules. All these concepts are crucial when exploring the work presented in this thesis.

3 EXPERIMENTAL METHODS

This chapter describes the details of the experimental methods used during fabrication and characterization of the Nano/bio hybrid devices presented on this thesis. We start with processing techniques for graphene, covering synthesis of graphene and electrolysis driven ("bubble") transfer. Second, we discuss the fabrication of GFETs. We outline the procedure used for fabrication, and then we detail each step of the process, laser, and photo- lithography, deposition of thin layers, plasma etching, and annealing. Then we discuss the functionalization chemistries, using a pyrene based linker, an PFPA based linker, and nanoparticle aided functionalization. Finally, we describe the characterization techniques such as electrical measurements, Atomic Force Microscopy, and Raman spectroscopy.

3.1 CHARACTERIZATION METHODS

3.1.1 Electrical Measurement

Electrical transport in graphene is a measure of local electrostatic effects in its surroundings.[71] Considering the presence of the biomolecule and target causes an electrostatic change close to the graphene we can precisely determine binding effects by properly characterizing transport. In this thesis, we use two electrical configurations to characterize arrays shown in Figure 3.1, two-probe and four-probe configurations. In both configurations, we characterize the resistance of the channel at a range of gate voltages (V_g). Two-probe configuration measures the current (I)

through the device at constant bias voltage (V_b). Four-probe configuration measures the voltage (V) across the middle ports when a constant bias current (I_b) flows through the outer ports. The Four-probe measurement geometry removes any ohmic effect of contact resistance.

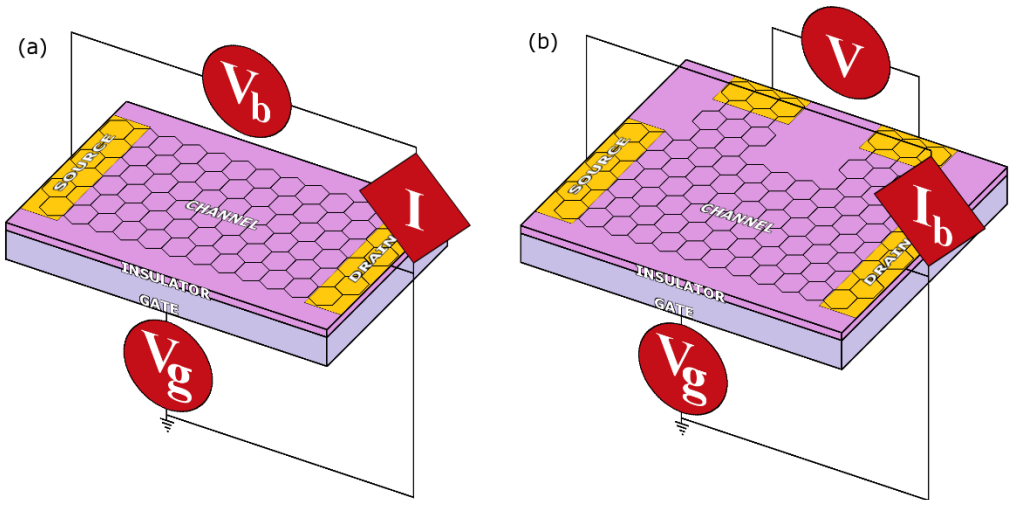

Figure 3.1: Connection schematic for electrical characterization of GFETs for (a) two-probe configuration, V_g is gate voltage, V_b is the bias voltage, and I is the measured current (b) four-probe configuration, V_g is gate voltage, I_b is the bias current, and V is the measured voltage.

All electrical measurements throughout this thesis were performed in a CASCADE MICROTECH MPS150 TRIAX modified for parallel measurement (up to 136 pins). Under normal operation the setup requires two source meters, so we used a KEITHLEY 6517A as a gate voltage source and a KEITHELY 2400 as either a voltage source/picoammeter or a 4-probe meter depending on configuration. However due to the need for simultaneous measurement of each device in a large array during electrical characterization we used in addition a NATIONAL INSTRUMENTS PXIe-1073 MXIe and a PXI-2535 4x136 FET switching matrix (SM) that allows connections between an input line and any of its output ports. A

custom order ACCUPROBE probe card is used to connect the column outputs to the GFET pads on the chips. The setup allows to connect the source meters (rows SM) to the source or drain of GFETs (columns SM/probe card). Finally, data is collected digitally through a NATIONAL INSTRUMENTS DAQ card and instruments are controlled through either GPIB or USB ports. LabVIEW is used to control the setup. The setup is shown in Figure 3.2.

Figure 3.2: Parallel electrical characterization setup. Two Keithley source meters, a probe card, a switching matrix, the probe station, and a controller computer are shown.

3.1.2 Atomic Force Microscope

Although a monolayer graphene film is visible to the naked eye, many important properties of nanoscale materials exist on a scale below the resolution limit of visible light microscopy. Scanning Probe Microscopy can be used to improve on the visible limit: a probe raster-scans across the sample measuring a specific property and an image is generated by mapping this quantity in the probed area. Atomic Force Microscope (AFM) uses a small mass, sharp tip that is able to deflect vertically due to electric or magnetic forces (depending on the material of

the tip).[72] AFM is a relatively non-invasive SPM technique, especially if the tip is set to “tapping mode” where the tip is piezoelectrically driven to oscillate near resonance. The measurement of the oscillation is done by a laser that reflects off the backside of the cantilever and is collected on a four-quadrant photodetector. Intramolecular forces cause a dampening in the oscillation changing its amplitude, frequency, and phase.[73] A feedback loop maintains a constant dampening force by changing the distance to the sample. The height of the surface can be calculated from the feedback. Figure 3.3 shows an illustration of an AFM operating principles.

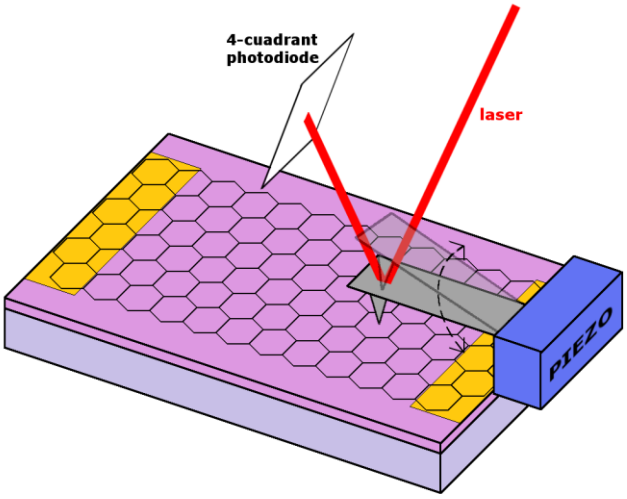

Figure 3.3: Diagram of AFM operation. Piezoelectric sensor controls the oscillation, movement in the horizontal plane and the height. A feedback loop keeps the measured force constant.

Amplitude and phase of the AFM scan can also provide useful topographical information.[74] The phase of the oscillation of the cantilever varies with the physical properties of the material. Lateral resolution is limited by tip radius and the mechanical components that move the sample, Z direction however is much more sensitive since it is limited by the photodetector resolution and vibrational noise.

A BRUKER DIMENSION 3000 was used for all AFM images in this thesis. Cantilever tips were TAP300Al-G Budgetsensors with a resonant frequency of 300 kHz and a tip radius less than 10 nm. Scanning was done parallel to the electrode orientation and in tapping mode.

3.1.3 Scanning Electron Microscope

The Scanning Electron Microscope (SEM) measures signals from the interaction between a beam of electrons focused on a small spot on the sample and the atoms on that spot.[75] The signals contain different information on the topography and composition of the material, depending on how they were collected. The position of the beam and the information collected from the interaction signals can be processed to generate an image. The types of signals include secondary electrons (SE), back-scattered electrons (BSE), photons from x-rays, and cathode luminescence (CL); the most common being SE. Samples must be electrically conductive at the surface, and grounded during measurement (to avoid electron accumulation. The experiment is done in low vacuum or high vacuum, over a wide range of temperatures. The electron beam itself can be generated either thermoionically (SEM) or by a field emitter (FE-SEM). Figure 3.4 shows the electron beam focused by using a series of scattering apertures and electromagnetic lenses. For this thesis, all images were taken using a FE-SEM JEOL 7500F.

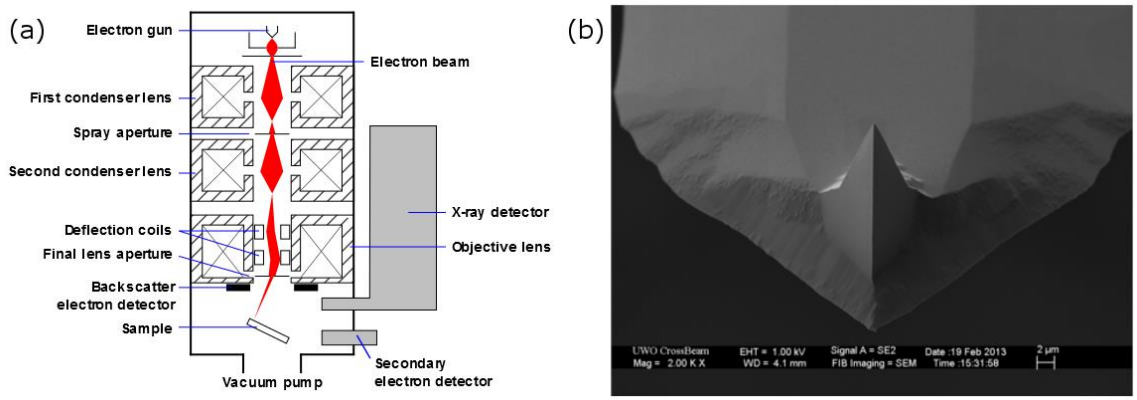

Figure 3.4: (a) Schematic of a Scanning Electron Microscope. Electron gun generates the stream of electrons; a series of electromagnetic condensers and apertures focus the beam to a small point on the sample. The whole system is under vacuum. (b) SEM image of an AFM tip.[2-3]

3.1.4 X-Ray Photoelectron Spectroscopy

X-Ray Photoelectron Spectroscopy (XPS), or Electron Spectroscopy for Chemical Analysis (ESCA), is a spectroscopic technique that measures electron binding energies of the atoms in a material.[76] A sample is bombarded with an X-ray beam with energy such that electrons are ejected from the sample's atom orbitals, simultaneously the number of electrons is counted and the kinetic energy for each is measured (Figure 3.5). Experimentally XPS requires high or ultra-high vacuum and only the first few atomic layers from the surface (~10nm) can be measured. Additionally, XPS has trouble detecting atoms with low atomic number, like hydrogen or helium. Detection limit is around the parts per million (ppm) but lower limit can be achieved by doing long exposures.

The energy collected is discreet due to the quantum nature of atomic orbitals. Then, by energy conservation we can write,[77]

$$E_{h\nu} = E_k + \phi + E_{B(i)} \tag{3.1}$$

where $E_{h\nu}$ is the x-ray energy, E_k is the photoelectron kinetic energy, ϕ is the work function (this compensates for the work function of the sample and the absorption of the electron by the detector), and $E_{B(i)}$ is the binding energy for the *i-th* level. $E_{B(i)}$ is calculated for each event in the photodetector and an energy histogram is constructed, peaks in the histogram can be fitted to a Lorentz peak to find the binding energies of the spectrum.

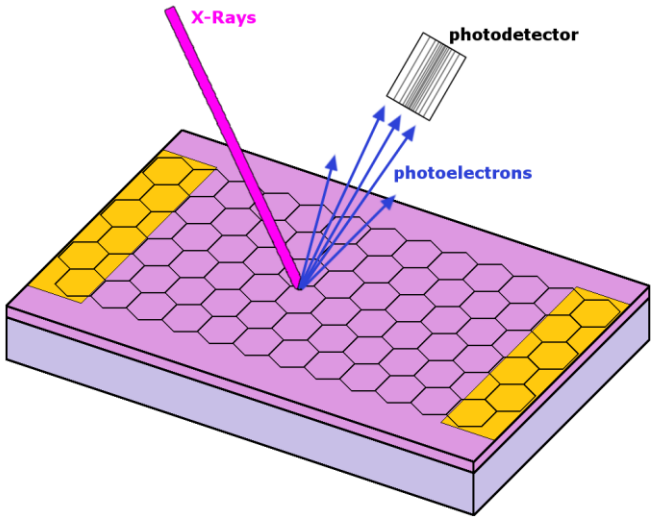

Figure 3.5: Diagram of XPS operation. An X-ray beam shines to the sample and excites photoelectrons that are detected. The measured energy spectra of the photoelectrons depends on the sample composition.

A VG Scienta AB XPS is in this thesis. Analysis was performed using a monochromatic Al Kα source ($E_{h\nu} = 1486.6\, eV$) The residual pressure in the chamber was maintained to less than 10^{-8} Torr and the spectrometer was calibrated to ISO 15472:2001 with an accuracy of ± 0.05 eV. Survey and high-resolution

spectra were acquired in constant-analyzer-energy mode with pass energies of 200 or 100 eV. The spectra were processed using CasaXPS software (v.2.3.16, Casa Software Ltd.). Background subtraction was performed using the Shirley−Sherwood method. The quantitative evaluation of XPS data was based on integrated intensity using a first-principles model and applying Powell's equation.[78]

3.1.5 Raman Spectroscopy

Raman Spectroscopy is a technique used to observe vibrational modes (linear or rotational) of a material.[79] The sample is irradiated with a laser that interacts with the low energy phonons (vibrations), the sample then either absorbs or releases a small amount of energy as photons. The energy released is a function of the energy of the phonons (vibrational modes) involved in the interaction. The photons are counted and their energy is measured. The Raman shift is then calculated as in equation (2.1, and from it histogram is constructed.

$$\Delta\varpi = \left(\frac{1}{\lambda_0} - \frac{1}{\lambda_R}\right) \tag{3.2}$$

where λ_0 is the laser wavelength, λ_R is the excited photons wavelength, and $\Delta\varpi$ is the Raman Shift (usually in cm^{-1} units).

Raman Spectroscopy for carbon systems has been extensively studied.[80, 81] The two most prominent peaks in the Raman spectra for Graphene are the G and G'

peaks, however defects in graphene also cause scattering signals at peaks D and D'. The G band depends on the sp^2 hybridized carbon-carbon bond, meaning that any deformations would show by shifting the G peak; as in carbon nanotubes, for example. The G' band shows a widening and shift for increasing number of layers.[82] The D and D' bands are a measure of the density of scattering defects in the sample.

The G peak (appearing at 1582 cm^{-1}) is a doubly degenerate phonon mode at the Brillouin zone center (Γ). This peak is the most Raman like since it is a single resonance process. The G' (appearing at around 2700 cm^{-1}), D (appearing at around 1350 cm^{-1}), and D' (appearing at around 1600 cm^{-1}) peaks originate from a double resonance (DR) Raman process. The difference between them is that the D and D' bands are defect mediated process while the G' is not. Since the Raman shift for the G' band is twice as much as for the D band, and both are DR processes G' is sometimes called 2D band. The DR process for the G' (D) band is: (i) an electron-hole pair is excited with energy E_{laser} near the K point (ii) the electron is scattered by a phonon (defect) towards the K' point (iii) the electron is scattered again by a phonon to a $\vec{k}$ state (towards K point) (iv) electron-hole recombines emitting a photon that is detected for the Raman signal. The G' signal additionally shows a DR process where both the electron and hole are scattered towards K' and recombine then. Similarly, the D' band shows a DR intravalley process (small change in the wave vector keeps the process around the K point) with a defect mediated interaction. All processes are indicated in **Error! Reference source not found.**.

All Raman data on this thesis is taken with a NTegra Spectra NT-MDT RAMAN/NSOM system with laser wavelength of 532 nm and 1mW power.

3.2 GRAPHENE PROCESSING

3.2.1 Chemical Vapor Deposition

Graphene was first isolated by mechanical exfoliation of highly crystalline graphite. Scientific advances allowed the synthesis of graphene sheets by Chemical Vapor Deposition (CVD), a chemical process used to grow high quality thin film materials. A reacting substrate is exposed to precursor gas at high temperature. The precursors will decompose and react with the substrate surface forming a thin film. Precursor by-products are usually removed by inert gas-flow, or vacuum.[83]

For graphene, specifically, the most common precursors is methane gas (CH_4) and hydrogen gas (H_2) is used to assist the growth process. Methane gas is used as a carbon source that at high temperatures decomposes into carbon atoms and hydrogen molecules. Hydrogen gas has a dual role: as a co-catalyst in the formation of surface bound carbon, and a carbon etching reagent that regulates size and shape of the growth domain.[84] Essentially it promotes and regulates the adsorption of surface bound carbon atoms. The partial pressures of methane and hydrogen gas determine the growth rate of graphene, and typically hydrogen should have 100-200 times higher partial pressure. An inert gas such as argon can be used as carrier gas to aid the removal of methane by-products. It has been shown that the

shape of single crystals domains can be affected by changing the partial pressure of hydrogen with respect to the carrier gas.[85] Copper, Nickel or Tungsten foils are usual substrates, due to carbon atoms becoming surface bound with relatively low energy. Purity and roughness are important parameters for good quality graphene in these substrates.[86, 87] Finally, after growth a fast cooldown of the furnace allows for the carbon atoms to form covalent bonds without deforming the crystal structure.

There has been significant research in recent years towards graphene growth at the wafer scale.[88-90] There are many parameters that control the quality, overall size, and domains of the resulting graphene: chamber pressure and temperature, gas flow and partial pressures, substrate roughness and cleanliness. The graphene setup is shown in Figure 3.6a.

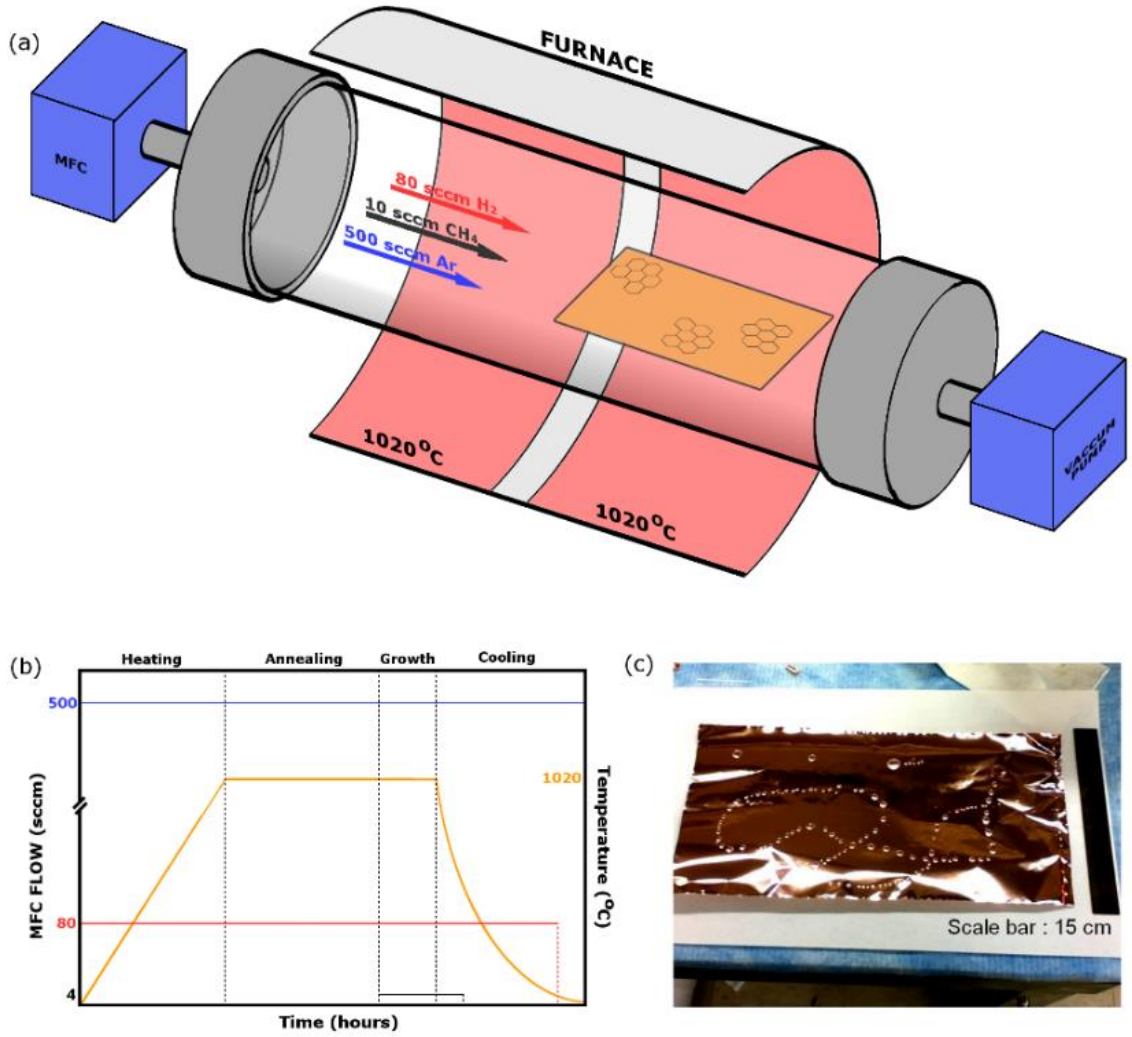

Figure 3.6: (a) Diagram of the graphene furnace used. MFC controllers are used to regulate the gas flow into the chamber. A vacuum pump maintains low pressure in the chamber and helps to remove reaction by-products. Methane gas is used as a precursor, Hydrogen gas as a regulator and Argon gas as a carrier. (b) Diagram of the growth recipe. Argon flow in blue, hydrogen flow in red, methane flow in black. Temperature profile in orange. (c) Picture of a copper foil with monolayer graphene as grown. Water droplets can easily form on the surface due to its hydrophobicity.

The furnace is a 4" Low Pressure CVD (LP-CVD: MTI Corp OTF-1200X-4-C4-SL-UL). Flow is regulated individually for each gas by Mass Flow Controllers (MTI Corp EQ-MFC-7B) and computer controlled using a 4-channel flow readout box (Sevenstar D08-4E). We use research grade (99.999% purity) gases: methane,

hydrogen, and argon. We developed a growth recipe (Figure 3.6b) that produces high quality graphene (~4000 cm^2/V-s mobilities and < 5 V Dirac voltage). The copper substrate is loaded and the chamber is put under vacuum, to approximately 50 mTorr. The chamber filled with 500 sccm of Ar and 80 sccm of H_2, and the furnace is then heated to 1020°C. We use a two-zone furnace, where the first zone is used to decompose the precursor gas before it arrives to the foil. The substrate is annealed under these conditions for 1 hour. Graphene growth is done under 5 sccm of methane for 5 min and 10 sccm for 15 min. The chamber is rapidly cooled, methane is turned off at 500 °C, and hydrogen at 80 °C.

Using a larger furnace without updating the growth parameters to adjust would usually not result in appropriate graphene growth. Figure 3.7 shows SEM images and Raman spectra for two graphene growth recipes. With unoptimized and optimized parameters, respectively. The SEM image shows that the unoptimized growth has islands of double layer graphene along the grain of the copper. This is confirmed by the Raman spectra that shows a G/G' ratio of approximately 1, this is characteristic of multilayer graphene. After optimizing parameters, the SEM image shows no traces of double layer. Raman shows a graphene like distribution with a G/G' ratio of 1/3.

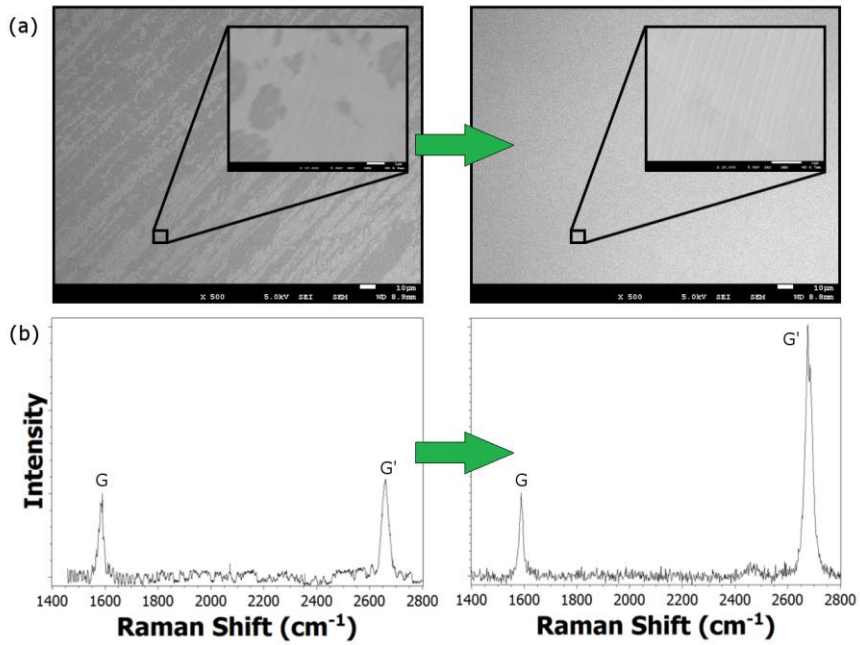

Figure 3.7: (a) SEM image of large scale graphene recipes. Inserts show a zoomed image of the same sample. Parameters as used for smaller scale growth (left), and after optimizing parameters (right) (b) Raman spectra for the unoptimized (left) and optimized (right) recipes. Peaks are normalized with the G peak, and have the same vertical scale.

3.2.2 Electrolysis Driven Transfer

It is necessary to be able to separate the copper from the graphene, to be able to transfer to an insulating substrate to fabricate GFETs. This can be done by either dissolving the copper using a metal etchant,[91] or by using electrolysis to drive copper separation ("bubble" transfer)[92]. However, hard acid etchants as the one used for copper can dope the graphene during the process. For this thesis, we will use the "bubble" method shown in Figure 3.8. We spin coat Michrochem 495 PMMA A4 at 2000 rpm for 60s on top of as grown copper/graphene, and cure it at 100^{o}C for 2m. A metal anode is submerged into a 0.05M solution of NaOH (passed through a 0.6 μm filter), while the cathode is connected to the copper/graphene/PMMA

structure. Bubbles will form at the interface between the graphene/PMMA and the copper, mechanical stress will separate both surfaces. The graphene/PMMA needs to be transferred through four baths of DI water to clean from impurities and can be scooped with the final substrate. A hard bake is done to promote adhesion between graphene and the final substrate, at 150 ºC for 2m. PMMA is removed with a short acetone bath for 4 min, followed by a long bath for 1 hour.

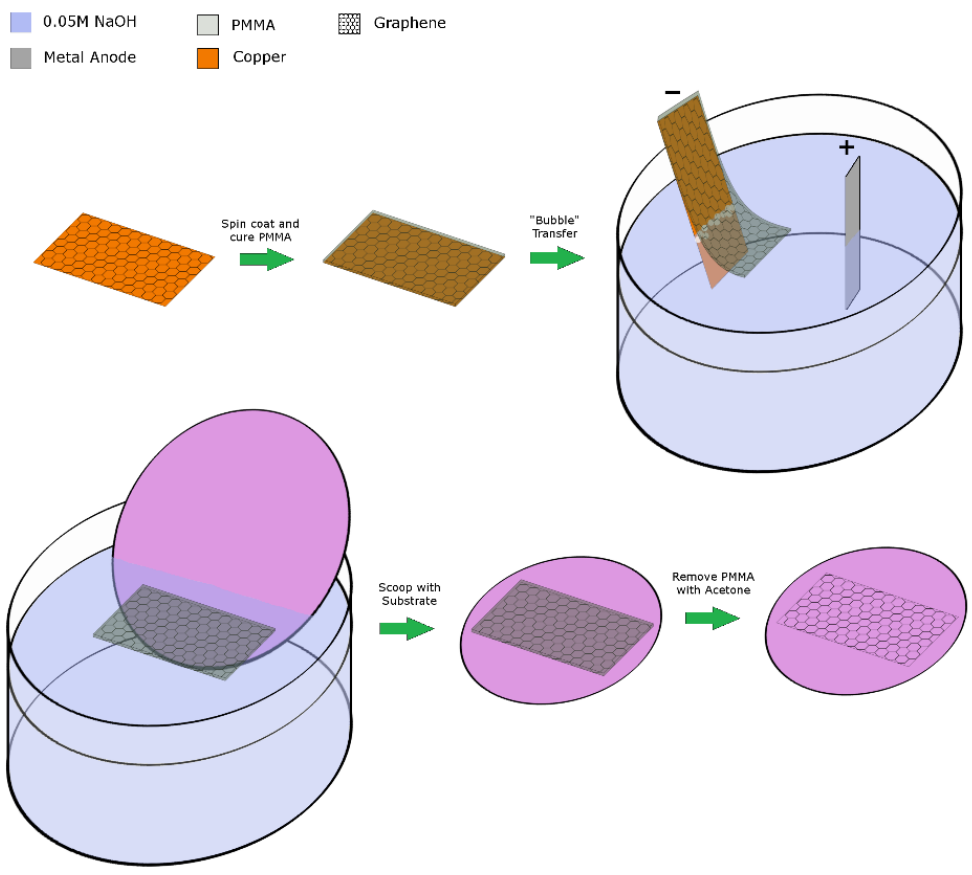

Figure 3.8: Schematic for electrolysis driven transfer. Copper foil is spin coated with PMMA. A bias is applied between the foil and a metal anode, that generates bubbles that mechanically separate the Graphene/PMMA from the copper foil. A substrate is used to scoop the Graphene/PMMA and acetone is used to remove the PMMA.

3.3 FABRICATION METHODS

In this subsection, we detail the fabrication procedure for GFETs. Each tool is described. Now we outline how each tool is used in the overall process. We start by Laser lithography used to print the photolithography masks. Photolithography is then used to define a metal contacts pattern on an industry standard Si/SiO_2 wafer, and thermal evaporation is used to deposit a 5 nm Cr adhesion layer and a 40 nm Au layer. HF is used to etch the back side of the wafer and thermal evaporation to deposit a 40 nm Au layer on the back side. A Physical vapor furnace is used to deposit a layer of HMDS that increases hydrophobicity and improves graphene properties.[93] Graphene is transferred on top of the metal contacts, and a second round of photolithography is done to define the channels. Oxygen plasma (RIE) is used to etch excess graphene, before resist lift off. The entire fabrication process is done at a wafer scale. The wafer can then be cleaved to individual chips and GFET arrays are then cleaned by annealing.

3.3.1 Laser Lithography

Laser Lithography (LL) is fabrication method by which a design can directly be printed on a polymer (photoresist) coating a substrate. This system has a slow throughput, but it is highly flexible and versatile.[94] LL can be used to print a design directly into a wafer, this allows for quick turnaround during an iterative design process. Alternatively, it can also be used to print masks for photolithography (photo-masks) where the initial substrate is a transparent crystal coated with a

reflective metal (*i.e.* soda lime glass coated with chrome). The system uses a laser with appropriate wavelength to interact the photoresist on the target spot. Once the pattern is printed on the substrate, a specially designed chemical with low pH that will only remove the exposed regions for positive resist (non-exposed regions for negative photoresist) develops the pattern. This allows further processing of the sample. For photo-masks we then remove the metal coating under the exposed regions with an appropriate etchant. Finally, the photoresist is removed completely with a specially designed organic solvent during a lift-off step.

Designs were done with Layout Editor, and converted to the printer format with BEAMER software. We used A HEIDELBERG DWL66+ to print a pattern into SODA LIME GLASS/CHROME photolithography mask coated with AZ1500 resist. The laser printer uses a 40 mm focal length lens to create a 2 μm spot size, which is below the Minimum Feature Size (MFS) of 10 μm. All designs in this thesis are a four-quadrant array, with metal pads on the edge of the chip. However, the specific parameters of the array (number of devices, 2/4-probe, etc.) differ on each project. The photo-mask is developed in MF319 for 1 min, and Remover PG overnight to clean them after chrome etching. There are two types of photo-masks: First, “dark field” if it is mostly metalized with some apertures cleared through the process. Second, “bright field” if it is mostly clear with some regions left metalized through the process.

3.3.2 Photolithography

Photolithography is a process that can be used to transfer a pattern from a master image (printed onto a glass/chrome mask) to photoresist coated substrate.[95] The equipment used for photolithography are known as Mask Aligners. For this tool a UV source, usually a Hg lamp with h-line and i-line filters are used as a light source. The light is exposed onto the sample with the photo-mask between them. Some regions will have illuminated and others will be blocked by the unetched chrome regions in the mask. The important parameters for the exposure are the contact type, wavelength of the light and the total energy per unit area during exposure (dose). After lithography, the pattern is then developed to allow further processing and the final step is always a lift-off to remove all resist from the sample.

There have been recent efforts to obtain a scalable fabrication process for graphene.[96-98] Our fabrication process uses two photolithography steps, done on a SUSS MicroTec MA-6 MASK ALIGNER. First, we define the metal contacts for the array. A 400 nm layer (4000 rpm/45 s) of PMGI (Microchem) is spin coated to a bare Si/SiO_2(250 nm) wafer, and cured at 210ºC for 5 min. Then, a second 1.5 μm layer (5000 rpm/45 s) of 1813 (Shipley) is spin coated on top of the previous resist, and cured at 115 ºC for 2 min. A photolithography exposure is done in hard contact mode at a dose of 140 mJ/cm^2 using a dark field photolithography mask. The sample is developed on MF319 for 1 min. After metallization, substrate treatment and graphene transfer we define the pattern for the graphene channels. A 400 nm layer

of PMGI is spin coated to the graphene/metalized wafer sample, and cured at 125ºC for 5m. The lower temperature is to avoid adhesion between the photoresist and the graphene. The second resist layer is a 1.5 μm of 1813, cured at 115 ºC. The exposure is done at soft contact mode at a dose of 140 mJ/cm^2 using a bright field photolithography mask. The sample is developed on MF319 for 1m. Second, after metallization, substrate treatment and graphene transfer we define the pattern for the graphene channels.

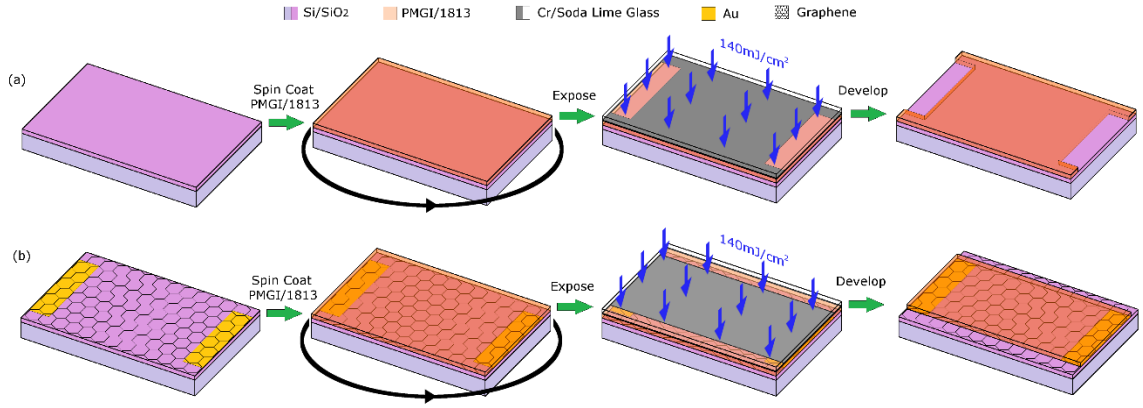

Figure 3.9: Schematic of the photolithography process (a) for a wafer to print an array of metal contacts to define the GFET source/drain (b) wafer after metallization, treatment and graphene transfer to define the GFET channel.

3.3.3 Physical Vapor Deposition

We will detail two types of film deposition. The first one used after the first photolithography step to deposit a thin layer of metal onto the wafer. This layer is referred to as the metallization and is used for the GFET electrodes. It can either be done by thermal heating or by electron beam.[99] A metal evaporator is a low vacuum chamber, with pressure usually on the μTorr range, with a heating element that turns a metal source into vapor. The metal source can be heated, either thermally by a

high current flow through a tungsten boat, or by a beam of electrons while the source is on an insulating crucible. The low pressure ensures that the mean free path (l) of the evaporated metal is large enough to reach the sample at the top of the chamber, l is typically a few meters for the range of pressures used in the equipment and the sample is located closer than that range. The evaporated particles move isotropically and deposit in an even layer across the sample, typically with a resist layer on it. The resist is later removed by lift-off with an appropriate solvent (Figure 3.10).

We used a KURT LESKER PVD75, thermal evaporator. To deposit a 5 nm adhesion layer of 98% Cr (reacts with SiO_2 to oxidize), and a 40 nm layer 99.9% gold. Process pressure was 2 μTorr. And, Lift-Off was a 5 min sonication on Remover PG followed by an overnight soak.

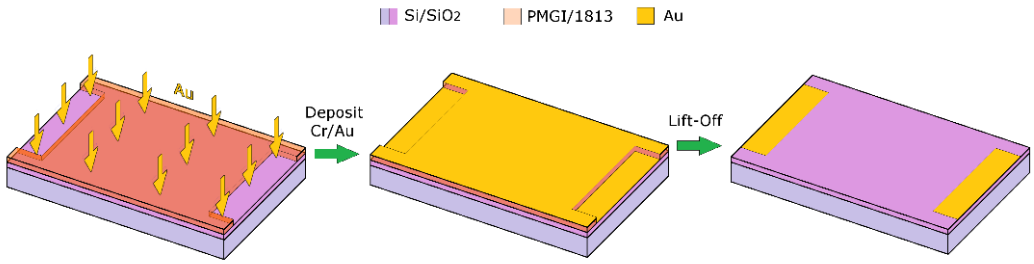

Figure 3.10: Process for electrode metalization. Wafer with resist after photolithography is placed on the chamber and a layer of Cr/Au is evaporated. The resist is cleaned by an appropriate solvent to remove excess metal from the depositon.

It has been reported that the hydrophobicity of the material as well as trapped charges in SiO_2 can negatively impact graphene electronic properties such as mobility and Dirac voltage, Bis(trimethylsilyl)amine (HMDS) can be used to decrease these effects.[93] While HMDS can be layered in a liquid state by spin

coating, best results are usually obtained in the gas phase. We use a YES EcoCoat 1224P Vapor Phase Oven to deposit a thin layer of HMDS onto a metallized wafer. Silane groups on HMDS react readily with SiO_2 and leave the metalized surfaces bare, this increases the hydrophobicity of the substrate and shields the trapped charges on the oxide.

3.3.4 Reactive Ion Etching

Reactive Ion Etching (RIE) is a process of material removal that utilizes bombardment of chemically reactive high energy ions (plasma) onto the sample. An electromagnetic field applied to a low pressure, gas filled, chamber generates plasma. Most common equipment is a parallel plate RIE, simply called RIE, where an electric field is used to react the gas into a plasma. Typically, the electric field is oscillating which causes repeated bombardment of the plasma ions. It has been shown that long exposures of oxygen plasma will deteriorate and remove graphene from exposed areas.[100] We used a TECHNICS SERIES 800 RIE for all graphene etching. We used a vacuum pressure of 400 mTorr, and when Oxygen gas was introduced pressure increased to 1.25 Torr. The etching process was, 50 Watt power for 35 sec. We found that after RIE graphene was almost completely removed, however a hardening of the resist had occurred. Lift-off was done using a Remover PG soak with gentle agitation for 2 min, and a Remover PG soak for 8 min. This process ensures that all resist is removed, without removing the graphene channels that were protected by it (Figure 3.11).

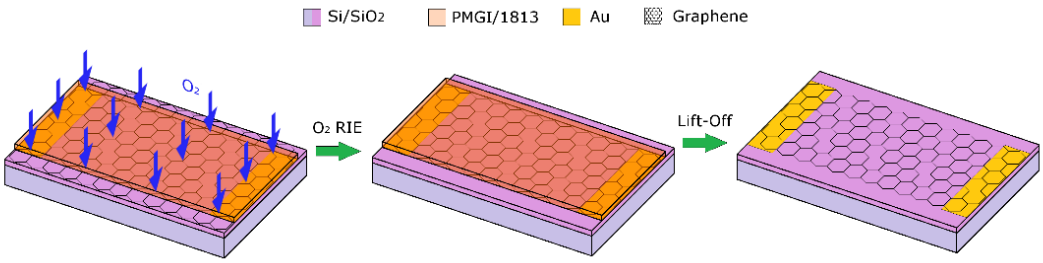

Figure 3.11: Reactive Ion Etching process. Wafer after graphene transfer and photolithography is exposed to oxygen plasma. Graphene is removed by plasma ions on the uncovered regions. Lift-Off removes the resist and leaves the graphene channel exposed.

3.3.5 Annealing

Cleanliness of GFETs is important for any electronic application, this is especially true for sensors where graphene is an electrical transductor. Impurities, residues from the fabrication process such as PMMA or PMGI can modify the electronic and chemical properties of graphene interfering with either the chemical signal or the electronic readout.[101] These residues can be treated with hydrogen annealing. The effect of PMMA can be shown by XPS, as in Figure 3.12. The sp^2 carbon bond is clearly the dominant signal. However, we can identify additional carbon peaks attributed to the PMMA structure.[10] The intensity of the PMMA peaks decreases for higher temperature, however we found out that for 225ºC we could obtain a clean surface without compromising the electrical characteristics of the GFETs.

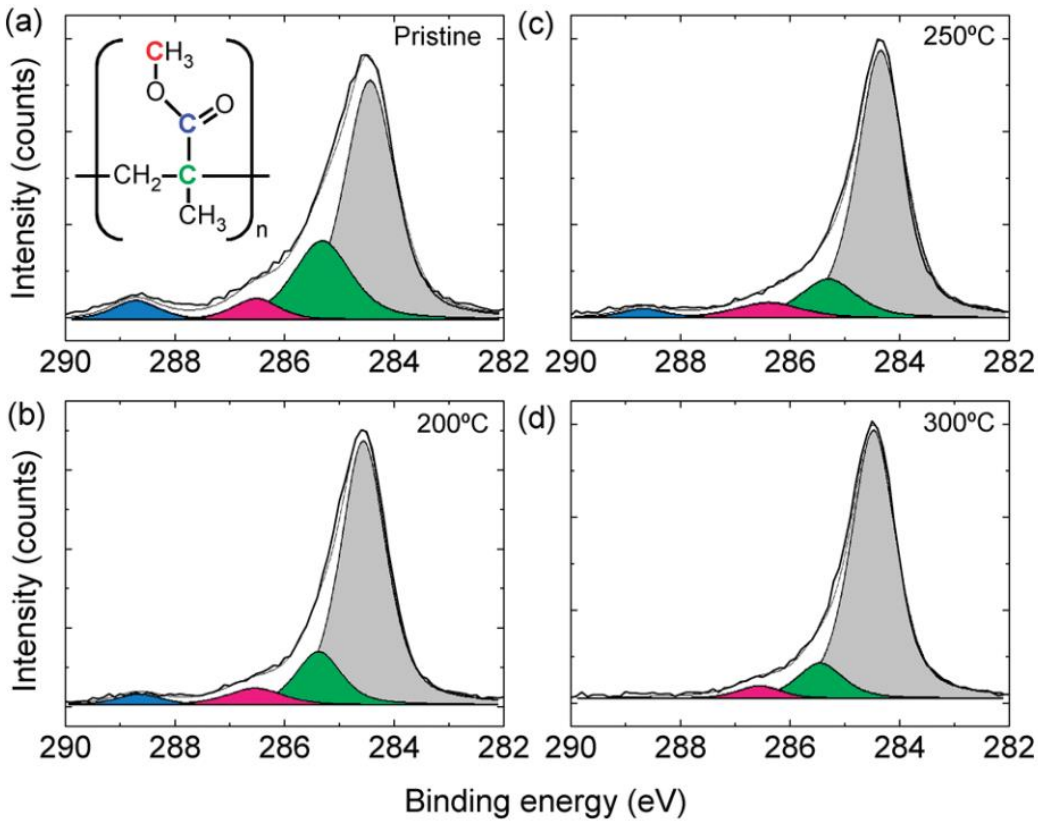

Figure 3.12: XPS Spectra of PMMA-transferred CVD graphene: (a) before annealing, and after annealing at (b) 200ºC, (c) 250ºC (d) 300ºC. The binding energy of the sp^2 carbon bonds (gray) is asigned at 284.4 eV for all curves. Other chemical shifts are atributed to the carbons in the PMMA structure (red, blue, green) respectively.[10]

We used a THERMO FISHER LINDBERG/BLUE M single zone tube furnace. This tube is not vacuum operated and as such it needs an inert gas to remove oxygen in the chamber. Once the samples are loaded into the tube and the end caps are secured to avoid any oxygen leakage we flow 1000 sccm of Ar and 250 sccm of H_2. The furnace is then heated to 225ºC and the samples are annealed for 1 h. A diagram of the furnace is shown in Figure 3.13.The samples are removed from the chamber after it has cooled to room temperature.

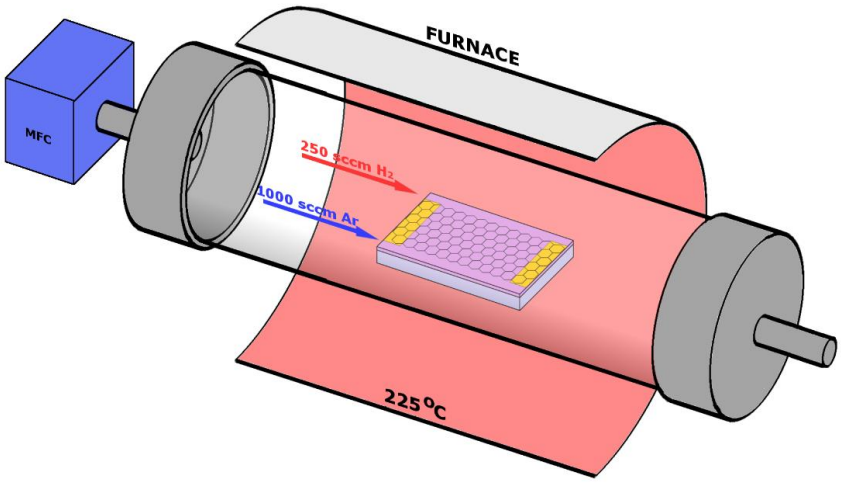

Figure 3.13: Diagram of an annealing furnace. A chip (or set of chips) are loaded into the tube chamber, close to the center of the heating zone. A constant flow of 1000 sccm Ar and 250 sccm H2 is applied. The furnace is heated to 225oC and the samples are annealed for 1 hour.

3.4 FUNCTIONALIZATION

It is necessary to the capability to bind to the desired biological molecule; this is often referred to as functionalization. All linking chemistries bind to the biomolecule by means of a succinimide ester reaction to an amine, as described in section 2.2.4. However, the chemical linkers must bind to graphene as well. Here we detail three methods to readily bind to graphene: non-covalent, covalent, and by nanoparticle (NP).

3.4.1 Azide Functionalization

Nitrenes are electron-deficient chemical species that are generated by either thermal or photochemical activation. Nitrene radicals can functionalize graphene very efficiently.[102] Perfluorophenyl nitrenes show enhanced bimolecular reactions, these are activated from perfluorophenyl azides (PFPA) which are specially

effective for functionalization. Upon light or thermal activation, the azide functionality dissociates into molecular nitrogen and a singlet nitrene species (Figure 3.14 top).[103] Fluorine substituents stabilize the nitrogen singlet, increasing its lifetime. PFPAs have been shown to have a highly efficient covalent binding to binding.[104, 105] The process occurs through the [2+1] cycloaddition of the nitrene into the graphene.[8]

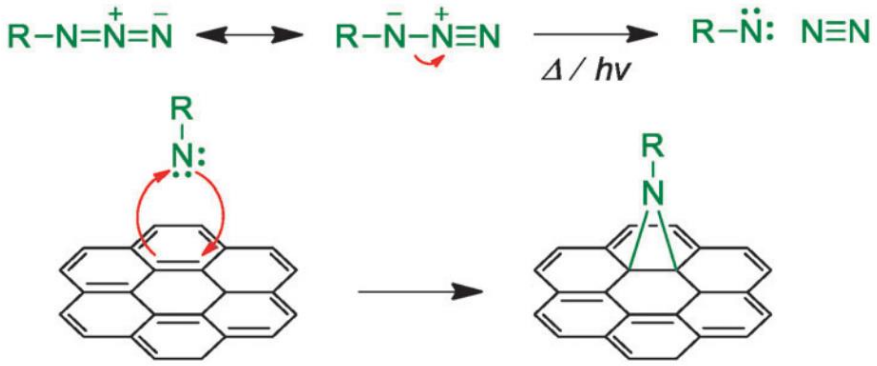

Figure 3.14: (top) Light (or thermal) activated decomposition of an Azide to a Nitrene (bottom) Cycloaddition of Nitrene onto graphene to form a covalent bond.[8]

Experiments in this thesis were based on the linker molecule 4-Azide-2,3,5,6-tetrafluorobenzoic acid, succinimidyl ester (Setareh Biotech 6977) (Azide-NHS), with a photoactivated PFPA and succinimide ester functions.

3.4.2 Pyrene Functionalization

Generally, covalent functionalization compromises the sp2 lattice structure. Depending on the nature of the covalent bond this might or might not affect electronic properties of graphene. In some cases, a noncovalent approach might be preferred. The noncovalent functionalization is mostly based on van der Waals

forces or π-π interactions with organic molecules or polymers.[106] The main mechanism used on our non-covalent linker molecule is π-π interactions. There are two requirements: the existence of π bonds, and enough geometry overlap to have a noticeable interaction. Pyrene is a polycyclic aromatic hydrocarbon that consists of four fused benzene rings, and shows a π-π stacking with graphene. This interaction is like the stacking of graphene sheets, carbon rings are intercalated in an AB structure.

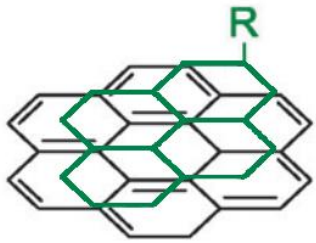

Figure 3.15: AB π-π stacking of a pyrene molecule with graphene. The interaction is similar to the interlayer stacking of graphene sheets.

Experiments in this thesis were based on the linker molecule 1-pyrenebutanoic acid succinimidyl ester (ThermoFisher Scientific P-130). Usually this molecule requires long incubation time to fully coat graphene due to the weak nature of the interacting forces.

3.4.3 Nanoparticle Mediated Functionalization

It is possible for amines in biomolecules to readily bind to a metallic nanoparticle (NP) instead of to a succinimide ester. Amines contain a lone pair, that can bind to the noble metal by donating an electron.[107] Density Functional Theory

(DFT) modelling shows a preference to Au-Au-N than to Au-N-C bonds due to a lower rotation angle energy.[108] This implies that it is not a nitrogen-carbon bond that determines the binding but rather the amine nitrogen by itself.

Noble metals are usually inert and chemically "uninteresting" in bulk form, at the Nano-scale a varied ligand chemistry is found. This is due to several possible oxidation scales present at the atomic scale, oxidation states from -I to +V are known.[9] The +I oxidation state is a linear ligand to the noble metal (ligand-noble metal-ligand) and relativistic effects are important in understanding these effects.[109] Figure 3.16 shows DFT computations of noble metal (+I) to thiolate complex; for copper (left), silver (right), and gold (right). The exact nature of the noble metal – thiolate complex bond can affect the geometry.

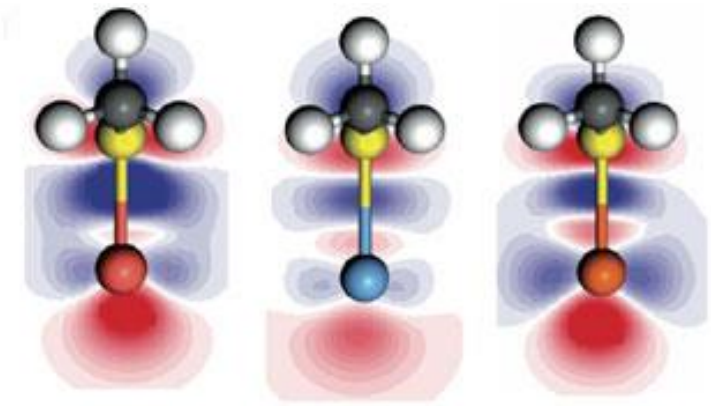

Figure 3.16: Density Functional Theory (DFT) computations for the noble metal – thiol complex bonding, for copper (left), silver (middle) and gold (right). All show some degree of covalence, copper is most polarized and gold is least polarized.[9]

We will use two NP-mediated functionalization methods. First, as an intermediate linker between two amines,[110] one bound to graphene and the other to

a biomolecule. Second, we create a monodisperse layer of nanoparticles by thermal annealing,[11] and readily bind amine modified biomolecules to them. The NP acts as an enhancement of the sensing signal since the graphene can detect electrostatic charge changes in close to its surface.[111]

3.5 SENSING

Sensors need good quality devices that transduce a response to a measurable output. After fabrication GFET arrays present excellent quality as shown by SEM, XPS, and Raman. Since GFETs will be used as electronic transducers, it is important to characterize the electrical properties of graphene. We measure the resistance of the graphene channel as a function of the applied gate voltage. The result is fitted to the model described in equation (2.12. Figure 3.17 shows the electrical responses for a single array after subtracting contact resistance, and the accumulated fitted values of Dirac voltage (0.5019 ± 2.712 V), and mobility (4952 ± 1682 $cm^2/V\text{-}s$) for all the arrays in a single wafer.

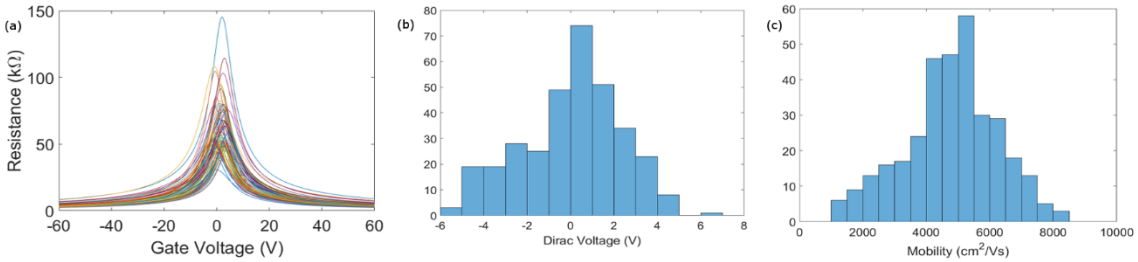

Figure 3.17: (a) Electrical response of a single GFET array. Resistance is measured as a function of gate voltage. (b) Dirac voltage, and (c) mobility; of all devices fabricated in a wafer calculated by mathematical modelling.

For our sensors, we use the Dirac voltage to track the target response. The Dirac voltage difference between the model response after the biomolecule and the target is calculated individually for each device. These average difference (within a standard error) have a correlation with the target concentration as described by Hill-Langmuir dynamics in equation (2.16).

3.6 SUMMARY

In this chapter, we review all the equipment and methodology used to gather and evaluate data. We start with a description of imaging tools, electrical characterization, and spectral analysis. Then, we outline the GFET fabrication process and detail each tool used: Photolithography of both metallization and graphene, as well as cleaning protocols through annealing. Third, we describe the type of linkers used in this project: covalent, noncovalent, and nanoparticle. Finally, we discuss the sensing process, this includes the requirements of graphene quality and yield as well as the most common data processing protocol.

4 NANOPARTICLE BASED SENSORS

This chapter outlines Nano/bio hybrid sensors that are functionalized with their biomolecules mediated by a noble metal nanoparticle (NP). First, we motivate this research and introduce previous NP/Graphene (NP-Gr) applications. We mention the limitations of previous approaches and outline the general advantages of the approach used here. Then, we detail two approaches on the methodology of NP deposition, and apply them to two different biomolecules. While this is done only on two projects it is possible to interchange the deposition method and biomolecules from the ones presented in this thesis. Four different sensors can be derived from this research; this highlights the flexibility of our approach towards NP mediated sensors.

We start by using a thermal evaporated layer of gold to form a monodisperse layer of gold nanoparticles on a GFET channel. The gold nanoparticles bind to the nucleotide bases and immobilize a single strand DNA (ssDNA) chain. A complementary chain can then be sensed. Then we report a novel strategy for scalable fabrication of arrays of graphene field effect transistors (GFETs) modified with PtNP and then functionalized with HER3-specific scFv antibodies, to demonstrate selective and sensitive detection of the breast cancer biomarker protein HER3 in buffer solution. The devices showed high sensitivity (~300 fg/mL limit of detection) and excellent specificity as indicated by multiple control experiments.

4.1 INTRODUCTION

Noble metal nanoparticle-graphene (NP-Gr) hybrid structures hold tremendous promise for label-free biosensing applications,[112-117] in which graphene functions as an ideal transducer due to its 2D nature, biocompatibility, and high carrier mobility. In contrast to linker molecules such as pyrene,[118, 119] diazonium[120] and BSA-streptavidin,[121] noble metal NPs allow simple, fast and efficient immobilization of the functionalized receptor molecules on the biosensors through covalent bonds.

So far most attempts have been devoted to biosensors based on reduced graphene oxide (rGO) for the detection of proteins,[112] microRNA,[117] and DNA oligomers.[116] Encouraging progress has been achieved, including nM-level detection of target DNA in real-time.[116] Despite the ease of preparation for rGO, it is difficult to control its thickness, uniformity and channel dimensions.[122] Consequently, device performance is frequently degraded compared to graphene-based devices, with low carrier mobility (<10 cm^2/V-s),[123] on-off ratio (< 2)[124] and yield. Dong *et al.*[115] reported on a DNA biosensor based on chemical vapor deposited (CVD) graphene) decorated with gold NPs. However, their process was focused on single device preparation and they did not report on process reproducibility, control of graphene channel dimensions, and electrical performance such as carrier mobility. There is currently no report on a scalable, reproducible, and high quality fabrication process of NP-GFETs.

4.2 MONODISPERSE GOLD NP MODIFIED GFET FOUR PROBE ARRAYS FOR ssDNA DETECTION

The results presented here have also appeared in: Ref 122.[125]

4.2.1 Abstract

We have developed a scalable fabrication process for production of DNA biosensors based on gold nanoparticle-decorated graphene field effect transistors (AuNP-GFETs), where monodisperse AuNPs are created through physical vapor deposition followed by thermal annealing. The FETs are created in a four-probe configuration, using an optimized bilayer photolithography process that yields chemically clean devices, as confirmed by XPS and AFM, with high carrier mobility (3590 ± 710 cm^2/V-s) and low unintended doping (Dirac voltages of 9.4 ± 2.7 V). The AuNP-GFETs were readily functionalized with thiolated probe DNA to yield DNA biosensors with a detection limit of 1 nM and high specificity against non-complementary DNA. Our work provides a pathway toward the scalable fabrication of high-performance AuNP-GFET devices for label-free nucleic acid testing in a realistic clinical setting.

4.2.2 Introduction

In this work, we demonstrate a novel, wafer-scale fabrication process for arrays of DNA biosensors based on AuNP-GFET measured in a four-probe configuration. The devices were of high quality, with hole mobilities of 3590 ± 710

cm^2/V-s and Dirac voltages of 9.4 ± 2.7 V. This approach thus offers significant performance advantages over the NP-rGO materials discussed above. The high quality is attributed in part to the use of a photolithography process that includes a polydimethylglutarimide (PMGI) protective layer,[126] which largely eliminates photoresist residues on the graphene channel, as confirmed by AFM, XPS, and electrical measurements. Physical deposition of a sub-monolayer of gold followed by thermal annealing was used to decorate the graphene with AuNPs with a high density (~ 400/μm^2) and relatively tight diameter distribution (5.3 ± 1.2 nm), enabling dense functionalization with thiolated probe single-stranded DNA oligomers. After exposure to target DNA, a positive Dirac voltage shift is observed whose magnitude varies with target concentration, in agreement with an electrostatic gating mechanism.[120] A detection limit of 1 nM was achieved, with good specificity against non-complementary ssDNA oligomers. This work provides a clear route to a scalable and reliable fabrication process for large arrays of high-performance AuNP-GFET devices, with potential applications for label-free DNA biosensors and immunoassays.

4.2.3 Materials and Methods

Graphene synthesis and Au deposition: Graphene synthesis was carried out by low-pressure chemical vapor deposition (OTF-1200X-4-C4-SL-UL, MTI Corp.). Cu foils (Alfa Aesar Item #46365) were cleaned with 5.4% HNO_3 for 40 seconds and two DI water baths for 2 min, and then blown dry with N_2 gas. The reaction chamber was pumped to a base

pressure of 50 mTorr. The Cu growth substrate was annealed at 1020 °C for 30 minutes with a gas flow of 500 sccm Ar and 80 sccm H_2. Monolayer graphene was then grown using methane as a carbon source at a flow rate of 5 sccm for 5 mins and then 10 sccm for 15 mins. The reactor was subsequently cooled to room temperature rapidly under a flow of 80 sccm H_2 and 10 sccm CH_4. A layer of gold was then deposited onto the graphene by thermal evaporation to a nominal thickness of 2 Å at a rate of 0.15 Å/s, as determined by a quartz crystal microbalance monitor.

AuNP-GFET sensor array fabrication: Standard photolithographic processing was used to define an electrode array for 24, four-probed graphene FETs on a highly p-doped Si wafer with a 300 nm thermal oxide layer. The contact metallization was 5 nm Cr / 40 nm Au, deposited by thermal evaporation. To minimize doping of the graphene FETs by substrate defects,[93] the electrode array was treated with HMDS to yield a hydrophobic surface. Gold covered graphene was transferred onto the metallized SiO_2/Si chip using the PMMA assisted "bubbling" transfer method.[2, 16] Briefly, PMMA coated Au/graphene/Cu was slowly immersed into a 0.05 M NaOH solution with a 20 V potential difference applied between the copper foil and the solution. PMMA supported Au/graphene was separated from the Cu foil by gas bubbles formed at the Cu surface. After three DI water baths, the PMMA/graphene film was transferred onto the metallized SiO_2/Si chip with the gold layer oriented away from the substrate, followed by air drying and baking at 150 ˚C for 3 minutes to enhance adhesion between the graphene and the substrate. After removal of PMMA with acetone, the chips were spin coated with a photoresist bilayer of PMGI (MicroChem Corp.) and S1813 (Shipley). Graphene channels were defined using by photolithography and oxygen plasma etching (Pressure: 1.25 Torr, Power: 50 W, Duration: 35 seconds). The

photoresist residue on graphene channels was removed by a N-Methyl Pyrrolidinone (NMP) based stripper (NANO^{TM} Remover PG, MicroChem Corp.), acetone and IPA to obtain the array of 24 FETs. Finally, the array was annealed in H_2/Ar forming gas at 225 ˚C to reduce photoresist residues and to allow the formation of relatively monodisperse AuNPs through a nucleation and growth process in which the free energy of Au clusters is minimized.[127]

SEM, AFM and XPS characterization: The morphology of the AuNPs was characterized by field-emission scanning electron microscopy (SEM, JEOL, 7500F) with an acceleration voltage of 18 kV. An atomic force microscope (AFM, Icon Bruker) equipped with a probe with a tip radius of <10 nm (TAP300Al-G, Budgetsensors) was used to characterize the topography of the AuNPs. The graphene surface was investigated by XPS using a customized XPS spectrometer (VG Scienta AB, Uppsala, Sweden).[128] XPS analyses were performed using a monochromatic Al Kα source (photon energy:1486.6 eV). The residual pressure in the analysis chamber was maintained at less than 10^{-8} Torr. The spectrometer was calibrated according to ISO 15472:2001 with an accuracy of ± 0.05 eV. Survey and high-resolution spectra were acquired in constant-analyzer-energy mode with pass energies of 200 and 100 eV, respectively. The spectra were processed using CasaXPS software (v.2.3.16, Casa Software Ltd., Wilmslow, Cheshire, U.K.). Background subtraction was performed using the Shirley−Sherwood method. The quantitative evaluation of XPS data was based on integrated intensity using a first-principles model and applying Powell's equation.[78]

Functionalization with probe DNA and testing against target or control solutions: Arrays of AuNP-GFET sensors were incubated in 1 µM aqueous solution of

thiolated probe DNA with a T_{10} spacer between the recognition sequence and the thiol functional group[129] ((SH)-TTTTTTTTTTAGCCGGGCGAGATACCCAATGCGC (5' to 3')) in DI water for 1 hour in a humid atmosphere to suppress the evaporation of the DNA solution. The array was then treated with 0.1% Tween 20 aqueous solution for 1 hour to remove probe DNA adsorbed nonspecifically on the graphene and to act as a blocker against non-specific binding of target DNA. This was followed by washing with two 0.05% Tween 20 solution baths and one DI water bath (2 min each) and drying with N_2 gas. After electrical measurement, the probe DNA-immobilized AuNP-GFET devices were immersed in 12 mL of complementary target DNA (cDNA) (GCGCATTGGGTATCTCGCCCGGCT (5' to 3')) or a control solution of non-complementary DNA (non-cDNA) (CTTCTGTCTTGATGTTTGTCAAAC (5' to 3')) of different concentrations in 0.1 % Tween 20 solution for 2.5 hours to allow for DNA hybridization. The devices were washed with two 0.05% Tween 20 solution baths and one DI water bath, followed by drying with N_2 gas before measurement of the electrical properties.

Electrical measurement and evaluation: Electrical measurements were performed under ambient conditions in a probe station equipped with a probe card that can measure 24 devices simultaneously. Conductivity-gate voltage (σ-V_g) measurements were carried out using a Keithley 2400 sourcemeter, with a bias current of 10 μA, with a four-probe geometry (Figure 4.1c) to eliminate the effect of the contact resistance or Schottky barriers formed at the graphene-electrode interface[130]. The gate voltage was applied using a Keithley 6487 voltage source. Dirac point voltage and hole carrier mobility were extracted by fitting the hole branch of the σ-V_g curve to the equation (4.1)[47, 131, 132]:

$$\sigma^{-1}{}_{(V_g)} = [\mu c_g (V_D - V_g)]^{-1} + {\sigma_s}^{-1} \tag{4.1}$$

where c_g is the gate capacitance per unit area for the 300nm thick SiO_2 (11.5 nF/cm^2), μ is the hole carrier mobility, V_D is the Dirac voltage, and σ_s is the saturation conductivity as $V_g \to -\infty$. This is a simplified equation derived from (2.12, where n_0 and R_s are zero.

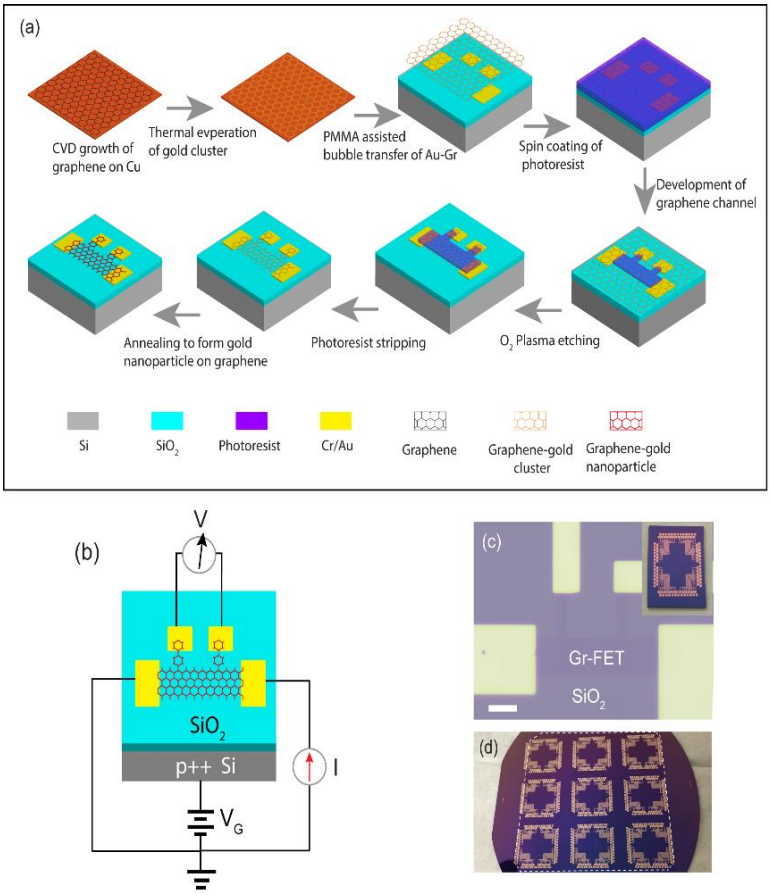

Figure 4.1: (a) Schematic showing the AuNp-GFET fabrication process. A gold layer is deposited onto CVD graphene. The gold-graphene layer is coated with PMMA and transferred. GFET channels are patterned using photolithography followed by oxygen plasma etching. Finally, the photoresist is removed, and the array is annealed to form AuNPs on the graphene. (b) Schematic of the four-probe conductivity-gate voltage measurement set up. (c) Optical micrograph showing an individual four-probed GFET device. Inset: Optical image of a chip with 24 Au-GFET devices. (d) Optical image of a 4-inch wafer with 9 electrode arrays and a transferred graphene monolayer that covers the full region defined by the arrays (dashed line).

4.2.4 Results and Discussion

Figure 4.1a shows a schematic of the sensor array fabrication process; details are provided in the Methods section. The process is designed for fabrication of nine arrays, each consisting of 24 devices in a four-probe configuration, on a 4-inch wafer (Figure 4.1b-d). Fabrication included the use of a resist bilayer (PMGI protective layer and S1813 imaging layer) to reduce photoresist residues on the graphene and thereby improve the performance of the FETs. The effectiveness of this approach was assessed by AFM, XPS, and electrical characterization of graphene FETs without AuNP decoration. When the photolithography process included only S1813, considerable contamination was observed by AFM (Figure 4.2a, lower panel), while no evidence of a residue layer was found for a similar sample processed using the bilayer process ((Figure 4.2a, upper panel). Electrical characterizations were used to confirm these results, the σ-V_g curves show higher mobility and a more symmetric behavior between their conducting branches for samples with the PMGI protective layer.

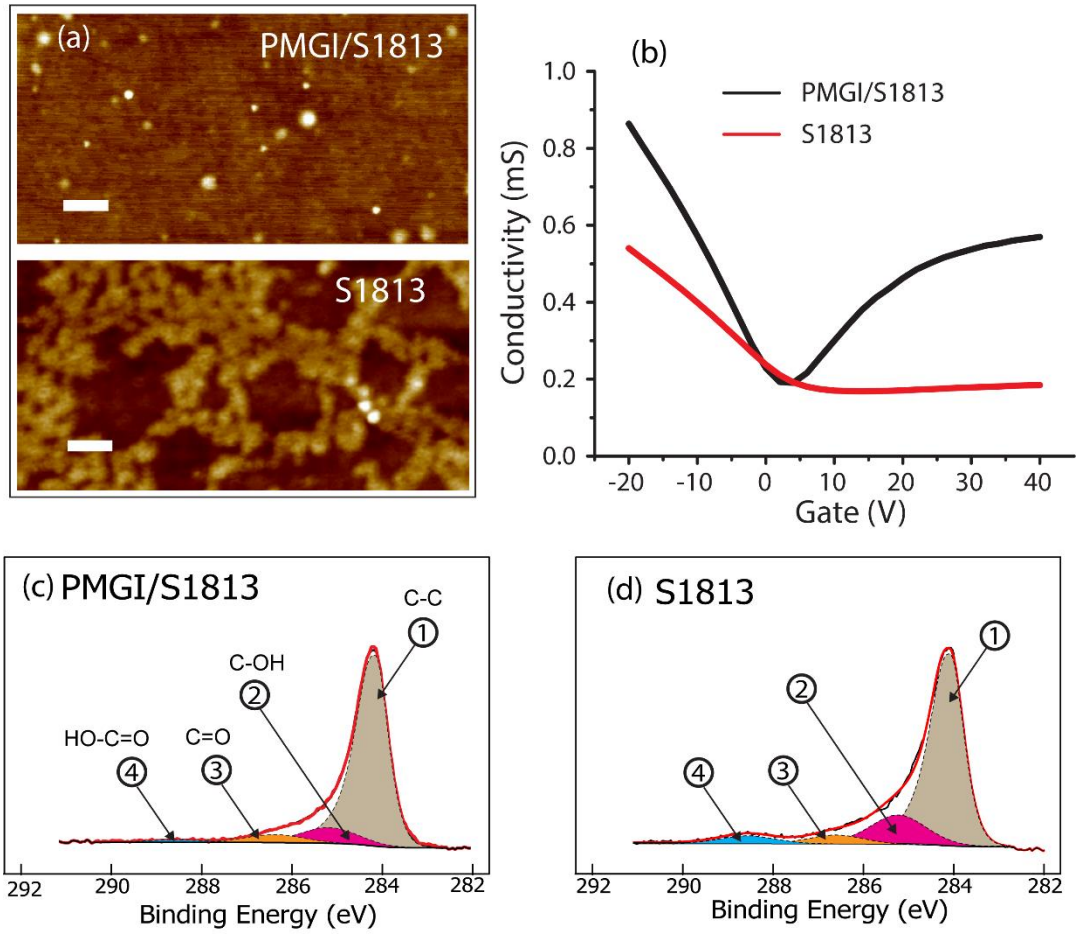

Figure 4.2: Measurements of photoresist contamination on graphene after photolithographic processing. (a) AFM images of the Gr-FET surface after photolithography and thermal annealing. The bilayer process results in low surface contamination (top image), and single layer process leaves significant residue on the surface (bottom image). Scale bar is 100 nm. Vertical color scale is 5 nm. (b) σ-Vg curve of Gr-FETs fabricated using and a single layer (red). (c-d) XPS spectra of the C1s regions for the samples processed using PMGI/S1813 (panel c) and S1813 (panel d). Both spectra are normalized to Peak 1. Peaks 2-4 are significantly reduced in the spectrum from the sample processed using PMGI/S1813, indicating a lower level of chemical contamination.

To confirm the chemical identity of the residue, a quantitative XPS analysis of the graphene surface was performed before and after photolithographic processing. The overview XPS spectra shows that the dominant elemental components (Si, C, O) were the same before and after photolithography. On a finer

scale (Fig. S2), the C1s region of the spectrum (~282-292 eV) shows a main peak at 284.1 eV, associated with the sp^2 hybridized C-C bond of graphene, and three other peaks with chemical shifts of +1.3, +2.5, and +4.5 eV, which are assigned to C–OH, C=O and HO-C=O functional groups, respectively.[133]. Immediately after transfer, the relative integrated intensity of the satellite peaks compared to the main peak are 12.6 ± 1.8%, 5.8 ± 0.2%, and 3.0 ± 0.3%, which presumably reflects a very small amount of residue from the PMMA layer used during transfer. The graphene FET array processed using a single layer of S1813 (Fig. 2c), the intensities increased dramatically, approximately doubling, to 22.6 ± 0.5%, 8.5 ± 0.8%, and 7.4 ± 0.4%, confirming the presence of significant contamination. In contrast, the use of the bilayer resist scheme (Figure 4.2d) leads to negligible increase in the satellite peaks (13.7 ± 0.6 %, 6.4 ± 0.4 %, and 2.0 ± 0.1 %); in fact, the peak associated with the HO-C=O functionality is reduced post processing. The XPS investigation thus confirms that PMGI acts as an effective protective layer in the photolithography process, resulting in a chemically cleaner surface for the GFET.

The electronic effect of the contamination was assessed using four-probed σ-V_g measurements of complete arrays of 24 graphene FETs processed using the two approaches (Figure 4.2b). The σ-V_g curve for the FET fabricated using the bilayer process shows symmetry between the hole and electron branches, and analysis of measurements of a full array show high hole carrier mobility of 3720 ± 170 cm^2/V-s and electron mobility of 3100 ± 450 cm^2/V-s and low doping as indicated by the

Dirac voltage of 5.2 ± 0.5 V. In contrast, the σ-V_g curve for the FET processed using a single layer of S1813 is strongly asymmetric, with significantly lower mobility (hole: 1860 ± 250 cm^2/V-s, electron: 390 ± 290 cm^2/V-s) and greater doping (Dirac voltage of 11.6 ± 1.5 V). These observations are attributed to the fact that conventional imaging photoresists such as S1813 contain aromatic components that can bind strongly to the graphene surface through π-π stacking interactions[126, 134] and degrade the electrical performance of graphene FETs. PMGI, which is free of Novolac resin, can act as a protective layer for the graphene and reduce the photoresist residues. A similar method has previously been shown to effectively reduce the contaminant layer of photoresist on carbon nanotube FETs.[126] Our process therefore provides a strategy for cost-effective, large-scale fabrication of high-performance graphene FET arrays and compares very favorably with other reports of graphene FETs produced by photolithography, where the hole carrier mobility is typically lower than 2500 cm^2/V-s.[97, 135]

SEM shows that thermal deposition of 2Å of gold on to graphene led to the formation of small gold clusters on the surface (Figure 4.3a). After definition of the FET channels, these gold clusters were transformed by annealing into nanoparticles with a uniform number density of ~ 400/μm^2 (Figure 4.3c). AFM topographic images (Figure 4.5a) show the nanoparticle size is 5.3 ± 1.2 nm (Figure 4.5b).

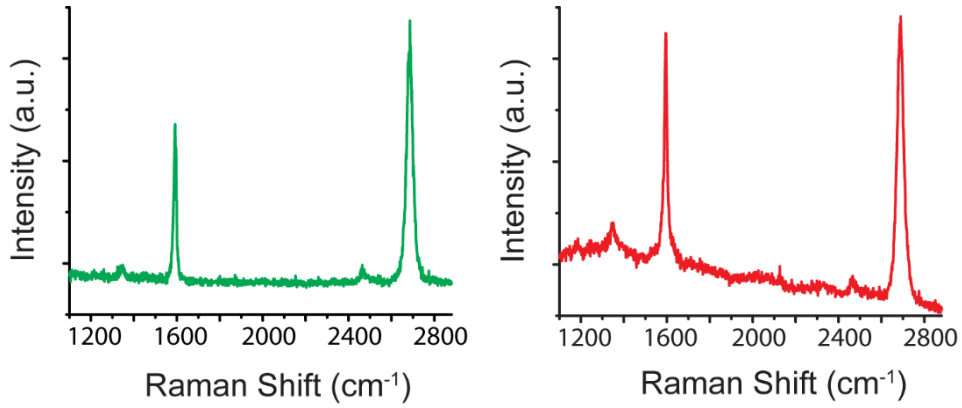

Figure 4.4: (left) Raman spectrum of graphene after photolithographic processing using bilayer PMGI/S1813. (right) Raman spectrum of AuNP-Gr hybrid layer after bubble transfer onto the SiO2 substrate and thermal annealing.

The Raman spectrum (Figure 4.4) of the AuNP-Gr hybrid layer reveals a 2D band located at 2689 cm^{-1} with a Lorentzian full-width at half-maximum (FWHM) of 51 cm^{-1}, larger than that of the bare graphene (31 cm^{-1}), indicating that the graphene is doped by the AuNPs.[136] The Raman spectrum also shows a very small D band at ~1346 cm^{-1}, with I_D/I_G ratio of ~0.11, slightly larger than that of the pristine graphene (I_D/I_G ~ 0.07). This low I_D/I_G ratio suggests that the hybrid AuNP-Gr layer retains its high material quality.[135]

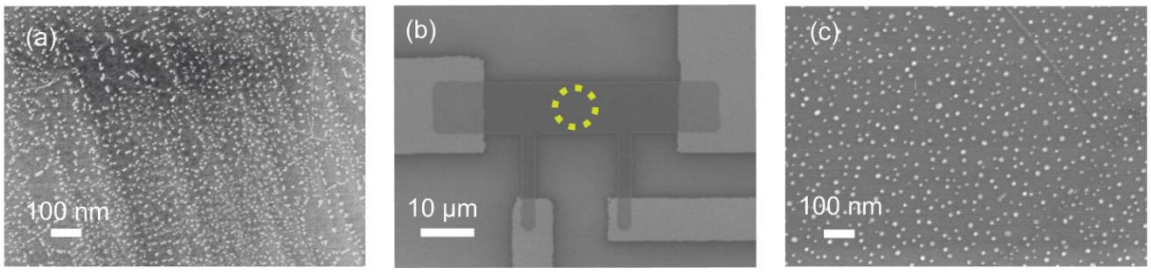

Figure 4.3: (a) SEM image of graphene after thermal evaporation of a gold layer shows the formation of small (~2 Å thick) Au clusters. (b) SEM image showing the four-probe AuNP-GFET, where gold electrodes contact the graphene from below. (c) SEM image of the highlighted area in (b), showing a uniform distribution of AuNPs. The number density is approximately 400/μm2, consistent with the AFM characterization

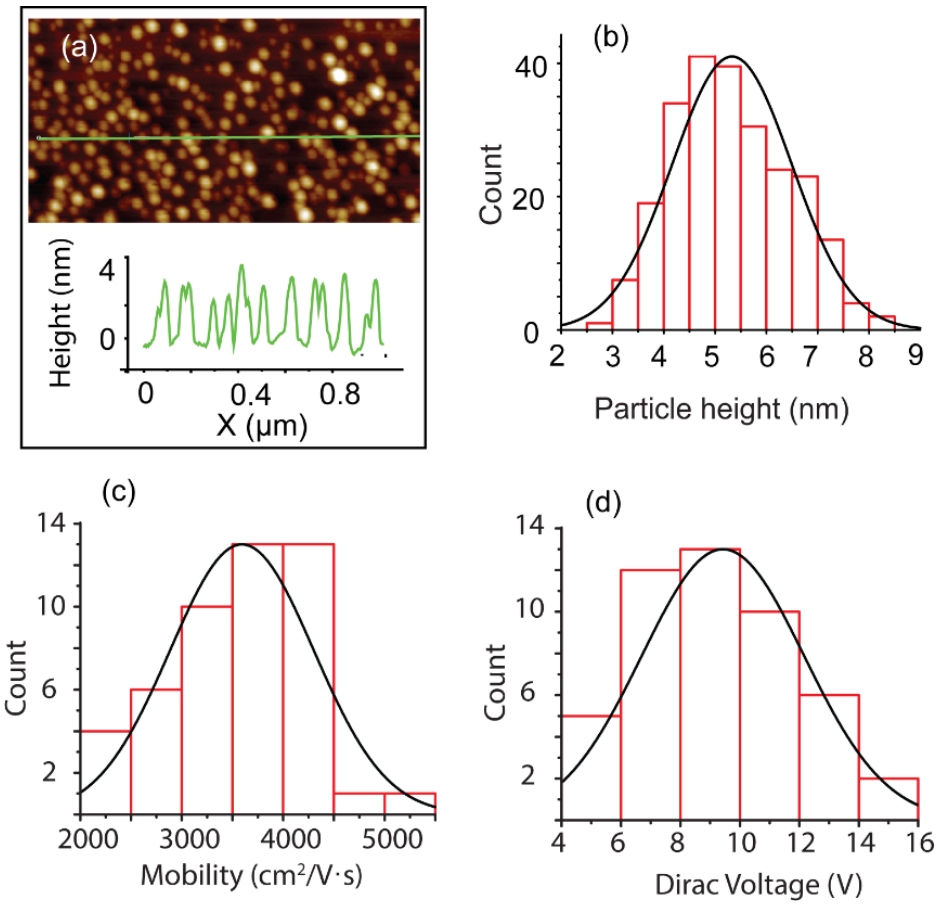

Figure 4.5: (a) AFM image showing the formation of uniform AuNPs on graphene after annealing. The corresponding AFM line scan is shown below the AFM image. (b) AuNP size distribution. The AuNP diameter is 5.3 ± 1.2 nm. Histograms of (c) hole mobility and (d) Dirac voltage with Gaussian fits (black curve) of AuNP-Gr-FETs based on three separate arrays, with 24 devices each.

Four-probe σ-V_g measurements conducted on AuNP-GFET arrays to confirm graphene quality. Mobility is calculated at 3590 ± 710 cm^2/V-s (Figure 4.5c), only slightly less than the value found for undecorated GFET devices. Compared to earlier reports on AuNP-rGOFETs,[123] AuNP-GFETs show superior performance, with mobility more than two orders of magnitude higher; indeed, the mobility values reported here are to our knowledge the highest to date for metal NP-Graphene hybrid structures. The Dirac voltage of the AuNP-Gr-FET shows a

positive shift to 9.4 ± 2.7 V (Figure 4.5d) higher than devices without AuNPs (5.2 ± 0.5 V), corresponding to an induced dopant density of ~ 3.0×10^{11} cm^{-2} due to the AuNP decoration. This effect is ascribed to the work function difference between graphene (~4.66 eV)[137] and gold (5.1-5.47 eV) which leads to graphene p-doping.

To complete the fabrication of the DNA biosensor (Figure 4.6a), the nanoparticles were functionalized with thiolated probe DNA by application of a 1 μM solution in DI water. Devices were treated with a solution of 0.1% Tween 20 in DI water in order to block exposed graphene that would enable undesirable non-specific binding of arbitrary DNA oligomers.[138, 139] Tween 20 is a nonionic surfactant with good affinity for graphene that has been reported to deter non-specific binding of proteins on carbon nanotubes[140] and bacterial cells on rGO.[141] Tween 20 is also used in PCR-ELISA to reduce non-specific binding of analyte DNA to enable detection of a specific PCR product. Four-probe σ-V_g measurements were conducted after each step. As shown in Fig. 4b, treatment with probe DNA led to a significant increase in the Dirac voltage (ΔV_D =59.6 ± 3.2 V), attributed to the chemical-gating effect[132] of probe-DNA molecules that become negatively charged due to ionization of phosphate groups in residual water. Mobility of the AuNP-Gr FET was also reduced by ~70 % to 1100 ± 360 cm^2/V-s, presumably due to scattering associated with the bound, negatively charged DNA. Application of the Tween 20 blocker led to a negative Dirac voltage shift of 16.0 ± 2.2 V and an increase in carrier mobility to 1470 ± 60 cm^2/V-s, both consistent with the

expectation that Tween 20 saturates the graphene surface and displaces nonspecifically bound probe DNA. Assuming chemical gating of 34 negative charges for each probe oligomer, the density of immobilized probe DNA is ~ 850 /μm^2, corresponding to about two probe DNA oligomers per AuNP.

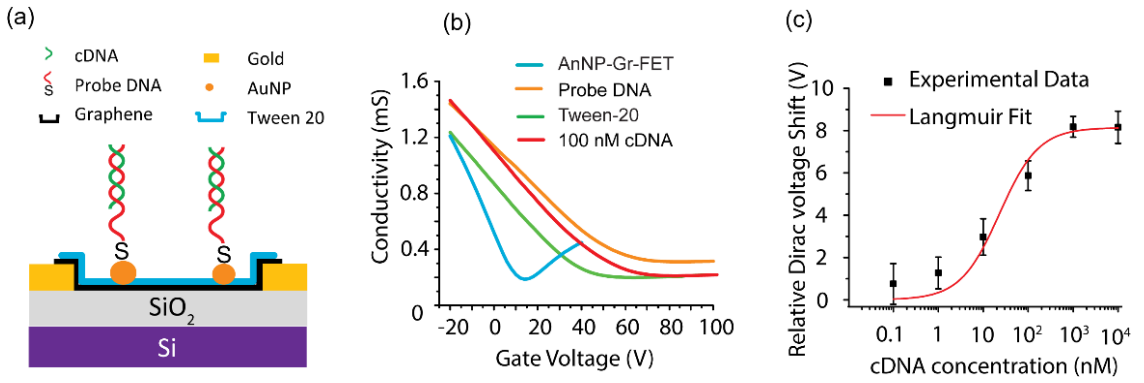

Figure 4.6: (a) Schematic of the AuNP-GFET DNA biosensor. (b) σ-Vg curves after chemical functionalization and exposure to target cDNA. After functionalization with probe DNA and Tween-20 blocker, exposure to 100 nM cDNA leads to a Dirac voltage shift of 13.6 V (green to red). (c) Sensor response as a function of cDNA concentration. The limit of detection is 1 nM.

Biosensor testing against target DNA was also carried out in 0.1% Tween, which allows specific binding of target oligomers with probe DNA to generate a sensor output but prevents undesirable non-specific binding of DNA on the graphene surface. To avoid cross-contamination, each array of biosensors was tested against a single concentration of complementary target DNA ("cDNA"). Figure 4.6b shows results from a typical experiment, where exposure to cDNA at a concentration of 100 nM in 0.1% Tween leads to a Dirac voltage shift of +13.6 ± 0.7 V. The sensor response for various concentrations of cDNA (c) is reported as ΔV_D^{rel}, the Dirac voltage shift relative to the shift measured upon exposure to 0.1%

Tween in DI water (+ 7.7 V). The data is consistent with an electrostatic gating mechanism,[130, 142] where hybridization of target cDNA with probe DNA on the AuNP provides additional chemical gating of the graphene FET channel. The measurements agree well with a Hill-Langmuir model.

$$\Delta V_D^{rel} = \frac{\frac{c}{K_a}}{1 + \frac{c}{K_a}} \tag{4.2}$$

where A is the maximum response with all binding sites occupied, c is the cDNA concentration, and K_a represents the concentration at which half of the available binding sites are occupied. The cooperativity n is set to 1. The best fit to the data yields values A = 8.2 ± 0.4 V; assuming chemical gating by 24 negative charges for each oligomer, the density of bound cDNA is ~250 μm^{-2}. Based on the probe DNA density inferred above, hybridization rate is ~30%, in good agreement with the expectation of 25-56% at room temperature .[143] K_a = 22.5 ± 9.4 nM, which is consistent with surface plasmon resonance experiments.[144] In a control experiment, a biosensor array tested against 1μM (random sequence) non-cDNA had a Dirac voltage shift of 7.7 ± 1.0 V, essentially identical to the Dirac voltage shift for pure buffer (0.1 % Tween in DI water), showing that the DNA biosensor has high specificity. The results suggest a limit of detection of approximately 1 nM (relative Dirac voltage shift of 1.3 ± 1 V) for this choice of cDNA.

4.2.5 Conclusion

In summary, a reproducible, high-quality fabrication process for large arrays of AuNP-GFETs has been developed. The devices are shown to be suitable for use as DNA biosensors. Fabrication incorporates chemical vapor deposited graphene with a thermally evaporated gold layer that through annealing forms nanoparticles, and an optimized photolithography process with a four probe design for the channel.

The fabrication process leads to AuNP-GFETs with mobility of 3590 ± 710 cm^2/V-s and a Dirac voltage of 9.4 ± 2.7 V. The photolithography step relies on the use of a PMGI layer that effectively avoids contamination of the graphene, as assessed by AFM and XPS. Annealing is used to form AuNPs on the graphene surface at a high density (~400/μm^2) with a tight diameter distribution (5.3 ± 1.2 nm). After attachment of probe ssDNA to the AuNPs, the devices act as DNA biosensors with high specificity against non-target DNA and a limit of detection of 1 nM. Similar experiments in rGO show lower mobility, yield and reliability.

The scalability and sensitivity of the AuNP-Gr-FET devices are potentially applicable for gene-expression investigations and label-free genetic diagnosis. The device structure should also be suitable for protein functionalization and immunoassay development.

4.3 PLATINUM NP MODIFIED NANOHYBRID GFET ARRAY FOR THE DETECTION OF BREAST CANCER BIOMARKER

The results presented here have also appeared in Ref 142.[145]

4.3.1 Abstract

Biosensors based on graphene field effect transistors (GFETs) decorated with antibody-functionalized platinum nanoparticles (PtNPs) are developed for the quantitative detection of breast cancer biomarker HER3. High-quality chemical vapor deposited (CVD) graphene is prepared and transferred over gold electrodes microfabricated on an SiO2/Si wafer to yield an array of 52 GFET devices. The GFETs are modified with PtNPs to obtain a hybrid nanostructure suitable for attachment of HER3-specific, genetically engineered thiol-containing single-chain variable fragment antibodies (scFv) to realize a biosensor for HER3. Physical and electrical characterization of Bio-GFET devices is carried out by TEM, AFM, Raman spectroscopy, and electrical measurements. A concentration-dependent response of the antigen is found in the range 300 fg/mL to 300 ng/mL and is in quantitative agreement with a model based on the Hill–Langmuir equation of equilibrium thermodynamics. Dissociation constant is estimated to be 800 pg/mL, indicating that the high affinity of the scFv is maintained after immobilization. The limit of detection is 300 fg/mL, showing the potential for PtNP-GFETs to be used in label-free biological sensors.

4.3.2 Introduction

Various techniques have been developed for cancer cell detection, including cytologic testing, fluorescent imaging, magnetic resonance imaging, computerized tomography, X-ray radiography, and ultrasound.[146-149] However, these techniques have disadvantages of high cost and long time required for either experimental process or instrumentation. Therefore, it is highly desirable to develop fast, and cost-effective methods for early detection of cancer cells in preclinical diagnosis for reduction in mortality for certain cancers. In this respect, point-of-care hand held devices offer promising alternatives to existing laboratory-based tests.

Electrical detection methods like field-effect transistor (FET) based biosensors exhibit highly sensitive detection of chemical and biological species when designed so surface–analyte or ligand–receptor binding occurs very close to the FET channel.[142] Carbon-based nanomaterials such as carbon nanotubes (CNTs),[150-155] reduced graphene oxide (rGO),[156] and graphene (Gr)[120, 157-161] have received considerable attention for label-free FET-biosensors with high sensitivity because of their unique electrical properties and suitability for miniaturization in an array format. Compared to CNT and rGO, large-area graphene grown by chemical vapor deposition (CVD) offers advantages of overall electrical conductivity,[162] device reproducibility, low noise, and superior carrier mobility,[163] which are expected to lead to greater sensitivity.

The direct immobilization of proteins on CNTs[140] or rGO[156] has been reported to be unstable and washed off easily (unless covalent immobilization through special surface treatment and additional steps of carbodiimide chemistry of protein binding is involved), which results in undesirable effects such as poor device sensitivity, poor reliability, and non-specificity of the sensor. This has been avoided by stable bimolecular immobilization through metal nanoparticles on graphene,[164] as their 3D geometry enables high bioreceptor loading with controlled orientation for ligand binding and thus are widely used in biosensing applications.[165, 166] In this work, we use platinum nanoparticles (PtNPs; Φ = 6.4 eV) instead of the more commonly used gold nanoparticles (AuNP; $\Phi \approx 5.3$ eV) because PtNPs are reported to provide improved electrical signals in CNT-based FET biosensors.[167, 168] This was attributed to enhanced electron transfer from the CNT channel (Φ = 4.9 eV) to the PtNPs, thereby increasing the hole carrier density, leading to improved biosensor characteristics. Since the transduction mechanism in FET-based biosensors is largely electrostatic,[16, 142] the use of single-chain variable fragment antibodies (scFvs; 2–3 nm in size) in place of conventional antibodies is expected to offer performance advantages.[152]

4.3.3 Results and Discussion

GFET devices were fabricated as described in the Experimental Section. Briefly, large-area monolayer graphene was prepared by low-pressure catalytic chemical vapor deposition process on a copper foil with CH_4 as a precursor source. The graphene thin film was then transferred using a polymethyl methacrylate (PMMA) assisted "bubbling" transfer method onto a pre-patterned SiO2/Si substrate with an array of 52 pairs of metal electrodes each having a dimension 100 μm wide separated with a 10 μm gap between the source and the drain electrode. After transfer, GFET channels were patterned using standard photolithography and oxygen plasma etching, as described in Figure 4.7. The GFETs were then annealed at 250 °C under flowing N_2 gas to remove residual photoresist contamination.

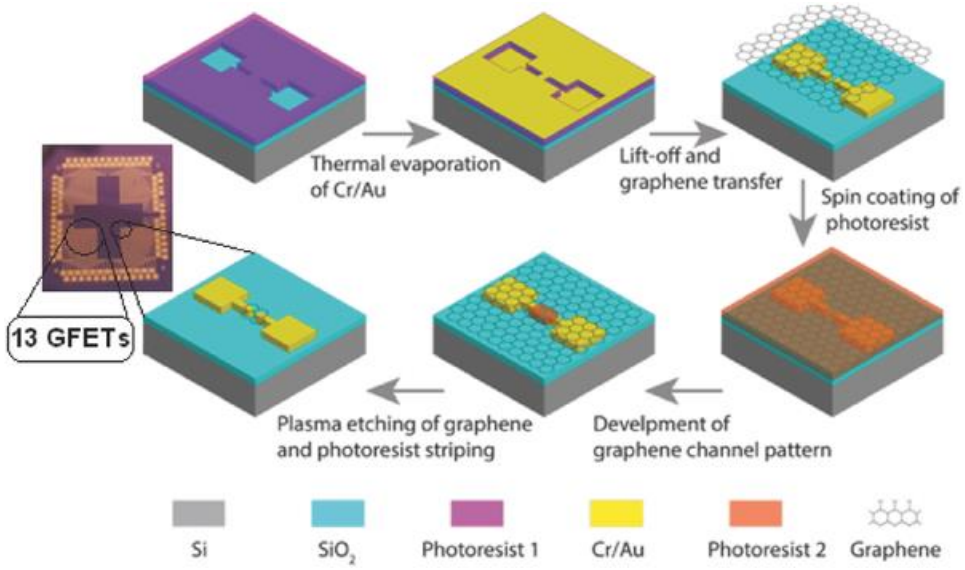

Figure 4.7: Schematic representation of fabrication process for an array of 52 GFETs. Metallization of contacts is done through photolithography patterning and a Cr/Au evaporation. Graphene is transferred by "bubbling" to the metallized wafer, and by a second round of photolithography and plasma etch the graphene channels are defined. Each array has a total of 52 GFET devices.

The Raman spectrum of the GFET channel showed the G band at 1580 cm^{-1} and the 2D band at 2670cm^{-1}, with an I_G/I_{2D} intensity ratio of 0.6 (Figure 4.8). The symmetric 2D peak was well fit by a single Lorentzian with a full width half-maximum of 31 cm^{-1}, and the D (disorder) peak located at ~1350 cm^{-1} was nearly undetectable. The spectra is indicative of a high-quality monolayer graphene[169, 170] channel in GFETs after processing.

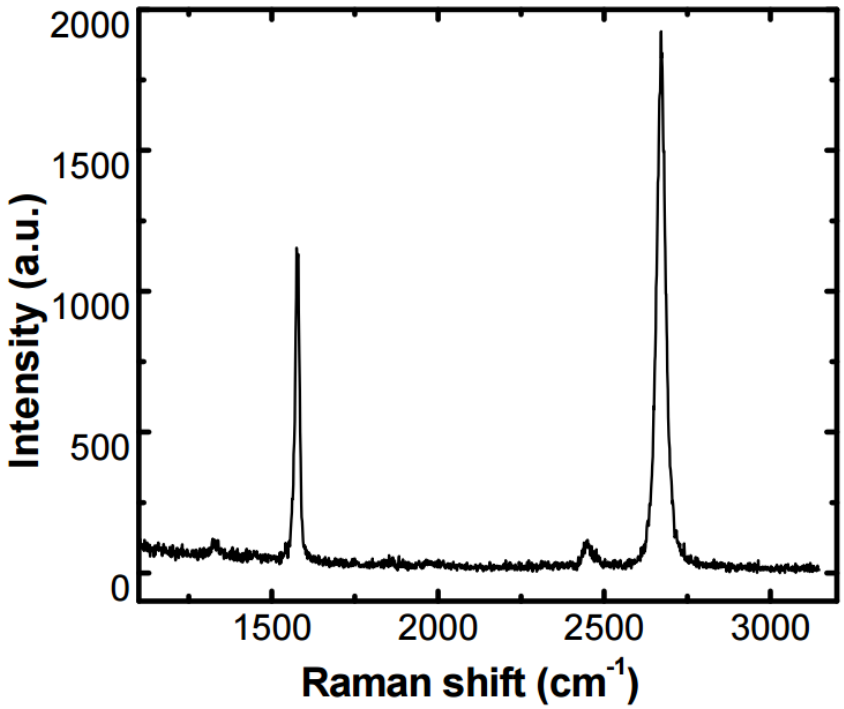

Figure 4.8: Raman spectra of CVD graphene transferred to Si/SiO_2 wafer. G peak is centered at 1580 cm^{-1} and the 2D band at 2670 cm^{-1}, with an IG/I2D intensity ratio of 0.6 and negligible D intensity, indicative of good quality, monolayer graphene.

The GFETs were first modified with PtNPs by using the bifunctional molecule, 1-methyl pyrene amine (Pyrene-NH2). The pyrene terminal binds to graphene via π–π interaction, and the amine terminal binds to the PtNP, as described in section 3.4.3.[107] High-resolution transmission electron microscopy (TEM) was

carried out on samples of graphene decorated with PtNPs by this method (Figure 4.9a) and showed that the small PtNPs were uniformly dispersed on the graphene surface. Typically, the size distribution of nanoparticle size varied between 1 nm and 3.7 nm, with an average size of about 1.8 nm and 2.4 nm. This has been further elucidated by scanning electron microscopy images (Figure 4.9b) showing PtNPs uniformly distributed without agglomeration over the entire graphene surface channel of the GFET.

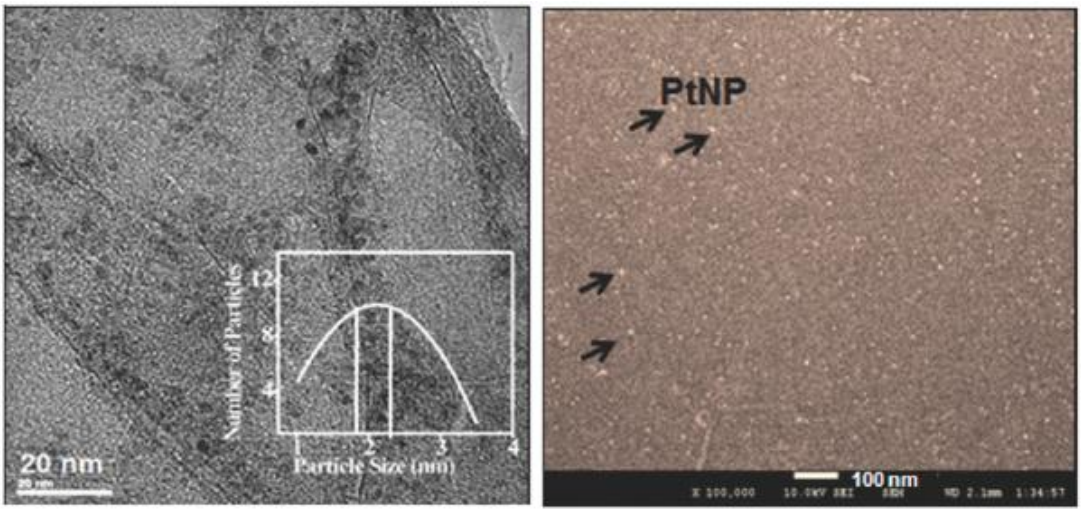

Figure 4.9: (a) TEM image of the PtNP-Gr structure. Inset: Size distribution of Pt nanoparticles, with an average size of about 1.8-2.4 nm. (b) SEM of a PtNP-Gr nanohybrid FET, 100 000X magnification and 10.0 kV accelerating voltage.

The PtNPs on the GFET were then functionalized by site-specific immobilization of HER3-specific scFv antibodies, which act as bio-receptor for immunoreaction with target HER3 antigen. HER3 monoclonal antibody were engineered into an scFv antibody[171] with a pair of cysteine (thiol) residues inside the loop sequence bridging the VH and VL segments, allowing it to be immobilized on the PtNPs. Figure 4.10 is a diagram of the functionalization process to obtain

PtNP-GFET biosensors to HER3. The electronic properties of Pt-decorated graphene change more significantly than that of intrinsic graphene after molecular adsorption of cysteine, which makes it promising candidate for sensor development.[172]

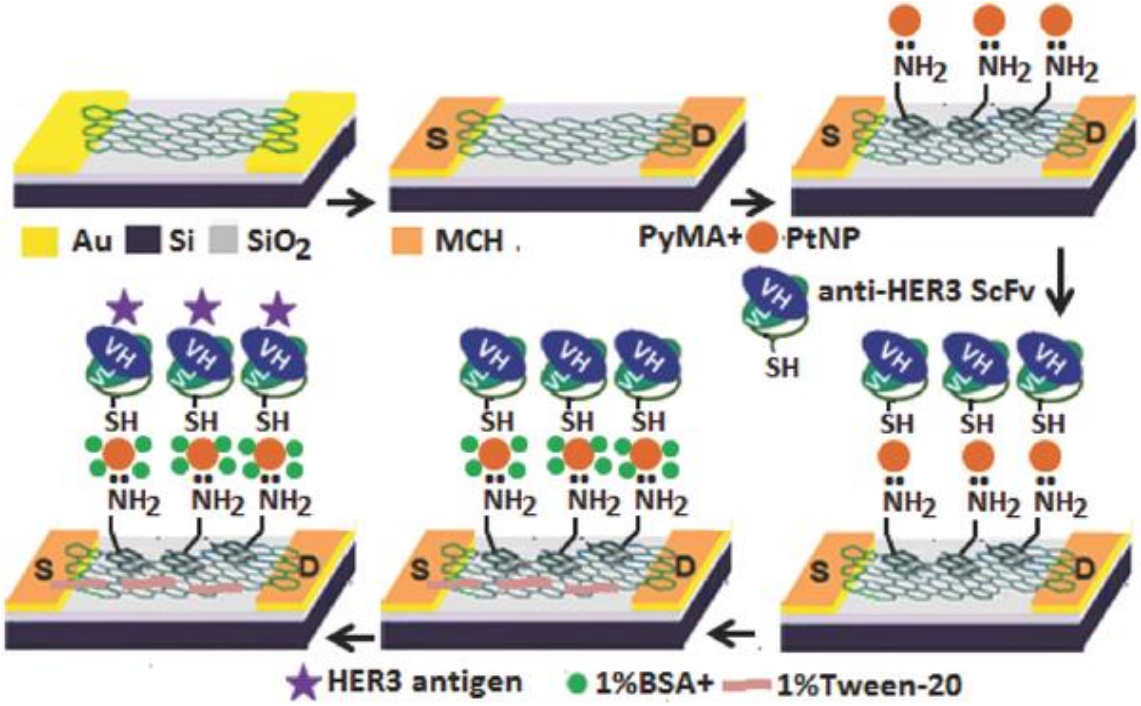

Figure 4.10: Diagram of the fabrication process for scFv-functionalized PtNP-GFET arrays. Graphene is transferred to a metalized wafer. Pyrene-NH2 is used to immobilize PtNP near the graphene surface.

AFM imaging shows the topography of CVD graphene, PtNP-graphene, and scFv immobilized on PtNP-graphene (Figure 4.11a-c). From the height profile, the thickness of the CVD-graphene sheet is 0.3–0.5 nm, consistent with monolayer graphene. After modification with PtNPs, the sample showed a height profile of 2.0 ± 0.5 nm. This together with a fine particulate feature of the hybrid structure showed that the PtNPs were well-distributed over the graphene surface. After further

modification with scFv antibodies, the device showed a height profile of 4.0 ± 0.5 nm with globular features that are significantly larger than the PtNP-graphene. The height profiles for graphene, PtNP-Gr and scFv-functionalized PtNP-Gr are shown in Figure 4.11d. the height difference of 2.0 nm is consistent with the expected height of the scFv antibody (2.5 nm), indicating the formation of scFv-PtNP conjugates bound to the GFET channel (Figure 4.11e).

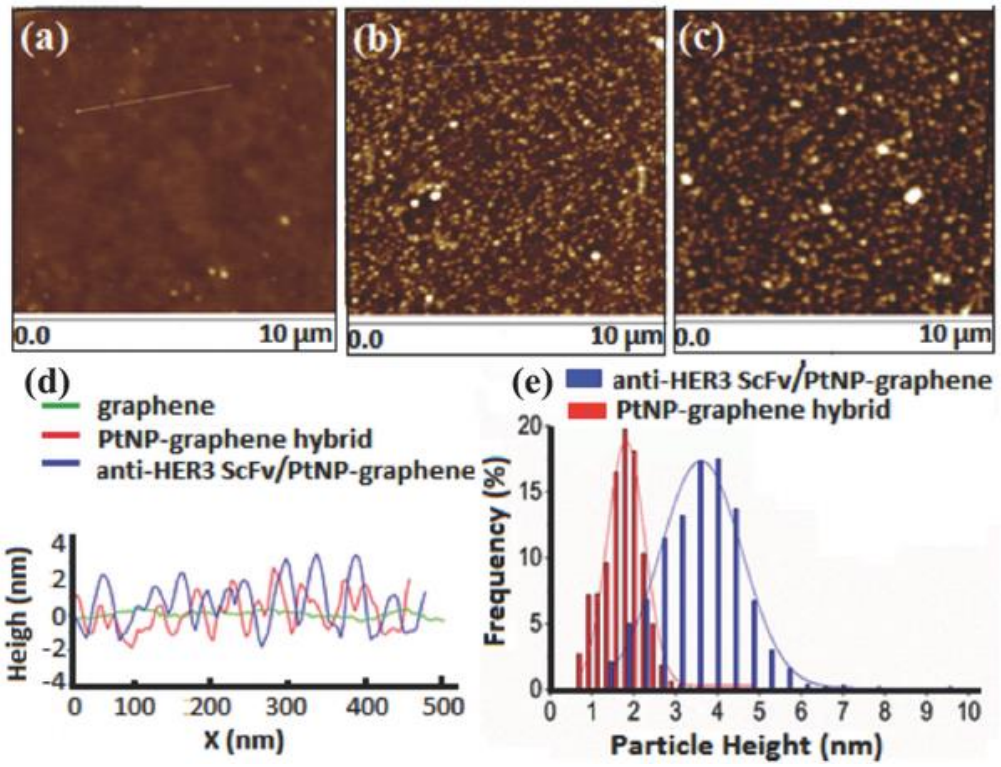

Figure 4.11: Atomic force microscopy image of a) graphene, b) PtNP-graphene hybrid, and c) scFv/PtNP-graphene, all on Si/SiO2. d) AFM line scans for each step in the fabrication (e) Particle height histograms of PtNP/GFETs, and scFv-functionalized PtNP/GFETs.

We measured the channel current as a function of gate voltage (I-Vg) at constant 50 mV bias for all devices in the 52 GFET array. Measurement was done at each fabrication step: (1) metal (Au) electrode surface passivation with 1-

mercaptohexane (MCH), (2) GFET modification with PtNPs, and (3) scFv immobilization, to confirm the formation of the bio-GFET hybrid devices (Figure 4.12). The Au source and drain electrodes were passivated with an MCH self-assembled monolayer to block nonspecific protein binding and thus avoid undesired surface contamination with scFv protein during bio-functionalization of the GFET channel. The device was rinsed thoroughly in water, and dried in a compressed air stream before taking measurements.

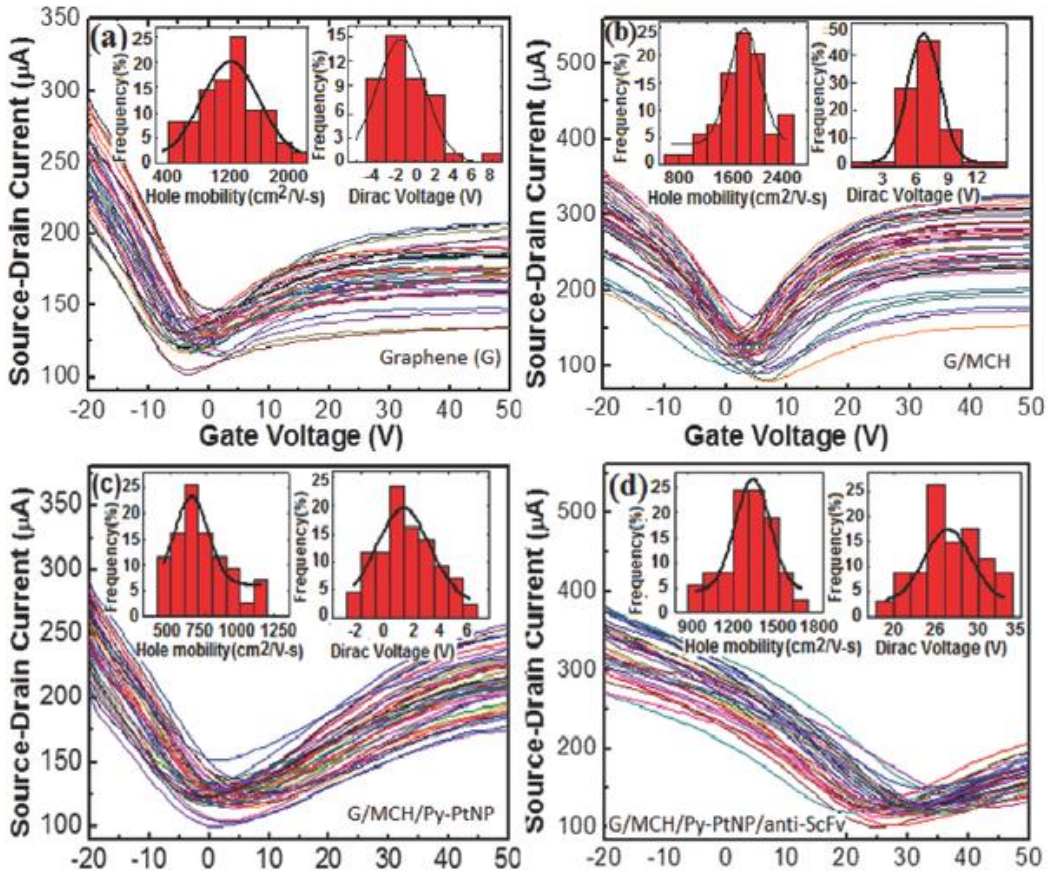

Figure 4.12: Electrical characteristics of GFET devices at different stages of surface modification, with a representative set of 52 I–Vg curves in each case. (a) As-fabricated GFET, (b) after electrode passivation with MCH, (c) PtNP/GFET hybrid, and (d) scFv-PtNP/GFET nanohybrid device. Insets show histograms of carrier mobility and Dirac voltage along with Gaussian fits (black curves).

The Dirac voltage of the GFETs was typically in the range −4.0 to +2.0 V, with an average carrier mobility of 1197 ± 56 cm^2/V-s (Figure 4.12a), which indicates a relatively clean transfer of graphene. After MCH passivation of the Au electrodes, a positive shift in the Dirac point was observed to be 6.5 ± 0.5 V with a comparatively high charge mobility 1719 ± 31 cm^2/V-s (Figure 4.12a). This may be understood in terms of a shift of the electrode Fermi level to an energy closer to the graphene valence band, which reduces the Schottky barrier at the Au–graphene interface and enhances hole injection, as reported earlier for carbon nanotube FETs. The Pyrene-NH2 binding to the PtNP on the GFET channel reduced the carrier mobility by 651 ± 21 $cm^{2/}$V-s and caused a negative shift in the Dirac voltage of 0.92 ± 0.25 V, ascribed to increased scattering by the basic Pyrene-NH2.[142, 173] Following antibody attachment the carrier mobility increased to 1330 ± 14 cm^2/V-s with a positive shift in the Dirac voltage of 26.4 ± 1.0 V, suggesting a decrease in carrier scattering by scFv attachment.

Figure 4.13 shows the I–Vg characteristics of an individual GFET device functionalized as described above and then treated with a blocking reagent (0.1% Tween 20 + 0.1% bovine serum albumin), which served as a barrier to nonspecific protein adsorption on the metal nanoparticles and GFET channel,[112] followed by immunoreaction upon exposure to the HER3 antigen in buffer (pH 7.3) at concentrations in the range 300 fg/mL to 300 ng/mL. For each measurement, the GFET was incubated in a solution with a given HER3 concentration for 1 h, gently

dried with compressed air, and electrically characterized. The Dirac voltage of the Bio-GFET showed a successive positive shift with increasing HER3 concentration. Figure 4.13a shows the shifts in Dirac voltage for an individual GFET at each successive stage of chemical modification/bio-functionalization with a positive shift of 7.0 V upon exposure to 300 ng/mL of HER3. Figure 4.13b shows the response of an individual device to 30 ng/mL of HER3, insets show the response to 300 fg/mL of HER3 (positive shift of 1.7 V) and pure buffer as a negative control (shift less than 1.0 V).

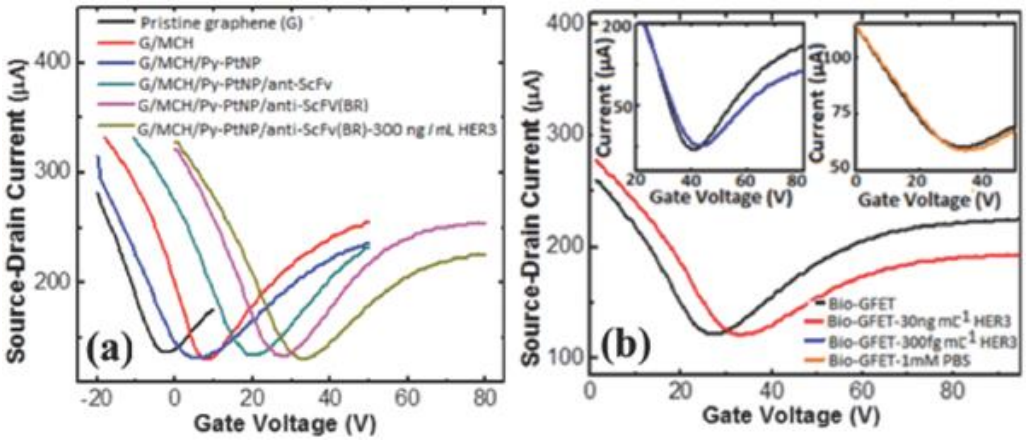

Figure 4.13: (a) Current–gate voltage (I–Vg) characteristics of a representative GFET device after fabrication and after each successive surface modification leading to formation of anti-HER3 scFv functionalized PtNP/GFET and on exposure to 300 ng/mL HER3 in PBS. (b) The sensing performance of the device against 30 ng/mL HER3; Insets: (upper left) shows sensor response to 300 fg/mL HER3, and (upper right) sensor response to PBS (without antigen).

A significant positive shift in Dirac voltage was observed upon exposure to HER3 antigen, which is readily distinguishable from the very small response observed for a pure buffer sample. The observed Dirac voltage shifts may be attributed to electrostatic chemical gating of the GFET associated with increasing binding of antigen to scFv receptors bound on the graphene surface.

There was a systematic dependence of the VD shift with varying antigen HER3 concentration. Each concentration tested independently on 6–10 functionalized devices for signal averaging and to avoid sample contamination across trials. The variation of the average measured shift in the Dirac voltage as a function of HER3 concentration is displayed in Figure 4.14, where the error bars reflect the standard error of the mean. The sensor responses agree with a model based on the Hill–Langmuir equation describing the equilibrium binding of a ligand by a receptor, as described in section 2.2.3.

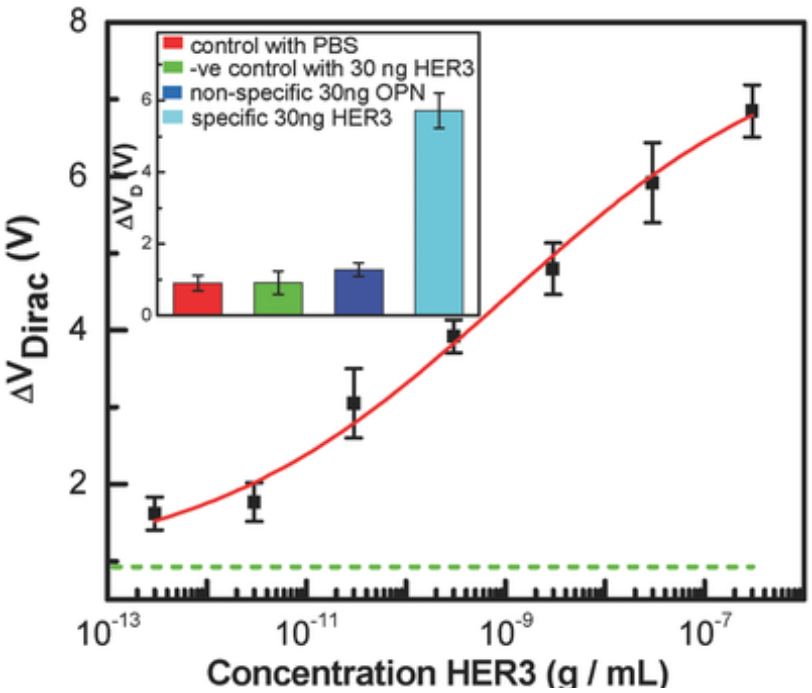

Figure 4.14: Response of the PtNP biosensor showing Dirac voltage shift (ΔV) response as a function of HER3 concentration (300 fg/mL to 300 ng/mL). The data is fitted to a Hill-Langmuir model (red curve); Inset: Comparison of device responses for various control experiments. Fully prepared biosensor to target HER3 at 30 ng/mL (light blue bar). Fully prepared biosensor to negative controls plain PBS buffer (red bar) and non-complementary protein marker osteopontin (OPN; dark blue bar). Also shown is the response in a negative control experiment where a device prepared without the scFv antibody was exposed to the target HER3 at 30 ng/mL (green bar).

$$\Delta V_D^{rel} = A\frac{\frac{c}{K_a}}{1+\frac{c}{K_a}} + Z \tag{4.3}$$

here c is the HER3 antigen concentration, A is the sensor response at saturation when all binding sites are occupied, Z is an offset to account for the response to pure buffer, K_a is the dissociation constant describing the concentration at which half of available binding sites are occupied, and n is the Hill coefficient describing cooperativity of binding. The best-fit parameters were K_a = 790 ± 160 pg/mL. The low value of K_a indicates strong binding affinity of the scFv for HER3 antigen at the electrode surface, which may reflect high antibody loading of the PtNPs. The value of the offset parameter Z = 0.90 is in good agreement with measured responses of devices to pure buffer (0.89 ± 0.2 V; indicated by the dashed line in Figure 4.14). The results indicate that a collection of 6–10 bio-GFET devices can readily differentiate between pure buffer (0.89 ± 0.2 V) and a solution containing 300 fg/mL HER3.

Multiple control experiments were conducted to gauge the specificity of the device (inset to Figure 4.14). First, A fully functionalized bio-GFET device was tested against 30 ng/mL of OPN, the resulting response (0.91 ± 0.2 V) was indistinguishable from the device response to pure buffer. And second, the response of an unfunctionalized GFET device to 30 ng/mL of HER3 (1.19 ± 0.2 V) was again comparable to the buffer response, which is significantly smaller than the response

of a functionalized bio-GFET to the same HER3 concentration (5.71 ± 0.49 V) suggesting that bio-GFET response to HER3 target reflects specific ligand–receptor binding with a negligible contribution from nonspecific binding. Although a precise quantitative understanding of the transduction mechanism remains to be developed, our results motivate the possibility that the present method could be further optimized to develop a new class of scalable graphene-based nanohybrid biosensors with the highly sensitive and specific chemical recognition characteristic of the protein for a useful diagnostic test.

4.3.4 Conclusion

We demonstrated a novel scalable fabrication process for biosensor arrays based on PtNP-Gr devices functionalized with an scFv with specific affinity for the breast cancer biomarker protein HER3. The device exhibited a concentration-dependent response over a wide concentration range of HER3 that was in excellent quantitative agreement with a model based on the Hill-Langmuir equation of equilibrium thermodynamics. Control experiments indicated that the HER3 specific scFv antibody retains its highly specific binding characteristics on the PtNP-Gr hybrid structure, signifying the suitability of PtNPs for efficient biomolecular immobilization for enhanced loading of antibodies on graphene transistors. These observations of a good analytic range, high antigen–antibody specificity, rapid response, and ease of use with a small sample volume makes this device superior to traditional immunoassay, suggesting its use as a point-of-care diagnostic tool.

4.3.5 Experimental Section

Graphene synthesis: Done in a Low Pressure Chemical Vapor Deposition furnace. Cu foil was cleaned with acetone and isopropyl alcohol (IPA), and then dried by N2 gas. The reaction chamber was pumped to a base pressure of ~50 mTorr and 80 sccm hydrogen (H_2) flow into the chamber. The furnace was heated to the process temperature of 1020 °C, followed by annealing of the Cu foil for 30 min. Growth is done under methane (CH_4) introduced at a flow rate of 50 sccm for 35 min for graphene growth. The reactor was subsequently rapidly cooled to room temperature under a flow of 80 sccm H2 and 50 sccm CH4.

Device fabrication: A source and drain electrode array was patterned on an SiO2/Si water using a standard photolithographic process, based on a bilayer resist process of PMGI and Shipley 1813. Thermal evaporation was used to deposit 5 nm Cr and 40 nm Au, followed by lift-off with 1165 striper. CVD Graphene was transferred onto the Si/SiO_2 chip with metal electrodes by the PMMA-assisted "bubbling" transfer method.[92] After graphene transfer, GFET channels were patterned using bilayer photolithography similar to the metallization, followed by oxygen plasma etching (1.25 Torr, 80 W, 30 sec). Stripper 1165 removes residual photoresist.

Biosensor fabrication: GFETs were incubated in a colloidal mixture of 100 ppm PtNPs (Sigma) in 5mM 1-methyl pyrene amine in methanol for 2 h, followed

by extensive washing with methanol and IPA, and dried under flowing N2 to yield the PtNP/GFET hybrid structure.

Expression and purification of Anti-HER3 scFv: The complete amino acid sequence of the variable heavy and light chains of the anti-HER3 A5 antibody was described previously.[171] An scFv version of the A5 antibody was expressed and purified as previously described.[174] Briefly, the pSYN-A5 scFv expression vector, which encodes for a 6x-HIS tagged version of the scFv, was transformed into TG1 E. coli and protein expression was induced through addition of 1 mM IPTG (Isopropyl β-d-1-thiogalactopyranoside, Fisher Biotech) to a logarithmically culture. After 4 h of induction at 25 °C fully folded scFvs were extracted from the periplasmic space by osmotic shock in 30 mM Tris-HCl (pH 8), mM EDTA, 20% sucrose (w/v). Protein was dialyzed into phosphate buffered saline and purified by sequential immobilized metal affinity chromatography (IMAC) and size exclusion chromatography.

Functionalization: A solution of scFv antibodies (3.2 μg/mL; pH 7.3) was pipetted onto the PtNP-GFET array in a humid environment (to keep the solution from evaporating), over an incubation period of 1 h. This causes PtNPs to be functionalized with scFv through binding of thiol groups of cysteine residues. After incubation, the chips were cleaned sequentially in two DI water baths under agitation for a total of 2 min, and then blown dry in a gentle stream of nitrogen.

4.4 SUMMARY

In this chapter, we explored two different nanoparticle-mediated functionalization methods. We applied each one to a different biomolecule through a thiol-nanoparticle bond, and as such the biomolecules are interchangeable with the nanoparticles. First, we developed a monodisperse layer of gold nanoparticles on a graphene channel field effect transistor (AuNP-GFET) by evaporating a gold layer onto CVD grown graphene and annealing after fabrication. Evaporating a gold forms clusters on top of the graphene and thermal annealing forms the nanoparticles from these clusters. These nanoparticles are bound to thiolated DNA to realize a complimentary DNA sensor of high specificity and sensitivity. Second, platinum nanoparticles were immobilized to a graphene channel field effect transistor (PtNP-GFET) by means of a 1-methyl pyrene amine linker (Pyrene-NH2). A thiolated scFv fragment from a HER3 antibody is bound to the PtNP to form a HER3 antibody sensor. The antibody sensor retains the specificity of the antibody biomolecule and the sensitivity of the graphene transducer.

5 ANTIBODY/ANTIGEN BIOSENSORS

This chapter outlines Nano/bio hybrid sensors that are functionalized with their biomolecules by chemical linkage. First, we motivate this research and introduce previous applications. We mention the limitations and outline the general advantages, and the flexibility of the approach used here. The flexibility of the chemical linkers presented here comes from one of their functional group that binds to an amine group. Amines are very prevalent in proteins, making both approaches presented here applicable to most natural and engineered proteins.

First, we present a comparison between two chemical linking methods, covalent and noncovalent interaction to the graphene. Both linkers bind through a succinimde ester reaction, and the same antibody is used to properly compare the sensing response of both linkers. The linker 1-pyrenebutanoic acid succinimidyl ester (Pyrene-NHS) non-covalently binds to graphene through π-π stacking, while the linker 4-Azido-2,3,5,6-tetrafluorobenzoic acid, succinimidyl ester (Azide-NHS). Finally, we developed the framework for a multiplexed measurement for simultaneous detection of a complex mixture of targets. The device array layout allows to functionalize groups of GFETs with different antibodies. We measure the response of each group to each individual target, and to the target mixture.

5.1 INTRODUCTION

In the context of biosensors, the aim is to detect target molecules in effective concentrations and in various matrices (*e.g.* biofluids and environmental). Biochemical receptor molecules of interest, especially for medical applications, are antibodies due to their high specificity and selectivity to their target antigen.[27, 175] It is crucial that the receptor molecule is bound to the transducer surface with high density without affecting its activity. Pyrene based compounds has been used to noncovalently functionalize reduced graphene oxide (rGO),[176] CVD graphene,[177] and nanotubes.[178] Pyrene is a versatile, noninvasive strategy that will maintain the mobility of the transducer. On the other hand, Perfluorophenylazide (PFPA) has been used to covalent immobilize functional groups onto carbon surfaces and nanoparticles upon thermal activation or light irradiation of the azide functionality.[102, 179-181] The PFPA conjugation method is simple, fast, reproducible, and has been proven to be efficient to immobilize synthetic polymers,[179] graphene,[180] and carbohydrates[181] onto variety of substrates.

Simultaneous detection of multiple biomarkers is a useful method to reduce both false positive and false negative diagnoses for biomedical applications where target biomarkers are present in complex bodily fluids. Arrays of Nano-enabled biochemical sensors suitable for multiplexed detection are a potential solution to this problem, where different areas of the sensing array can be dedicated to detect different targets of interest. Multiplexed detection using transduction devices such as nanowires,[182] and MEMS (nanorods)[183] have been reported. Graphene sensor arrays have not been widely implemented for multiplexed detection.

5.2 COVALENT/NONCOVALENT FUNCTIONALIZATION OF GFET ARRAYS FOR BREAST CANCER BIOMARKER DETECTION

5.2.1 Abstract

We have developed a Graphene Field Effect Transistor (GFET) array that consists of a single-variable chain fragment (scFv) bounded to the device channel and the electrical readout is used to read out the binding response between the scFv and its corresponding antigen. The extracellular domain human epidermal growth factor receptor protein (Her3-ECD) is used as target. The GFET fabrication process involves an industry standard compatible photolithographic process with soft plasma etcher conditions and specific solvent exposure time to avoid graphene degradation, as confirmed Raman spectroscopy. One GFET array consist of one hundred devices (10 μm x 100 μm) with an average Dirac voltage of -3.4 ± 0.3 V, mobility of 2363 ± 87 cm2/Vs and 95% yield. Two binding chemistries are compared: a photoactivated covalent binding based on a perfluorophenyl azide (Azide-NHS), and a noncovalent binding based on pyrene compounds (pyrene-NHS). Binding chemistries are used to attach the scFv to the graphene channel confirmed by Atomic Force Microscopy (AFM). Electronic transport measurements indicated the recognition of the binding between Her3-ECD and scFv, a concentration-dependent response in the Dirac Voltage was observed, with a detection limit of 3.1 pg/mL, a factor of 100x more sensitive than ELISA. The arrays exhibited excellent selectivity for Her3-ECD over other proteins as Upar.

5.2.2 Introduction

Proper chemical tools to attach different biomolecules to the graphene surface are of great importance for any biochemical application. Graphene is a one layer continues sheet of sp^2 hybridized carbon atoms arranged in a honey-comb lattice.[184, 185] All carbon atoms are exposed to the environment and its high carrier mobility make graphene extremely sensitive to small electrostatic changes in its surroundings. These properties combined with its ease of fabrication, and well understood chemistry provide a unique platform for sensor applications.[186, 187] Graphene Field Effect Transistors (GFET) can act as a transducer and be used to measure these electrostatic changes.[186, 187] GFET devices with a single back gate have been investigated by several groups for the detection of gases,[188] organic compounds,[189] and biomolecules.[189, 190] Immunoglobulins (Ig) are glycoprotein molecules that have high binding affinity for a specific antigen related to a disease.[191] Sometimes referred to as antibodies they serve as a recognizing agent for the immune system. The heavy chain and light chain (different amino acid chains) form the backbone of the structure known as the constant region (Fc). The single-chain variable fragment (scFv) is the active region of the antibody that bind to the biomarker.[191] scFv chains are shorter than their Ig counterparts and when used in GFET sensors the electrostatic interaction for the biomarker is closer to the graphene surface, this enhances sensitivity.

Here, we combine the exceptional properties of GFET arrays and the selectivity of immunoglobulins with two conjugation strategies to develop a powerful diagnostic tool. The GFET array fabrication method outlined here is high performance, scalable, and reproducible. The two bifunctional linkers used here (fig) are the commonly used [1-pyrenebutiric acid N-hydroxysuccinimide] (pyrene-

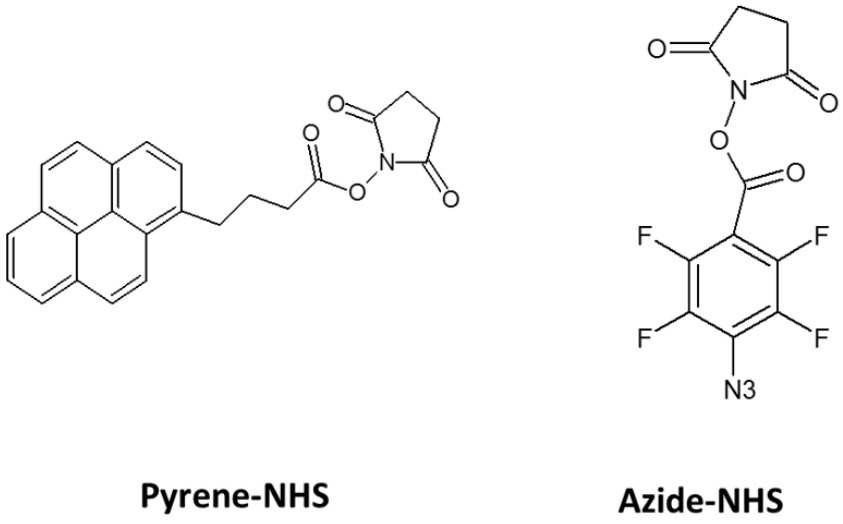

Figure 5.1: Chemical structure of pyrene-NHS (left) and azide-NHS (right). Both have an [N-hydroxysuccinimide, ester] group, active for amine reactions.

NHS) where the pyrene functional group stacks with graphene unchanging the device electronic properties, and [4-Azido-2,3,5,6-tetrafluorobenzoic acid, succinimidyl ester] (azide-NHS) a photoactivated molecule where the azide functional group forms two covalent bonds with graphene. Here we present a comparison between the two linker chemistries and present their advantages and drawbacks.

5.2.3 Methods

Graphene growth by chemical vapor deposition (CVD): Graphene synthesis was carried out by low-pressure chemical vapor deposition (OTF-1200X-4-C4-SL-UL, MTI Corp.). Cu foils (Alfa Aesar Item #46365) were cleaned with Acetone for 10 minutes and IPA rinse, and then blown dry with N_2 gas. The reaction chamber was pumped to a base pressure of 50 mTorr. The Cu growth substrate was annealed at 1020 °C for 30 minutes with a gas flow of 80 sccm H_2. Monolayer graphene was then grown using methane as a carbon source at a flow rate of 10 sccm for 20 mins. The reactor was subsequently cooled to room temperature rapidly under a flow of 80 sccm H_2 and 10 sccm CH_4. Once the furnace cooled to 80 °C, the graphene/Cu foil (Gr/Cu) was removed from the furnace and stored.

Array Fabrication. A two-step photolithography process is used to fabricate devices. First to define and deposit the gold contacts, second to define the channel after the graphene is transferred onto the metallized wafers. To define the contacts, we use Si/SiO_2 wafers with 250 nm oxide (Virginia Semiconductor) we use a bilayer photolithography process with PMGI followed by a Shipley 1813. Samples are exposed to a photolithography mask in hard contact with dose of 80 mJ/cm^2 and are developed in Shipley Microposit MF-319. A Lesker PVD75 evaporator is used to deposit a 5 nm layer of Cr and a 40 nm layer of 99.999% Au, an overnight soak of Stripper 1165 is used to lift-off the metal contacts after evaporation.

To transfer the graphene a layer of poly-methyl methacrylate (PMMA-A4) is spin coated to the Gr/Cu, as mechanical support. The Gr/PMMA is then transferred from the Cu foil by the "bubble" method through several baths of deionized water and finally transferred to the final substrate, the metallized wafer.

To define the graphene channels a bilayer lift off process is used, as before. PMGI followed by a Shipley 1813. Samples are exposed to a photolithography mask in soft contact with dose of 80 mJ/cm^2 and developed in Shipley Microposit MF-319. A Reactive Ion Etching (RIE) Plasma system is then used to anisotropically etch the graphene. The lift-off process consists of Acetone, Remover 1165, and Acetone 5 min soaks. The sample is rinsed with IPA and dried with N_2. Devices were annealed in 1000 sccm Argon and 250 sccm H2 for 1 h at 225 °C. The arrays yield ranged from 95% to 99%.

Graphene-FET Functionalization. The GFET arrays were exposed to a linker solution. A 10 mg of pyrene-NHS (Sigma-Aldrich) solution in 25 mL of methanol for 1 h, followed with 2 min in methanol and 2 min in IPA to remove the unattached pyrene molecules.[132] Droplets of 10 µg/mL scFv (HER3 scFv-A5) solution in PBS buffer (provided by Mathew Robinson, Fox Chase Cancer Center[192]) are placed to the GFET arrays for 1 h under high humidity conditions. Arrays were then cleaned with 3 baths of Deionized Water (DI-W) for 2 min each. To block the free NHS groups on the linker, we exposed the arrays to 300 uL of ethanolamine in 20 mL of 2 mM PBS (pH 8.5) for 30 min. The arrays were cleaned

with 3 baths of DI-W for 2 min each. Finally, the arrays were exposed to HER3 (HER3-ECD) antigen solution in a concentration range from ug/ml to pg/ml for 1 h under high humidity conditions with similar cleaning process than the scFv step.

In the second approach, a 2 mg azide-NHS (TCI America) solution in 20 mL of N,N-dimethylformamide (DMF) is used as linker (azide is light sensitive, and needs to be prepared under dark conditions). GFET arrays are placed in the linker solution and exposed to 3.5 J/cm^2 UV-light (365 nm: 29 mW/cm^2 for 2 min). Arrays were cleaned with DMF, Acetone and IPA baths for 2 min each. scFv, blocker and target attachment steps were done as before.

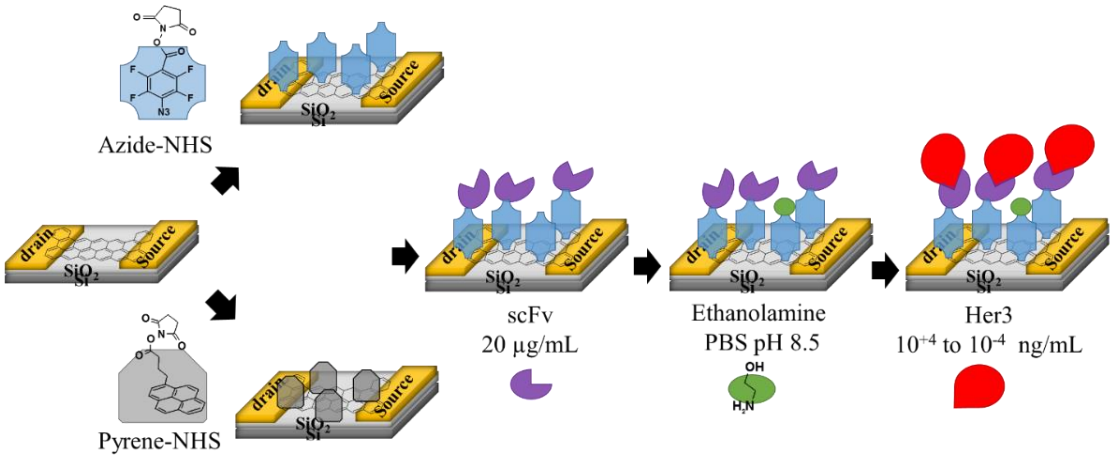

Figure 5.2: Functionalization strategies for creating Her3-ECD binding sensor. First, the graphene is functionalized with Azide-NHS or Pyrene-NHS. The NHS active groups recognize the primary amine of scFv-A5 receptor protein to form an amide bond. The unmodified NHS groups are blocked with ethanolamine and then the devices are exposed to a Her3-ECD solution.

5.2.4 Results and Discussion

We describe the development of wafer-scale GFET arrays (100 devices) with yield higher than 95%. Graphene samples are exposed to the PMMA supporting

layer, PMGI/Shipley 1813 resists, and a mild plasma etch; it is important to guarantee that the surface is residue free once the process is complete. AFM images of the GFET device in Figure 5.3A shows a clean graphene with low number of polymer residues and wrinkles. The Raman spectra in Figure 5.3B shows I_{2D}/I_G = 1.4 and small I_D/I_G = 0.2. In Figure 5.3: Performance characteristics of annealed Graphene-FET array: (A) AFM image 4x4 µm, z=10 nm; (B) Raman Spectra; (C-E) I-V response of 100 G-FET devices, 0.1 V and histograms of Dirac voltage and hole mobility. C-E, the I-V response for the G-FET shows ambipolar behavior with an average Dirac voltage of -3.4 $\pm$ 0.3 V and average mobility of 2363 $\pm$ 87 cm^2/Vs. The low intensity D peak, clean AFM and the excellent electronic parameters of our G-FETs confirms a high quality monolayer graphene with low contamination.

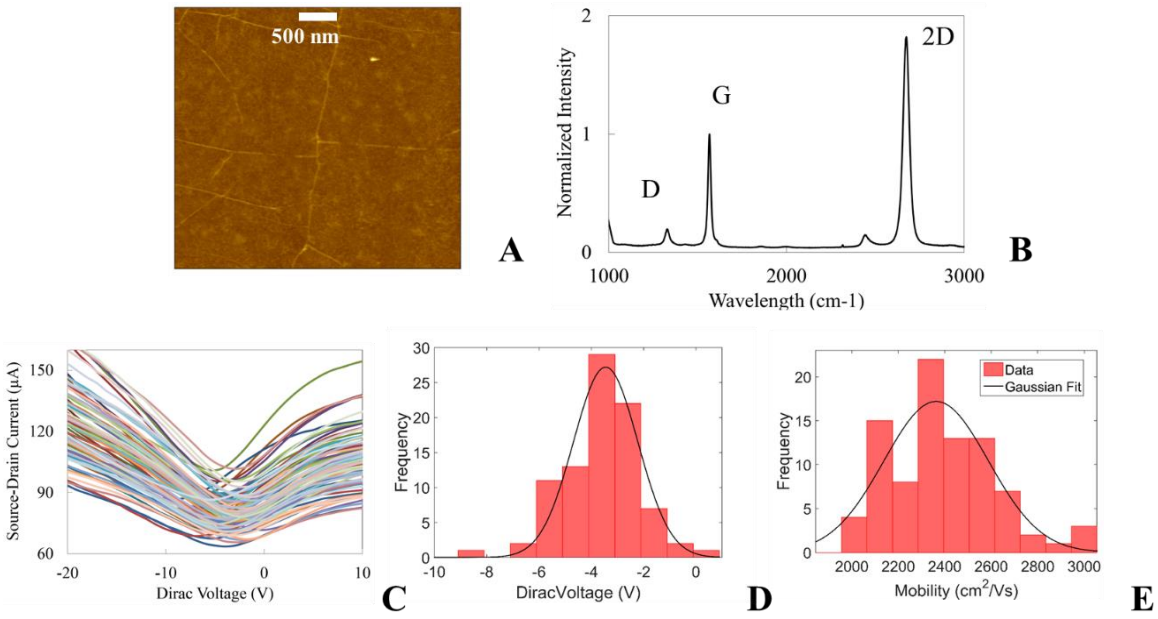

Figure 5.3: Performance characteristics of annealed Graphene-FET array: (A) AFM image 4x4 µm, z=10 nm; (B) Raman Spectra; (C-E) I-V response of 100 G-FET devices, 0.1 V and histograms of Dirac voltage and hole mobility.

Previously we reported a diazonium salts based chemistry to attach antibodies to graphene FETs, the diazonium linker forms a covalent bond with one carbon atom of the graphene.[120, 193] This new bond changes the C-C hybridization form sp^2 to sp^3 affecting the crystal structure and lowering carrier mobility.[102, 120] Now, we explore the azide-NHS chemistry that form a three-membered aziridine-ring linkage with two neighborhood carbons, generated by photochemical activation of organic azides.[179, 181] The divalent functionalization changes the C-C hybridization form sp^2 to sp^{2+g} and the Fluor atoms suppress the ring expansion reactions of the singlet phenyl-nitrene increasing the addition yield.[102, 180] Also, we explore the noncovalent bond between pyrene-NHS and graphene, this doesn't affect the sp^2 environment as well the electronic properties of graphene.

Figure 5.4 compares AFM scans for scFv-A5 proteins attached to graphene by the pyrene-NHS (Figure 5.4A) and azide-NHS (Figure 5.4C). The protein density increases a factor of four when the azide-NHS was used (131 proteins/um^2) compared to the pyrene-NHS (32 proteins/um^2). The higher protein density attached on graphene confirmed PFPA high reactivity and fast kinetics.[105] The histogram for pyrene-NHS (Figure 5.4B) had its average height at ~2.5 nm, for the azide-NHS (Figure 5.4D) the average height of the features increases to ~5.5 nm and a large number of features larger than 8 nm. We attribute the lower height for Pyrene-NHS absorbs on graphene with low contribution on the protein height ~3 nm.[102]

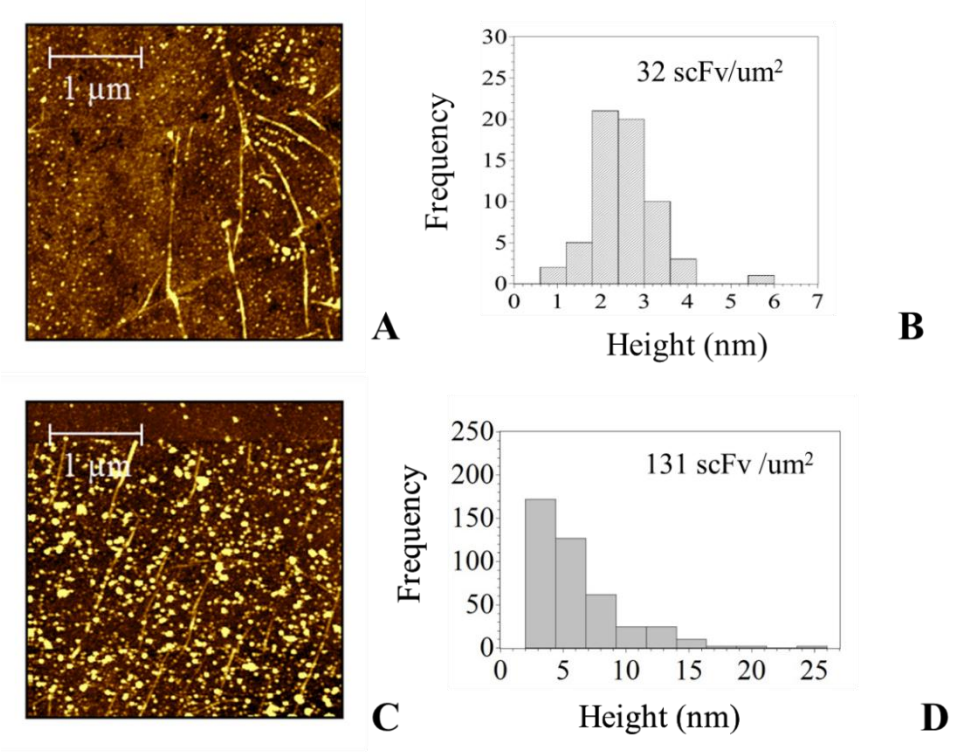

Figure 5.4: Atomic Force Microscopy (AFM) images and height histograms of scFv-A5 receptor proteins (gold dots) decorating the G-FET surface with: (A-B) Pyrene-NHS and (C-D) Azide-NHS, 3.3 x 3.3µm, z = 5 nm. There is a factor of 4 difference in the protein attachment density between the Azide-NHS and the Pyrene-NHS. The height histograms of AFM features show a peak around 2.5 nm and 5.5 nm for Pyrene-NHS and Azide-NHS, respectively.

Raman spectroscopy was done to characterize the GFET channel for the azide functionalization process. Figure 5.5 shows the spectra before and after incubation in Azide-NHS, after the UV-light exposition the D peak slightly increases. This minimum D peak change suggests that the graphene sp^2 structures are not significantly perturbed after a weak C-C bond forms between the two bridgehead atoms. After the scFv-A5 attachment with Azide-NHS the D peak increases confirming the protein modification on graphene. The significant increase in I_D/I_G ratio is consistent with the breaking of graphene carbon-carbon bonds during the chemical and proteins functionalization.[120, 132]

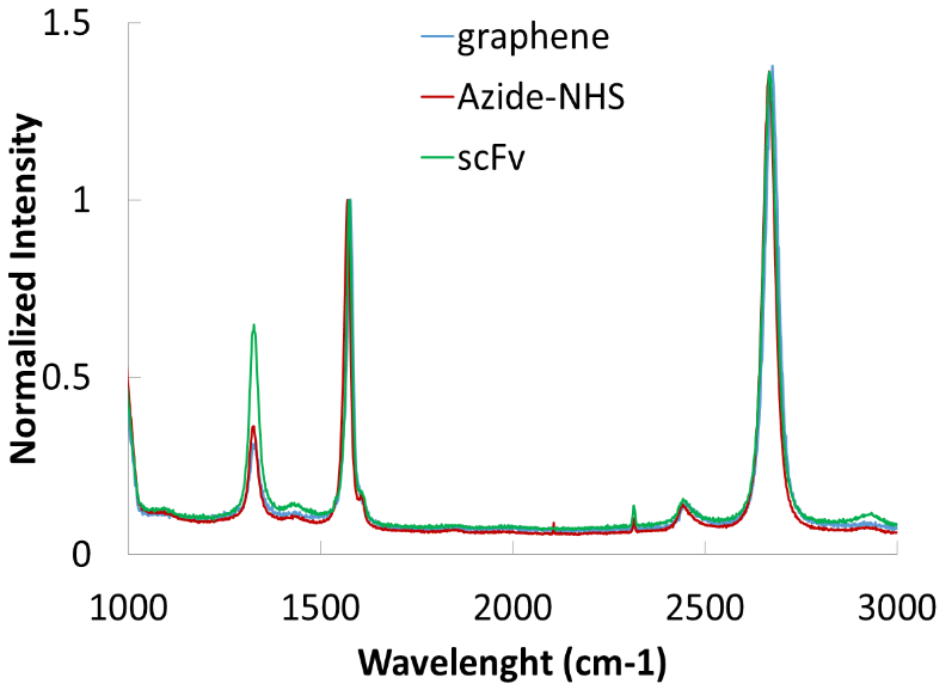

Figure 5.5: Raman spectra of GFET before (blue) and after (red) exposure to Azide-NHS and after scFv-A5 (green). The strongly enhanced D-band near 1360 cm^{-1} after the functionalization indicates formation of numerous binding sites on the graphene surface.

GFET electrical characterization is done by measuring the source-drain current as a function of back gate voltage (I-Vg). Mobility slightly decreases, the absorption of pyrene-NHS doesn't affect the carrier scattering.[132] After the Pyrene-NHS treatment (Figure 5.6A), the Dirac voltage increases consistent with the presence of carbonyls groups near the graphene.[132] The I-Vg curve of the photoactivated azide-NHS (Figure 5.6B) shows a slight increase of electron-hole mobility. Similar behavior was reported for graphene immobilized on a PFPA-functionalized wafer where the carrier mobility increases a factor of two.[105, 194, 195] It has also been reported that graphene capped with fluoropolymers as CYTOP and Teflon-AF show an increase of mobilities, caused by the strongly polar nature of the C-F bonds in the polymer.[196, 197]

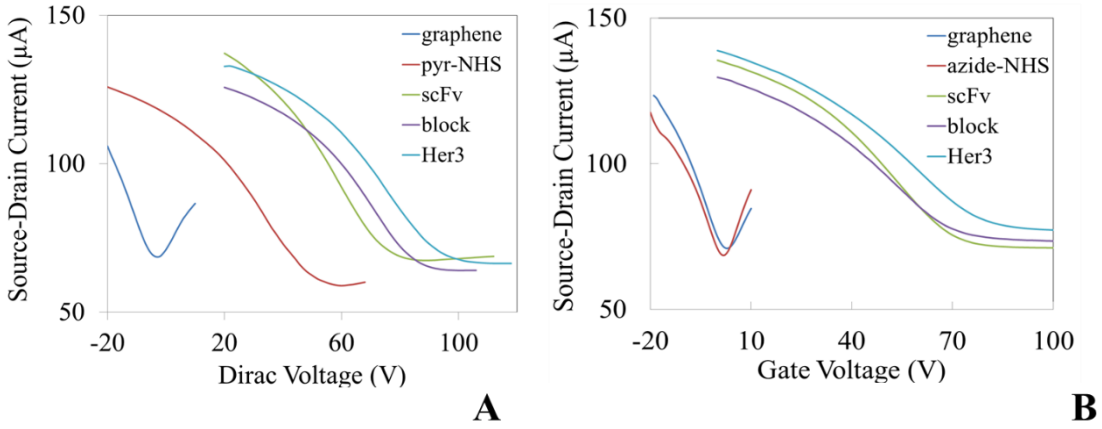

Figure 5.6: I-V_g curves in forward gate sweep after successive functionalization steps of GFET modified with: (A) Pyrene-NHS and (B) Azide-NHS. Note the Dirac voltage shift to positive values after exposure to a solution of scFv-A5, blocking step and Her3-ECD.

Graphene curves are modelled using a linear approximation for the Schottkey contact resistance, as in section 2.1.6. Dirac voltage is extracted from the response curves, for all GFETs, at each step of the functionalization and sensing. The mechanism for this sensing response can be explained by local electrostatic gating caused by a conformational change in the scFv-A5 receptor protein upon binding its Her3-ECD target.[198] For each device in the array, the Dirac voltage shift is calculated as the difference between the extracted voltages. The average response as a function of the concentration is fitted to a Hill-Langmuir curve that describes equilibrium binding of a ligand by a receptor (equation (5.1).[199]

$$\Delta V = V_{max} \frac{\left(\frac{c}{K_a}\right)^n}{1 + \left(\frac{c}{K_a}\right)^n} + V_{buff} \qquad (5.1)$$

c is the HER3 antigen concentration, V_{max} is the sensor response at saturation when all binding sites are occupied, Z is an offset to account for the response to pure buffer, K_a is the dissociation constant describing the concentration at which half of available binding sites are occupied, and n is the Hill coefficient describing cooperativity of binding. The best-fit parameters were K_a = 1.7 $\pm$ 0.9 ng/mL and $n = 0.5 \pm 0.3$ for pyrene-NHS (Figure 5.7A) and K_a = 0.1 $\pm$ 0.03 ng/mL and $n = 0.3 \pm 0.2$ for azide-NHS (Figure 5.7B).

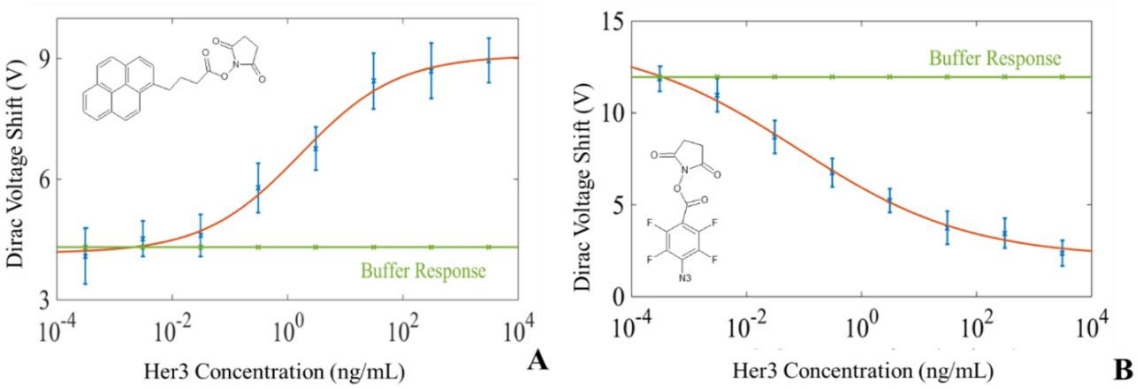

Figure 5.7: Sensor response (Dirac voltage shift) as a function of HER3-ECD concentration. Each point consists of 25 statistically significant devices for (A) Pyrene-NHS and (B) Azide-NHS.

The reported value of dissociation constant for the scFv-HER3 response is 11 nM,[132, 192] same order of magnitude as our value 70 nM. The response of 2 mM PBS plus one standard error represents the limit of detection of the GFET array and is represented in each curve (green line). Azide-NHS enhances the sensor sensitivity two times in comparison with pyrene-NHS linker, we attribute this to the C-F bonds that form a strong dipole net at the interface with graphene, enhancing any small electrostatic perturbation as the target-receptor interaction occurs. A control

experiment was performed using 3.1 ng/mL UPAR target, on pyrene-NHS GFET the average of Dirac voltage shift is 5.7 $\pm$ 0.5 V and for 2 mM PBS buffer is 5.8 $\pm$ 0.7 V. For reference, HER3-ECD target response at that concentration is 9.4 $\pm$ 0.9 V. For azide-NHS functionalized GFET the same control experiment yields a Dirac voltage shift of 13.8 $\pm$ 0.7 V, while the 2 mM PBS 14.8 $\pm$ 0.7 V, and HER3 11 $\pm$ 1 V. We conclude that the measured response for HER3-ECD was highly specific for both pyrene-NHS and azide-NHS linkers, however azide-NHS shows an enhancement in the measured sensor response.

5.2.5 Conclusion

We have showed that GFETs photochemically coupled with genetically engineered scFv of anti-HER3 have high sensitivity towards different HER3 concentrations with detection limits of lower pg/mL. Our GFET fabrication is simple, high yield, scalable, and compatible with current industry standards. The average Dirac voltage of a GFET array was -3.4 + 0.3 V, with mobility of 2363 + 87 cm^2/Vs with > 95% yield. The photoactivated linker azide-NHS has dipolar C-F bonds that improves mobility, electron-hole transport, enhance the protein receptor density and target recognition signal with respect to the more commonly used pyrene-NHS linker. Electronic transport measurements indicated the recognition of the binding between HER3-ECD and scFv-A5, with a detection limit of 3.1 pg/mL, a factor of 100 times more sensitive than ELISA. These devices exhibited excellent selectivity for HER3-ECD over other proteins as UPAR. GFET-based detection offers significantly lower, quantifiable detection limits as well as fast, all-electronic readout that can be performed by any technician in a point-of-care diagnostic setting.

5.3 SENSOR FABRICATION FOR MULTIPLEXED DETECTION OF LYME DISEASE BIOMARKER PROTEINS

5.3.1 Abstract

We have developed a scalable fabrication process of multiplexed sensing array for Lyme disease detection based on Graphene Field Effect Transistors (GFETs). Graphene, grown by Chemical Vapor Deposition is "bubble" transferred to a pre-patterned gold contact array wafer. Photolithography is used to define graphene channels, and thermal annealing is used to remove impurities. Devices show high mobilities (4800 ± 200 cm^2/V-s) and low charge doping (Dirac voltage of 0.5 ± 0.2 V), and high transistor yield (98%). Sensors are then functionalized with an engineered Lyme antibody protein by a photoactivated perfluorophenyl azide linker chemistry. Four different antibodies specific to two different targets (two antibodies for each target) were measured and show a concentration dependent response. A mixture of the targets is then measured where the antibodies are multiplexed at different regions of the sensor array, showing a distinct detection between the two components of the mixture.

5.3.2 Introduction

Simultaneous detection of multiple biomarkers is a useful method to reduce both false positive and false negative diagnoses for biomedical applications where target biomarkers are present in complex bodily fluids. Arrays of Nano-enabled biochemical sensors suitable for multiplexed detection are a potential solution to

this problem, where different areas of the sensing array can be dedicated to detect different targets of interest. Lyme disease is the most common tick transmitted disease in North America and Europe.[200, 201] The infection of *Borrelia burgdorferi*, commonly called Lyme disease, is transmitted through the bite of a black legged tick and clinical findings alone are often not sufficient for a diagnosis. Diagnosis of Lyme disease is currently done indirectly by measuring the antibody response to the presence of the bacterial infection, using either Enzyme-Linked Immunosorbent Assay (ELISA) or Western Blot. There is growing interest in development of approaches for improved early diagnosis of Lyme disease, with most research focused on improving the current diagnostic techniques. A 2-tiered ELISA test has been reported to provide higher sensitivity with equal specificity as a standard 2-tiered serological test (ELISA followed by immunoblotting).[200, 201] A second approach is to test other bodily fluids. In Europe, there are several species of *Borrelia burgdorferi* which limits further the effectiveness of serological analysis. Here the standard is to test the cerebrospinal fluid. Research has also shown that a combination of the sensitivity of PCR (for which the risk of sample contamination outweighs its effectiveness) with an ELISA based antibody detection can produce higher specificity at equal sensitivity than the standard 2-tier serological test.[202] Nanotube transistors have been shown as effective sensors for Lyme disease, immobilizing Lyme antibodies to nanotube FETs and measuring concentration dependent electrical shift at different Lyme target proteins.[203] There have been very

few efforts towards early diagnosis of the bacterium itself directly rather than the antibody response due to the complex nature of the serum solution. Graphene has been shown as a very effective electrical transducer for biological and environmental sensor applications,[27, 120, 124, 132, 142, 186, 189, 190] due to its high mobility and surface to volume ratio. Graphene is ideally suited for the direct detection of Lyme disease making it a high sensitivity, low cost, and scalable alternative to the current diagnosis tools.

In this work, we show the potential of a multiplexed graphene-based sensor array as a solution for direct detection of Lyme disease. The molecular targets are biomarker proteins from the Lyme organism, which offers redundancy in detection, for increased robustness against false positives and false negatives. We developed a wafer-scale fabrication process for arrays of all-electronic Lyme biomarker sensors, where each sensor is a graphene field effect transistor (GFET) functionalized with antibodies to specific target proteins of the *Borrelia burgdorferi* bacterium. Simultaneous detection is done through multiplexed electronic measurement of different areas of the array, each of which incorporates antibodies to a different Lyme protein target. GFETs are fabricated using photolithography compatible processes; they are of excellent quality confirmed with AFM, Raman spectroscopy and electrical measurements. Mobilities are measured at 4800 ± 200 cm^2/V-s and Dirac voltages of 0.5 ± 0.2 V with a yield of 98%. The process is scalable both in the number of GFETs per chip and the number of chips per wafer.

A photoactivated perfluorophenyl azide (PFPA) chemistry is used to create N-hydroxidesuccinimide binding sites on the graphene surface.[105, 194, 204] PFPA contains highly polar carbon-fluorine (C-F) bonds that serve to enhance graphene properties such as the mobility and Dirac Voltage.[196, 197] Exposed amine sites on the antibody proteins react with these binding sites and create chemical recognition for the Lyme disease biomarkers. When reacting the linker to the graphene, and immobilizing the antibody a positive shift in the Dirac voltage is consistent with density of attachment. A concentration dependent, relative to buffer positive voltage response is shown to match the expected Hill-Lanmuir equation of binding. Further, we show that the multiplexing graphene sensor arrays can resolve a mixture of two Lyme targets at distinct concentrations, and the measured response closely resembles the expected concentration as compared to the Hill-Langmuir calibration curves.

5.3.3 Methods

Graphene Synthesis: Graphene was grown using Low Pressure Chemical Vapor Deposition (OTF-1200X-4-C4-SL-UL, MTI Corp.). A Copper foil (46365, Alfa Aesar) was cleaned under sonication with 5.4% Nitric Acid solution for 40 seconds and two DI water baths for 2 minutes, then dried with Nitrogen (N_2) gas. The furnace chamber is pumped down to ~50 mTorr, and then it is filled with 500 sccm of argon gas. The furnace was heated to 1020^{o}C and the copper foil annealed at that temperature under 80 sccm of hydrogen gas. methane is used as a carbon

source, 5 min of 5 sccm followed by 15 min of 10 sccm. The furnace is then rapidly cooled down to 500ºC where methane flow is stopped.

GFET Array Fabrication: Figure 5.8a shows the sensor array fabrication process. A standard two-layer photolithography process (Michrochem PMGI/Shipley S1813) is used to define contact electrodes for 11 sensor arrays on 3" Si/SiO2 250nm wafers as shown in Figure 5.8d. The contacts are metallized with 5 nm Cr as an adhesion layer and a 40 nm Au layer deposited by thermal evaporation, followed by lift-off. The back side SiO2 of the wafer is etched with 1% HF for 6 min to expose the bulk silicon, and rinsed with DI water, followed by evaporation of a 40 nm Au layer to provide electrical contact to the back gate. Each individual array has 50 pair of contacts (source and drain), grouped into the four corners of the chip to allow for multiplexing of up to four different targets. To lower the effects of substrate doping we need to increase the hydrophobicity, the wafer is treated with an HMDS layer by vapor phase deposition (YES EcoCoat 1224P).[93] HDMS only reacts with the SiO2 layer and leaves the gold surfaces bare.

A 3" by 4" piece of CVD graphene on copper (Gr/Cu) is coated with a thin layer of PMMA for mechanical support and "bubble transferred" onto the Si/SiO2/HMDS contact array wafer.[120] The Cu/Gr/PMMA stack is submerged in a 50 mM NaOH solution, and a 30 V potential is applied between the Cu and a counter electrode. Bubbles from hydrolysis form at the Cu surface and mechanically separate the Gr/PMMA, which is cleaned with a triple DI Water bath and transferred

to the final substrate. After drying and a 2 min bake at 150ºC, the PMMA is removed by a 5 min acetone spray and a 1 hour acetone bath. GFET channels are then patterned using two-layer photolithography (Michrochem PMGI/Shipley S1813), and exposed graphene is etched in an oxygen plasma, at 1.25 Torr of Pressure and 50 W power for 35 sec. Lift-off is done with a 2 min bath of Remover-PG (Michrochem) under agitation, a 5 min bath of Remover-PG, a 5 min bath in Acetone and a 2 min bath in IPA. The wafer is then cleaved into individual chips and they are further cleaned through thermal annealing in a tube furnace (Fisher Scientific TF55035A) under a gas flow of 1000 sccm of Ar and 250 sccm of hydrogen at 225ºC.

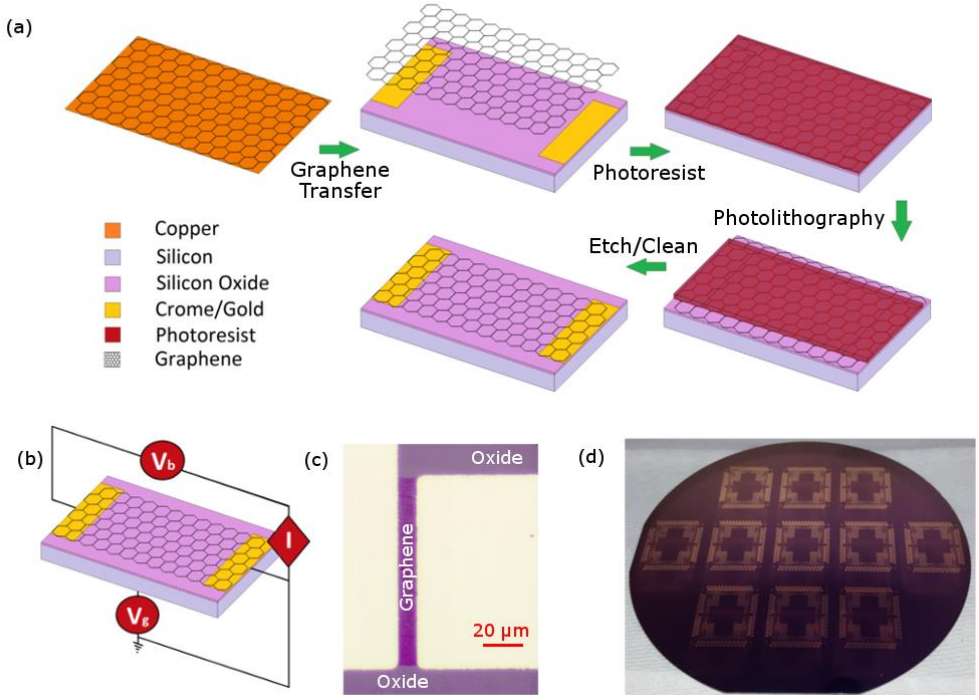

Figure 5.8: (a) Schematic of the GFET fabrication process. (b) Schematic of the electrical probe to characterize graphene devices. (c) Optical Image of a single GFET device. Silicon Oxide (Oxide) regions and graphene are differentiated by a difference in contrast. (d) Optical Image of a 4" wafer after completing fabrication. Process is done at the wafer scale.

5.3.4 AFM, Raman Spectroscopy, and Electrical Measurement:

The topography of the graphene was characterized by an atomic force microscope (AFM, Icon Bruker) equipped with a probe with a tip radius of <10 nm (TAP300Al-G, Budgetsensors). The integrity of graphene was measured by Raman Spectroscopy (RAMAN-NSOM, NT-MDT), after "bubble" transfer onto a Si/ SiO_2 wafer. Electrical measurements were performed in a probe station (Cascade Microtech) at room temperature and atmospheric pressure, using a 200 pin probe card (Accuprobe). Resistance-Gate Voltage (R-V_g) measurements were done using two Keithley ammeters, a 2400 Source Meter to apply the source-drain bias voltage and measure the current and a Keithley 6487 picoammeter/voltage source to sweep a potential across the gate. A National Instruments 1024 Switching Matrix was used to define the actual device under test. Curve parameters were extracted by first removing the baseline (contact resistance) and fitting the measured curve to the form,[45]

$$R_{(V_g)} = \frac{1}{\mu \frac{W}{L} \sqrt{(en_0)^2 + {C_{OX}}^2 \left(V_g - V_D\right)^2}} \tag{5.2}$$

where R is the resistance, V_b is the bias voltage applied, C_{OX} is the oxide capacitance per unit area, V_g is the gate voltage; and we are finding V_D is the Dirac Voltage, μ the mobility, and n_0 the substrate doping per unit area.

Functionalization, Sensing and Multiplexing: Experiments were based on the linker molecule 4-Azide-2,3,5,6-tetrafluorobenzoic acid, succinimidyl ester (6977, Setareh Biotech) (azide-NHS). The GFET arrays are placed in a linker solution of 2.5 mg of Azide-NHS in 25 mL of N-N, Dimethylformamyde (DMF) and exposed to 3 J/cm^2 of 345 nm light. Chips were then cleaned using a DMF, acetone, and Iso-Propanol (IPA) bath for 5 min each, then dried with compressed N_2. After the linker, genetically engineered antibodies are immobilized to the graphene by placing a 10 uL droplet (20 ug/mL in 0.75 mM PBS) in each corner of the chip at 100% humidity for 3 hours.

First we characterize the response for each antibody. This is done by functionalizing all GFETs of several chips to a single antibody. The devices are then measured electrically (100 mV bias, 1 mA current limit, and gate sweep from 0V to -60 V in 2 V steps). Each chip is then assigned a concentration to sense, a single 200 ml droplet of the target solution is placed on the chip (0.75mM solution of the protein in dialysis buffer). The devices are again measured electrically under the same conditions. Dirac voltages are then extracted from curve fitting for each chip before and after target and the shift in Dirac voltage is calculated. This process is done for antibodies 1G2G1 (groS-1), 4B4C10 (groS-2) that are specific to groS target and 4G8D4 (flab-1), 3F11B10 (flab-2) that are specific to flaB target (antibodies were produced by Promab).

5.3.5 Results

After fabrication of a device array, as described in Methods, the graphene is characterized to ensure it is both good quality monolayer graphene and there is minimum residue due to the photolithography and transfer processes. Raman spectrography is used to characterize the quality of the graphene after lithography, the peaks are then identified by a multi Lorentz peak fit shown in Figure 5.9a. Raman shifts of the G peak (1588 cm^{-1}) and 2D peak (2679 cm^{-1}) correspond with the expected shifts for graphene.[80] The G/2D ratio (0.33) corresponds to the signal of monolayer graphene, and the D/G ratio (0.16) suggest a small amount of defects in the graphene. Residues from photoresists or PMMA would appear in the spectrum, no evidence of abnormal peaks suggests that the graphene devices are clean of residues of the processing polymers. Raman spectrum shows a good quality, clean monolayer graphene. Figure 5.9b shows the resistance for different back gate voltages for a typical device array after annealing. Each individual response is highly asymmetric; this difference is usually attributed to contact resistance effects.[205] The curves are fitted to a resistance model, extracting the Dirac voltage, mobility, and neutrality charge. A histogram of the Dirac voltage, and mobility for all the arrays in a single processed wafer (11 arrays, each with 100 devices) is shown in Figure 5.8c-d. Mobility is calculated at 4952 ± 1682 cm^2/Vs and Dirac voltage at 0.5019 ± 2.712 V. Conventional imaging resists contain aromatic rings that can non-covalently bind to graphene through Van der Waals

interactions,[125] and the use of a protective layer like PMGI is then necessary to allow a more effective surface cleaning of graphene. The effectiveness of our process is shown with the low Dirac voltage and high mobility across the entire wafer for the complete process. This allows for a scalable, high yield, and high performance devices compared to other processes. [97, 135]

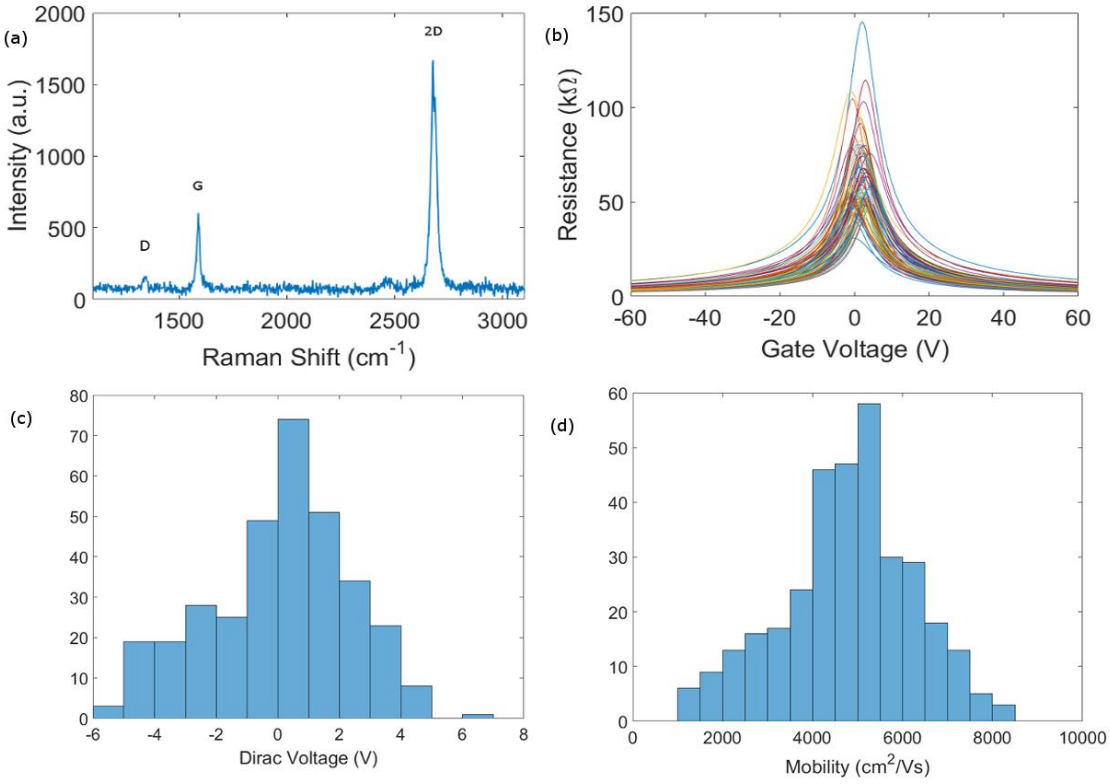

Figure 5.9: (a) Raman spectrum for a fully patterned GFET channel. The G/2D ratio is 0.33 and D/G ratio is 0.16, in agreement with low defect monolayer graphene. (b) Graphene resistance as a function of gate voltage with subtracted linear baseline for an entire array of GFET. Device yield is 98%. (c-d) Histogram of the Dirac voltage (panel c) and mobility (panel d) for a total of 1100 GFET devices (11 arrays of 100 devices each) from a single fabrication process.

The structure of Azide-NHS as well as the product of the reaction with graphene after photo-activation is shown in Figure 5.10a. The actual binding chemistry[8, 102, 180, 195] is caused by a photoactivated Azide anion (N_3) decomposed into a nitrogen molecule (N_2) nitrene (N^-) which binds with two contiguous carbon atoms. To complete the fabrication of the biosensor, an antibody is attached to the linker molecule using the procedure described before. Amine (NH_2) groups that are very prevalent in most proteins can readily bind with the N-hydroxysuccinimide (NHS) from the linker. Atomic Force Microscopy is used to characterize both steps of the functionalization process. Figure 5.10b shows the AFM image of an as fabricated graphene device, a device after pyrene-NHS attachment and a device after the antibody attachment. Figure 5.10c shows a comparison of line scans on each of the corresponding images. From the line scans the average height of the graphene is 0.95 +/- 0.19 nm, and the average height of the Azide-NHS layer is 1.65 +/- 0.20 nm. When protein binding occurs, the linker loses the succinimide ester group making the height measured by AFM lower than the actual protein height. The average protein height, measured as the difference between the high points in the line scan and the average height of the Azide-NHS layer, is 1.46 +/- 0.24 nm.

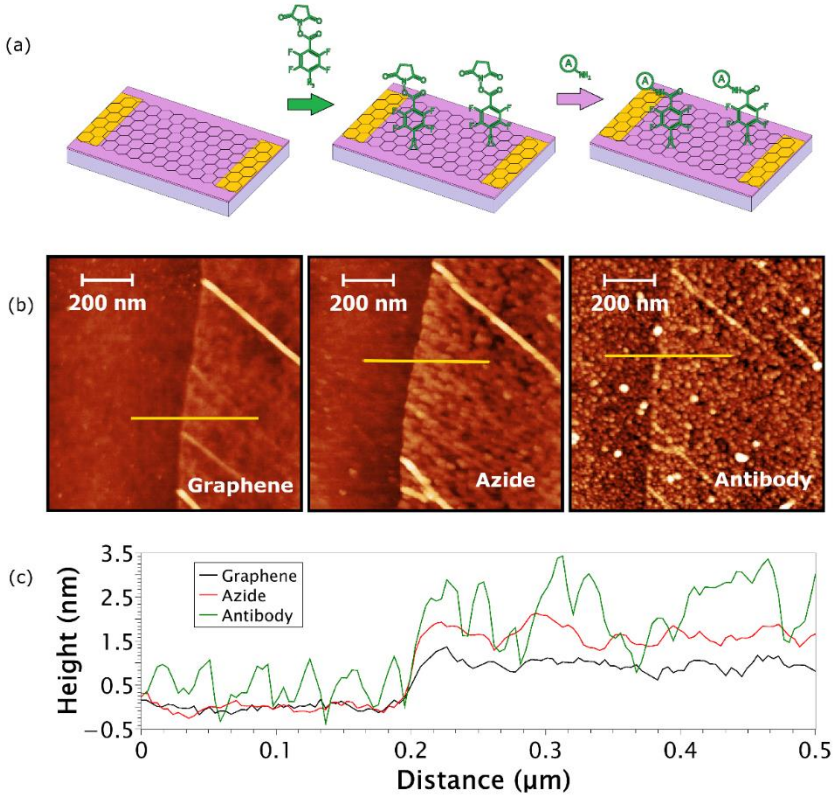

Figure 5.10: (a) Schematic for the binding chemistry of the linker molecule and the antibody protein. (b) AFM images of graphene at various steps in the process. Left: As-transferred graphene. Middle: After azide attachment. Right: After antibody immobilization.

The responses of each of the antibodies is characterized by measuring the shift between the response before the target (after antibody) and after the target. The curves are modelled using equation (5.2, and the shift in Dirac voltage is calculated. Figure 5.11a shows the target binding against the antibody, and Figure 5.11b shows the resistance curve for a typical response of a target-antibody binding of a single device. A relative to the buffer response is used to determine the sensor calibration. Sensors are expected to respond under the Hill-Langmuir binding dynamics model.

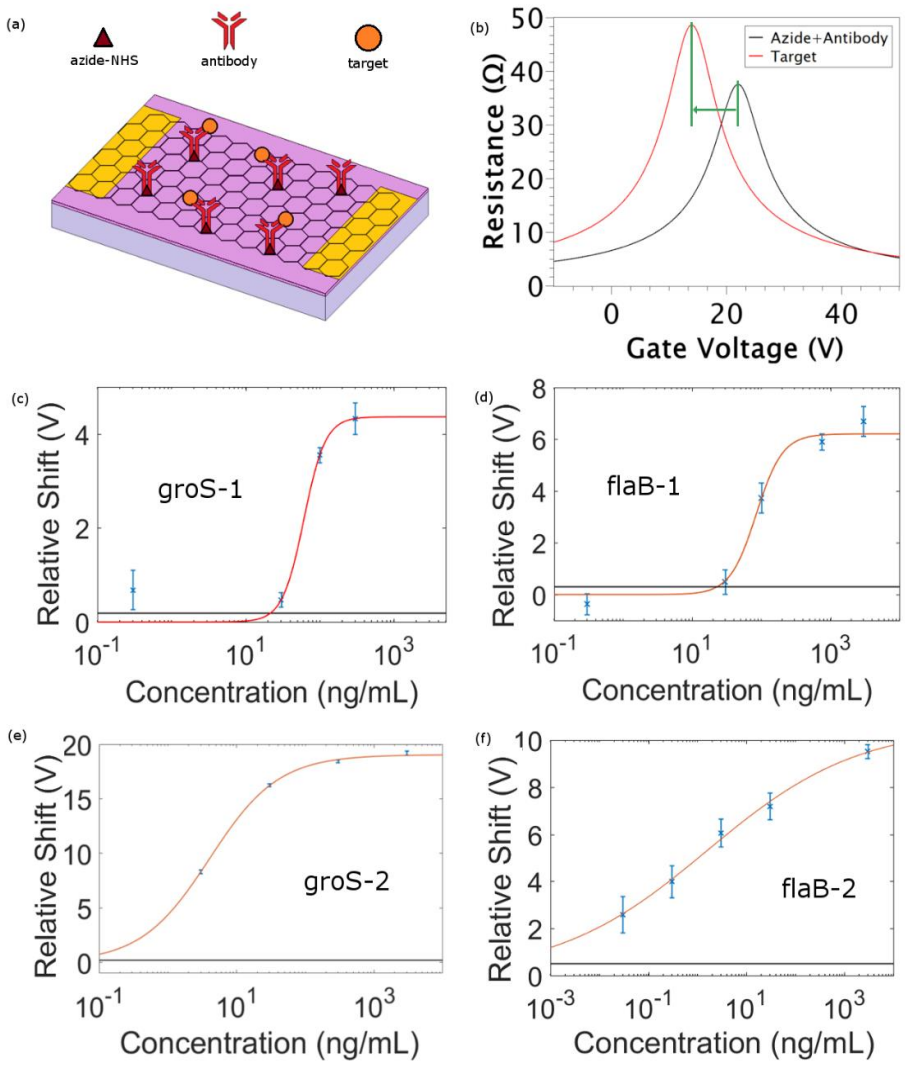

Figure 5.11: (a) Schematic of antibody/target binding. (b) R-Vg characteristic shows a shift after exposure to the target. Azide/antibody curve (black) is the reference and it shifts towards the target curve (red). (c-f) Concentration dependent responses (relative to buffer) of antibody/target pairs fitted by Hill-Langmuir model of binding dynamics. (c) GroS-1 antibody, (d) groS-2 antibody, (e) flaB-1 antibody, (f) flaB-2 antibody.

$$\Delta V = V_0 \frac{\left(\frac{c}{K_a}\right)^n}{1 + \left(\frac{c}{K_a}\right)^n} \tag{5.3}$$

where ΔV is the relative to buffer response, c is the target concentration, K_a is the dissociation constant (concentration where association and dissociation are in equilibrium), V_0 is the saturation response, and n is the cooperativity. We measured a total of two different targets, each one with two variants of antibodies shown in Figure 5.11c-f.

A similar process as the one described in Methods is used to characterize the multiplexing response to different antibodies in the GFET array. The antibodies used were selected due to their similar cooperativity. Both responses show a steep change in the relative response, this allows for the concentrations to be tested to be of clinical significance. As in the insert of Figure 5.12, one section of the chip is functionalized with groS-1 antibody and a different section for flab-1 antibody. All previous steps before the antibody attachment are the same as described before, applied to the entire chip. For multiplexing it is important to keep the volume of the droplets in each section contained to avoid mixing, both during incubation and rinsing. The devices are then measured electrically (100 mV bias, 1 mA current limit, and gate sweep from 0V to -60 V in 2 V steps). A 200 ml droplet of the target mixture solution (30 ng/mL of groS and 3000 ng/mL of flaB in 0.75 mM PBS) is placed on the chip for 1 hour. The devices are measured electrically using the same conditions as before, Figure 5.12 shows relative voltage shifts for both sections of the same chip. For each section of the chip corresponding to the groS-1 and flab-1 antibodies, devices are normally distributed with an average of 0.84 +/- 0.45 V and

13.94 +/- 0.27 V, respectively. These values are close to the expected values as given by the calibration curves of each of the antibodies (0.47 V for groS-1 and 18.59 V for flab-1).

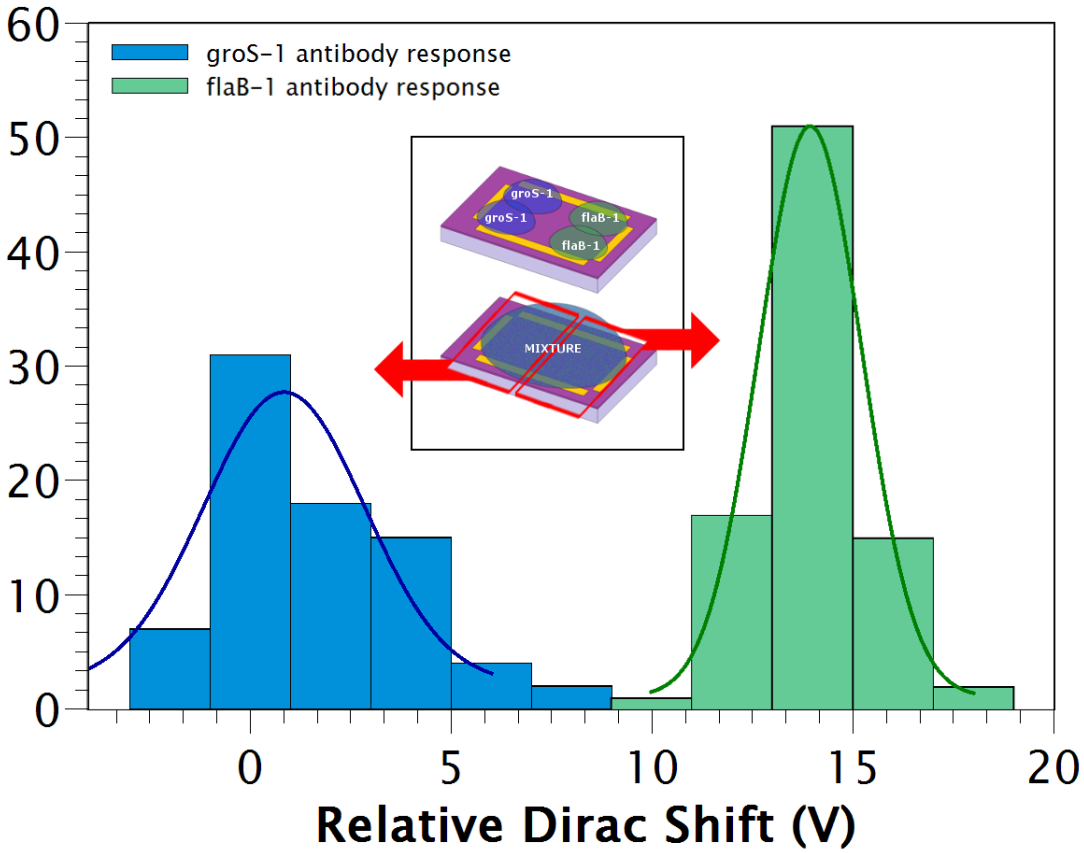

Figure 5.12: Relative to buffer Dirac shift for two sets of arrays. Insert shows a schematic of the multiplexed array. Each array is functionalized with groS-1 antibody on the top section of the array and with flab-1 on the bottom section of the array. A mixture of groS target (30 ng/mL in 0.75 mM dialysis buffer) and flaB target (3000 ng/mL in 0.75 mM dialysis buffer) is sensed by the entire chip. An accumulated histogram of the responses (relative to buffer) for both chips is shown, top section in blue and bottom section in green.

5.3.6 Conclusion

To summarize, a high yield, high quality, scalable fabrication process for graphene arrays has been developed. The fabrication process is a full wafer scale, photolithography compatible process. A full sheet of graphene is transferred to a pre-patterned metal contacts wafer where the graphene channels are then defined, the cleaning protocol includes a solvent soak and anneal is designed to remove most polymer residues while minimizing any damaging effects to the graphene. Graphene after fabrication shows a clean monolayer with low amount of dislocations as shown in their Raman spectra where the G/2D ratio is 33% and the D/G ratio is 16%, GFET arrays show excellent electrical properties with mobilities of 4952 +/- 1682 cm^2/Vs and Dirac voltage at 0.5019 +/- 2.712 V. The linker chemistry used provides a high-density layer of antibodies (as shown by AFM imaging) covalently bound to the graphene with minimum effect on mobility, while chemically gating the devices causing a Dirac voltage shift. The sensors are calibrated by four different Lyme antibodies that correspond to two different targets (each target can bind to two antibodies). Mixture detection is then demonstrated by multiplexing the sensing signal to separated sections of the same chip, functionalizing each section with antibodies corresponding to the targets in the mixture. The measured response shows a distribution of devices at different values, whose average closely resemble the expected values obtained from the calibration curves for each antibody/target pair.

5.4 SUMMARY

In this chapter, we detail two chemical linkage mechanisms for protein functionalization to graphene. First, we compare the covalently linked azide-NHS to the non-covalent linked pyrene-NHS using scFv HER3 antibody for both linkers as a benchmark response. The photoactivated linker azide-NHS has dipolar C-F bonds that improves mobility, electron-hole transport, enhance the protein receptor density and target recognition signal with respect to the more commonly used pyrene-NHS linker. However, devices for both linker chemistries show excellent sensitivity and selectivity as tested against the non-target UPAR. We then show the capability of GFET arrays for multiplexing the sensing signal of complex mixtures, by functionalizing different regions of the array with different protein chains from the bacterium of Lyme disease. The sensors differentiate signals of the target mixture, and show a value that closely resemble the calibration curves for each antibody/target pair.

6 CONCLUSIONS

In this chapter, we summarize the results of the experiments described in this thesis. We also detail research prospects that can be pursued based on the work presented here.

6.1 SUMMARY

Graphene has many properties to revolutionize modern technology. Since its discovery, it has been shown in several applications such as touch screen displays,[206, 207] high frequency electronics,[208, 209] energy storage,[210, 211] and field emitter antennas,[212] to name a few. Since the isolation of graphene through mechanical exfoliation our understanding of single layer materials has allow us to grow them through chemical vapor deposition (CVD).[87, 213] Aside from graphene, other materials like Boron Nitride,[214, 215] and transition metal dichalcogenides[216] have also been grown through CVD. Aside from excellent electrical, thermal, and mechanical properties graphene also exhibits properties like the Quantum Hall Effect[217] and fractional Quantum Hall Effect[218, 219].

In this thesis, we aim to develop a set of tools necessary for wafer scale fabrication of graphene field effect transistor (GFET) arrays for biosensing applications. The GFET arrays are used as electrical transducers for biomolecules chemically bound to the graphene channel surface. The biomolecules will cause an electrostatic change when doing conformal changes in their structure (folding, or

binding a target) and the GFETs conductivity is a function of this electrostatic change. We start by developing a model for our GFET devices such that it matches electrical parameters that we can characterize in the laboratory and to understand the linking mechanism of biomolecules. Then we define two linking mechanisms, thiol binding mediated by nanoparticle (NP) and amine binding through a succinimide ester.

The graphene model used is an approximation derived of first principles, where the conductivity of the graphene is calculated as the charge density in the channel. From band theory of solids, we show that the charge density depends linearly on the electric field applied on the back gate. Graphene underneath metal contacts is shown to exhibit both pinning and doping causing an electric field dependence for the contact resistance, which we model as a linear approximation. Considering all effects, we can write the graphene resistance as,

$$R = R_0 + R_s\left(V_g - V_D\right) + \frac{1}{\mu\frac{W}{L}\sqrt{(en_0)^2 + C^2\left(V_g - V_D\right)^2}} \tag{6.1}$$

where the details of the equation are shown in section 2.1. We also detail some important characteristics of the biomolecules presented in this thesis, deoxyribonucleic acids (DNA), and immunoglobulins (antibodies). It is important to understand the linking mechanisms to develop a comprehensive set of chemistry processes to link the biomolecules to graphene.

We detailed the processes and tools necessary for a wafer scale fabrication of graphene devices. The entire process is compatible with all microfabrication industry standards. We show that our CVD graphene shows minimal contamination, excellent structural, and electrical properties. Fabrication of GFET devices show above 95% yield, above 3000 cm^2/V-s mobilities and approximately 0 V Dirac voltage.

Nanoparticle mediated functionalization binds to a thiol in the biomolecule by forming a metal sulfide (*e.g.* AuS or PtS) bond. Here we present two approaches. First, we demonstrate DNA binding through a monodisperse layer of gold NP. Gold is deposited by thermally evaporating a thin layer before graphene transfer and thermally annealing after photolithography. We verify graphene quality and cleanliness by Raman spectroscopy and x-ray photoelectron spectroscopy (XPS), and NP deposition atomic force microscopy (AFM). Thiolated single strand DNA (ssDNA) is bound as a receptor biomolecule through a thiol bond to the NP to realize a very sensitive and highly specific biosensor. Then, we show a thiolated antibody binding through a pyrene functionalized platinum NP. Nanoparticles are chemically bound to the graphene surface by a pyrene amine linker, where the pyrene functional group π-π stacks with graphene and the amine functional groups binds to the nanoparticle when in its +I oxidation state due to relativistic fluctuations. Graphene quality and cleanliness is verified through Raman spectroscopy, and NP attachment and distribution through AFM and SEM. An scFv HER3 antibody, a biomarker for

breast cancer, is used. We show a highly specific sensor response, with 10 pM limit of detection. Control experiments reveal a highly selective response against non-targets, and non-specific binding.

Primary amines are very frequently occurring in most proteins. Amines can react with succinimide esters to form an amide bond. We explore two different functionalization chemistries for graphene, covalent and non-covalent, both of which have a succinimide ester functional group available to react with an amine. We use a pyrene bifunctional linker that π-π stacks with graphene to form a non-covalent functionalization. This method has the advantage of being non-invasive to the crystallographic structure of graphene. We also use a photoactivated perfluorophenylazide bifunctional linker that covalently attaches to both carbon atoms in each unit cell. A mobility increase from this functionalization is attributed to the dipole layer formed by the C-F bonds in the linker. An scFv HER3 antibody is used for which the covalent linker shows an enhanced response, similar limit of detection of a few nM. Control experiments are done towards the non-target UPAR and shows highly selective sensors due to the antibody response. Finally, we show the detection of complex mixtures by designing a multiplexing array. Regions of the array are functionalized with different antibodies corresponding to a Lyme disease target. Detection for each of the targets is shown individually and we measure the response curves. The sensors differentiate signals of the target mixture, and show a value that closely resemble the calibration curves for each antibody/target pair.

6.2 RESEARCH PROSPECTS

Graphene Field Effect transistor arrays provide an excellent transduction platform for sensing applications. Combining excellent electronic properties with biomolecules yields highly selective, ultra-sensitive detection mechanisms for biological applications. While the results in this thesis are encouraging in terms of performance and scalability there is much work to be done for them to become commercially available. Here we present, a few approaches to improve the operation and design of these devices.

6.2.1 Monodisperse Nanoparticles

In this thesis, we presented nanoparticle (NP) mediated sensor arrays. The NPs are used as a linker to bind a biomolecule to the graphene channel in a GFET. It is important however to study the graphene-noble metal NP interaction to understand the electrostatic signal enhancement, and the deposition physics to be able to control the density and size of the NP.

The most commonly reported interaction between graphene and noble metals is surface plasmon resonance (SPR), where photons from a light source resonate at the same frequency as the oscillations of an electron gas of the noble metal and SPR effects are enhanced by the graphene sheet. SPR enhancement has been reported for biosensors between graphene and noble metal films,[220] noble metal nanoparticles,[221]

and for Surface Enhanced Raman applications.[222] There has been very little research into electrostatic interactions between graphene and noble metal NP.

Research done by Bechalany, et.al.[11] focuses on the synthesis of gold nanoparticles by thermal annealing. The distribution of particle size and density is then studied as a function of its synthesis parameters, such as annealing temperature, gold thickness during deposition, and atmosphere during the annealing process. The study is done on thermally oxidized silicon wafers as substrate.

Figure 6.1 and Figure 6.2 show the effects of temperature on the distribution of NP size. The mechanisms that drive the formation of nanoparticle can range from coalescence to Ostwald ripening, the former dominates at lower temperatures and NP are skewed to larger sizes while the latter dominates at higher temperatures and sizes tend to be smaller. As annealing temperature increases the dominant effect changes from coalescence to Ostwald ripening and NP become smaller.

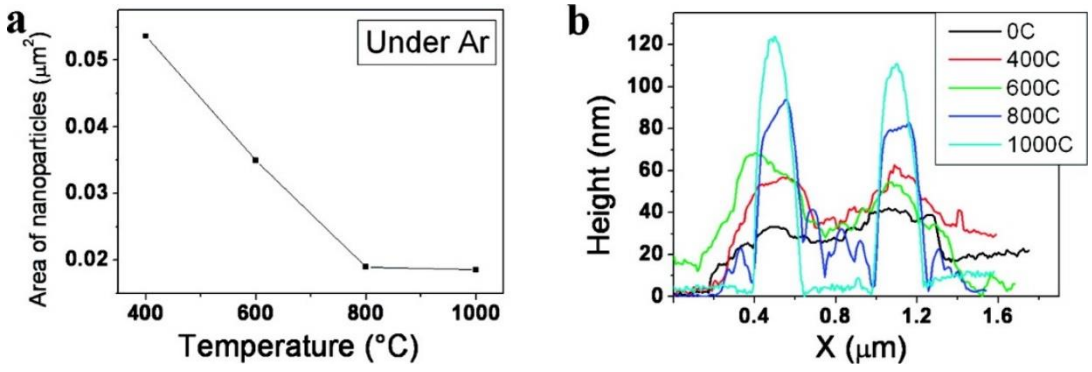

Figure 6.1: Variation of the Au nanodot area deduced from SEM images (a) and of the nanodot heights deduced from AFM measurements (b). All data have been taken after thermal annealing of Au island films on Si substrates in Ar for 1 h at various temperatures.[11]

Histograms in Figure 6.2 show NP size distribution with increasing temperature. Not only do NP get smaller but the deviation of particle size gets smaller as well. We attribute this to the systems effort to minimize surface energy for increasing temperatures.

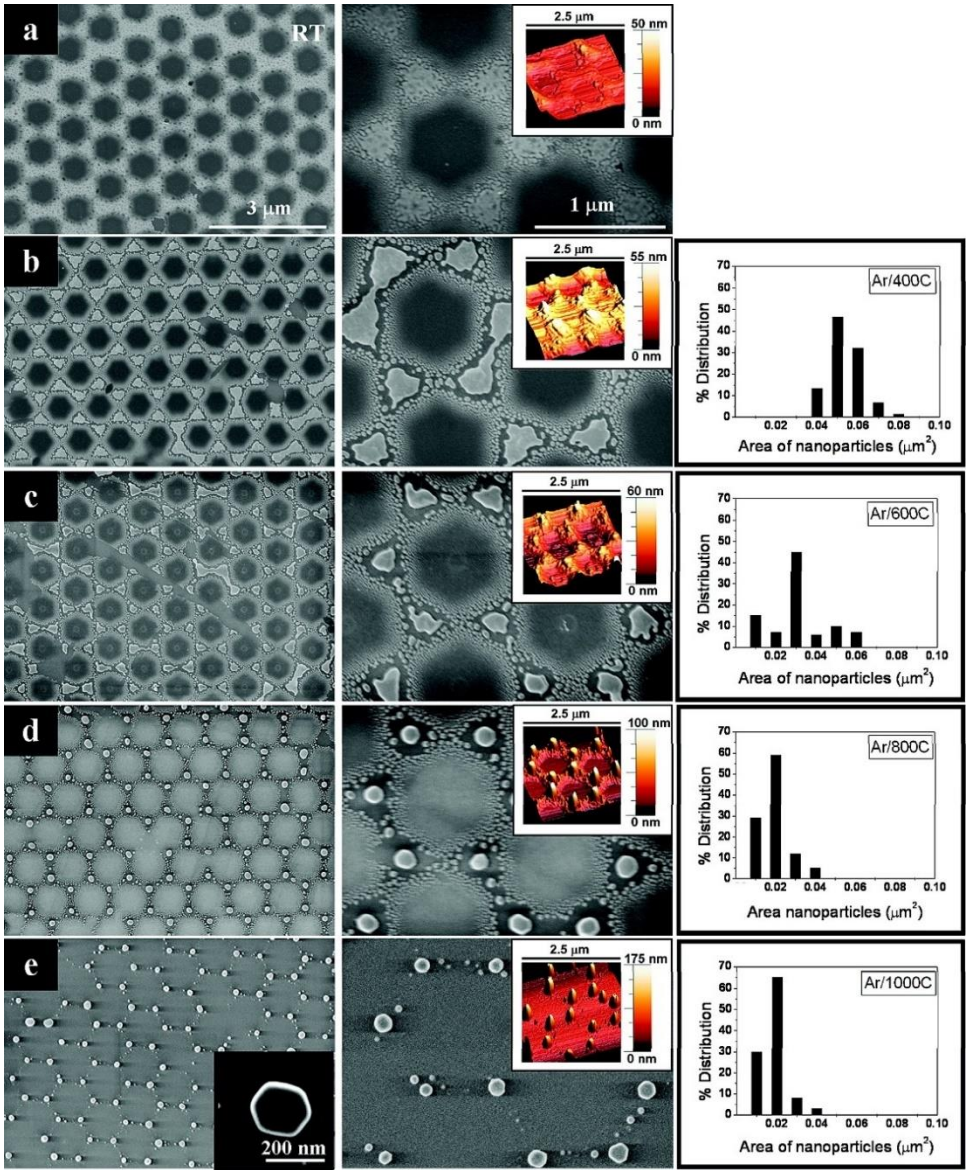

Figure 6.2: SEM and AFM images of a honeycomb Au mask prior to annealing (a) and SEM and AFM images of annealed Au island films on Si substrates in Ar for 1 h, and variation of the area distribution of Au nanoparticles depending on annealing temperature: (b) 400, (c) 600, (d) 800, and (e) 1000 °C.[11]

The amount of available material also influences the NP size distribution. All measurements were for NP annealed at 100oC in Ar atmosphere for 1 h. Figure 6.3a-d are SEM images of NP distribution for increasing thickness of gold during deposition. Figure 6.3e shows NP size as a function of gold thickness, it is important to note the size limit reached after 200 nm.

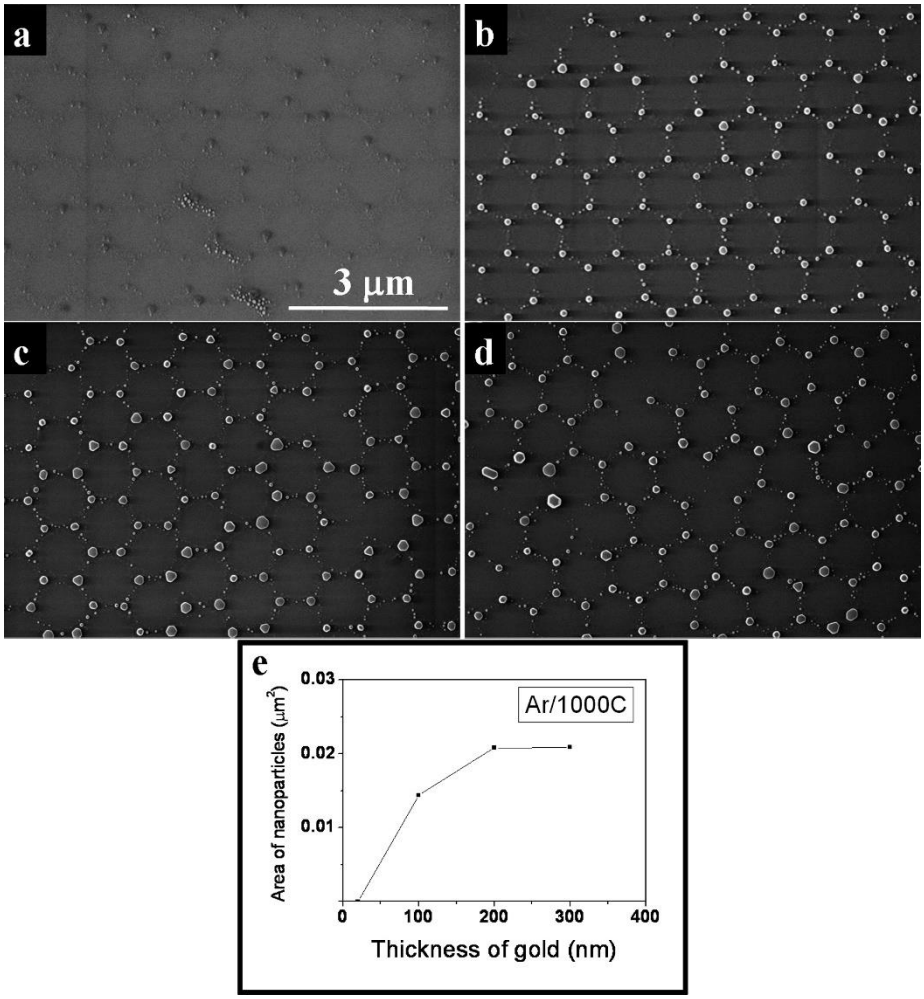

Figure 6.3: SEM images of hexagonal arrays of Au nanodots fabricated by annealing at 1000 °C in Ar atmosphere for 1 h. The diameter of the PS spheres was 1000 nm, and the thicknesses of the sputtered Au films varied: (a) 20 nm, (b) 100 nm, (c) 200 nm, and (d) 300 nm. Panel (e) shows the nanodot areas deduced from SEM data as a function of the thickness of the sputtered Au films measured by a quartz crystal microbalance.[11]

Figure 6.4 shows the effect of the atmosphere during annealing on the distribution of the NP. While Ar and Air seem to have similar distributions, N_2 is much sharper. This suggests that nitrogen lowers the deviation of nanoparticle size. H_2 and vacuum have a negative effect on the distribution, hampering the synthesis of well-formed NP.

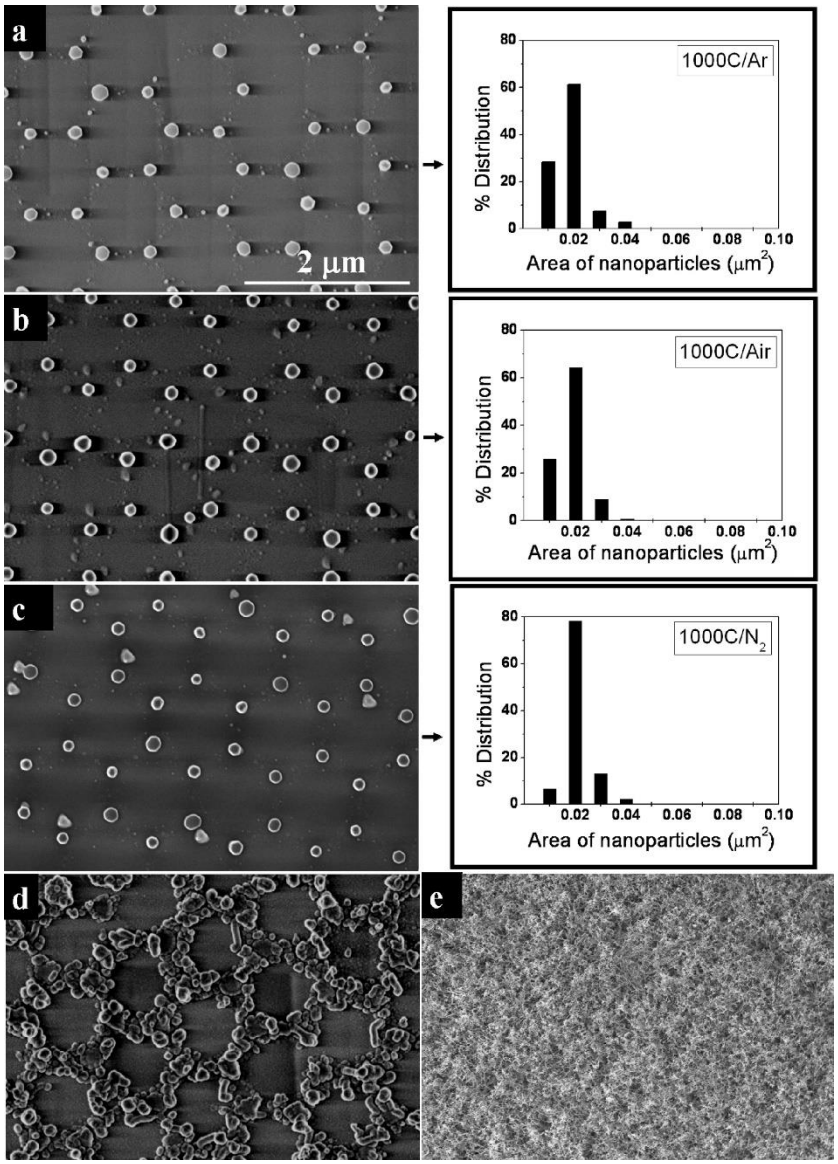

Figure 6.4: SEM images of Au nanodot arrays that formed after Au film sputtering (200 nm thick) through PS sphere shadow masks onto Si substrates and after annealing at 1000 °C for 1 h in different atmospheres: (a) Ar, (b) air, (c) N2, (d) mixture of Ar and H2, and (e) vacuum.[11]

We then propose a similar study where the substrate is as-grown CVD graphene (on the copper foil) and transferred to a thermally oxidized silicon wafer. Limitations to the parameters need to be considered such as the temperature during the anneal such that graphene retains good electrical properties. Additionally, we want to characterize the effects of changes in density and size of NP to the graphene conductance.

6.2.2 Linker Density

Linker density is an important parameter for sensitivity, it determines biomolecule density which enhances the electrostatic signal to be detected by the GFET transducer. In this thesis, we presented two chemical linkers, covalently linked and noncovalently linked, that produced a sparse layer of biomolecules of a few hundred biomolecules per μm^2.

Ping, et.al.[12] show that pyrene-NHS can be used as a chemical linker to immobilize probe DNA molecules onto graphene with such a high density that individual biomolecules cannot be distinguished by AFM (Figure 6.5a). They note however that the height increase is consistent with the expected size of the DNA chain, about 1.2 nm. The positive shift in Dirac voltage (Figure 6.5b) is attributed to hole doping in the graphene caused by chemical gating from the negative charges of DNA. It is calculated that carrier density is $\sim 3.0\times10^{12}$ μm^{-2}. Assuming 22

negative charge in the DNA chain, the separation between biomolecules is ~25 nm, causing a very dense layer as seen by AFM.

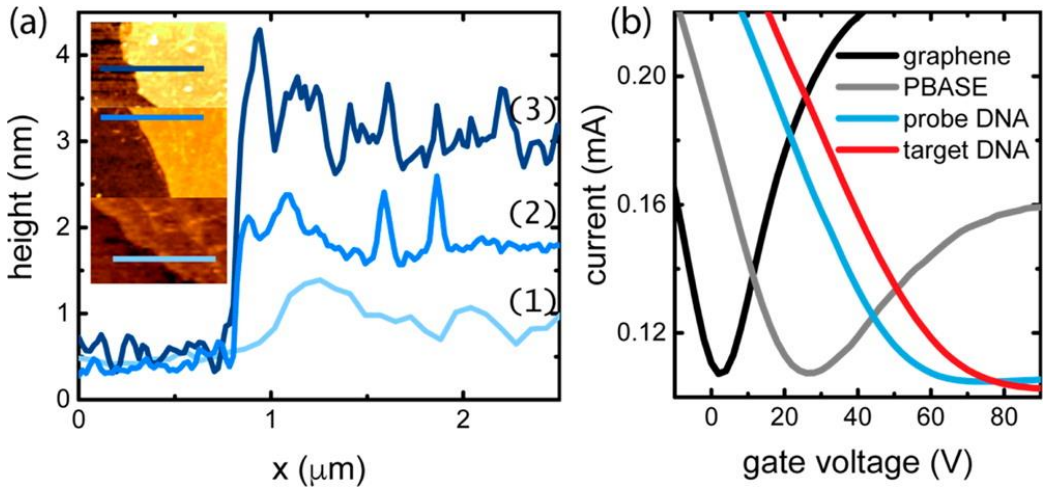

Figure 6.5: (a) AFM line scans of (1) annealed graphene, (2) PBASE functionalized graphene, and (3) graphene functionalized with PBASE and aminated DNA. Inset: AFM images showing the scan lines plotted in the main figure. Scan lines are 2.5 μm. Z-scale 8 μm. (b) I−Vg characteristics for a typical GFET that was annealed, functionalized with PBASE, reacted with 22-mer aminated probe DNA, and exposed to 10 nM target DNA in deionized water.[12]

The methodology for linking the DNA to graphene with pyrene-NHS is like the one used in this thesis. The incubation time in the linker solution is done for 20 h, which suggests that the has longer incubation times lead to better coverage of the linker. It seems to be a self-regulating process that once full coverage is achieved no more linker is deposited in the surface. Further research into the time dependent kinematics of the pyrene-graphene binding need to be done, as well as the density effect that it will have on other biomolecules.

For azide-NHS the parameter that controls the attachment density is the amount of active reacting molecules. Azide is a photochemically activated compound, with the addition of light (or heat) the azide decomposes to a nitrene.

The cycloaddition of nitrene with graphene is extremely fast due to its highly reactive nature. The attachment density depends on the amount of available nitrene groups in the graphene surface, which is controlled by the dose of energy density during light exposure. Figure 6.6 shows AFM images for two processes with two doses of energy density. Exposure for lower times shows increased roughness indicating a sparse attachment compared to its longer time counterpart.

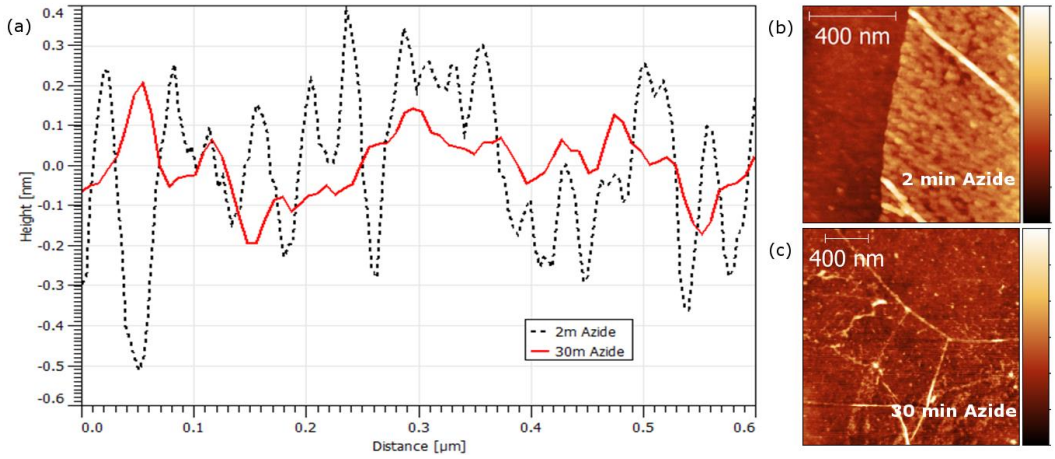

Figure 6.6: (a) Height profile of two linkage chemistry processes for azide-NHS taken by AFM. 2 min exposure (black-dashed) and 30 min exposure to 25 mW/cm^2 365 nm light. (b-c) AFM image of (b) 2 min exposure, and (c) 30 min exposure.

We characterize the effects of higher attachment density of antibodies. Figure 6.7a shows the Resistance as a function of gate voltage for two GFET devices, where dashed lines show devices before functionalization and solid lines show devices after azide-NHS/antibody functionalization, for 2 min exposure (red curve) and for 30 min exposure (blue curve). Figure 6.7b shows the concentration dependent response from sensing the corresponding target, for 2 min exposure (red curve) and for 30 min exposure (blue curve). We note an increase in the Dirac voltage shift

and an increase in saturated sensor response. The ratio between the Dirac voltage shifts is 0.33 V and the ratio between the saturated responses is 0.34 V. We attribute both changes to an increase in the chemical gating to higher attachment density.

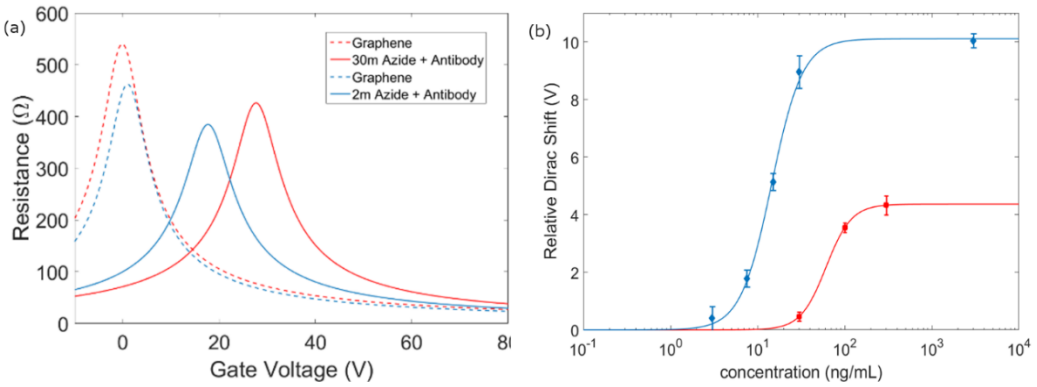

Figure 6.7: (a) R-Vg curves for two GFET devices (colored red and blue), dashed lines show devices before functionalization and solid lines show devices after azide-NHS/antibody functionalization. (b) Hill-Langmuir concentration dependent response for 2 min exposure (red) and for 30 min exposure (blue).

6.2.3 Engineered Biomolecules

The selectivity, specificity and selectivity from the Nano/bio hybrid sensors presented here comes from the engineered biomolecules. We used a genetically engineered antibody fragment, the single chain variable fragment (scFv) that is the active binding region of the immunoglobulin. The use of scFv can be extended for multiplexing to improve the sensitivity of results. There are additional modifications that can be done to proteins to further enhance the electrostatic signal. Yongki, et.al.[16] show the effect of genetically increasing the electrical charge at a specific location of the protein chain. In their research, they fabricated carbon nanotube field effect transistor (CNTFET) based sensors that consist of a single nanotube channel,

and a single biomolecule attached. They measure the response signal of a Lysozyme molecule completing a function over several cycles. Figure 6.8 shows the protein response, when positions 83 and 119 of the chain were mutated to have different charges (+2, +1, 0, -1, -2). The sensor response is shown to depend on the charges close to the graphene. The effect of engineering additional charges in the antibody chain such that these charges are in proximity to graphene could further enhance the electrostatic signal transduced by the GFET arrays in this thesis.

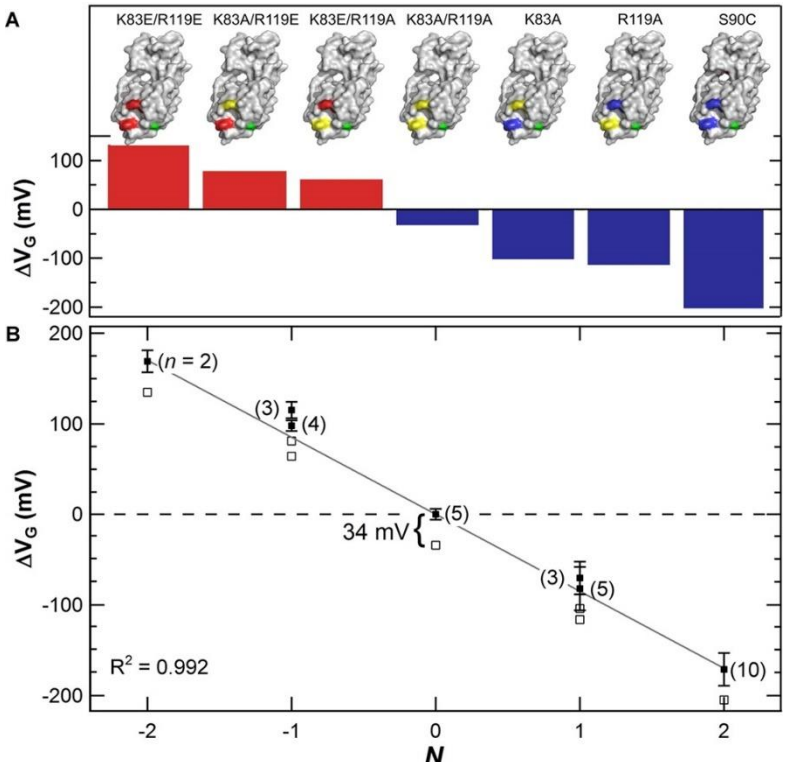

Figure 6.8: Average transduction by seven charged variants. (A) Lysozyme positions 83 and 119 were mutated to have positive (blue), neutral (yellow), or negative (red) charged side chains. The effective gating ΔVG by each variant varied from 135 to −205 mV, with a value of −34 mV for the neutral N = 0 variant. (B) For all variants, ΔVG is nearly proportional to N, with a slope of −85 ± 2 mV per unit charge. Raw data (open squares) shifted up +34 mV (solid squares) results in a response symmetric around zero. Error bars indicate three standard deviations as determined from n (indicated in parentheses) different devices fabricated with each particular variant.[16]

A second option to improve sensitivity and selectivity are aptamer beacons. Aptamers are oligonucleotides that have been selected to bind to a specific molecular target. They can consist of RNA, DNA or modified nucleotides and are typically less than 100 bases long.[223, 224] Aptamers have been used for biosensor applications with reduced graphene oxide (rGO),[225] graphene,[226] carbon nanotubes,[227] nanorods,[228] and nanoparticles.[229] The oligonucleotide primary and secondary structure are designed such that on folding they conform to a desired shape and allow binding to a specific biomolecule.

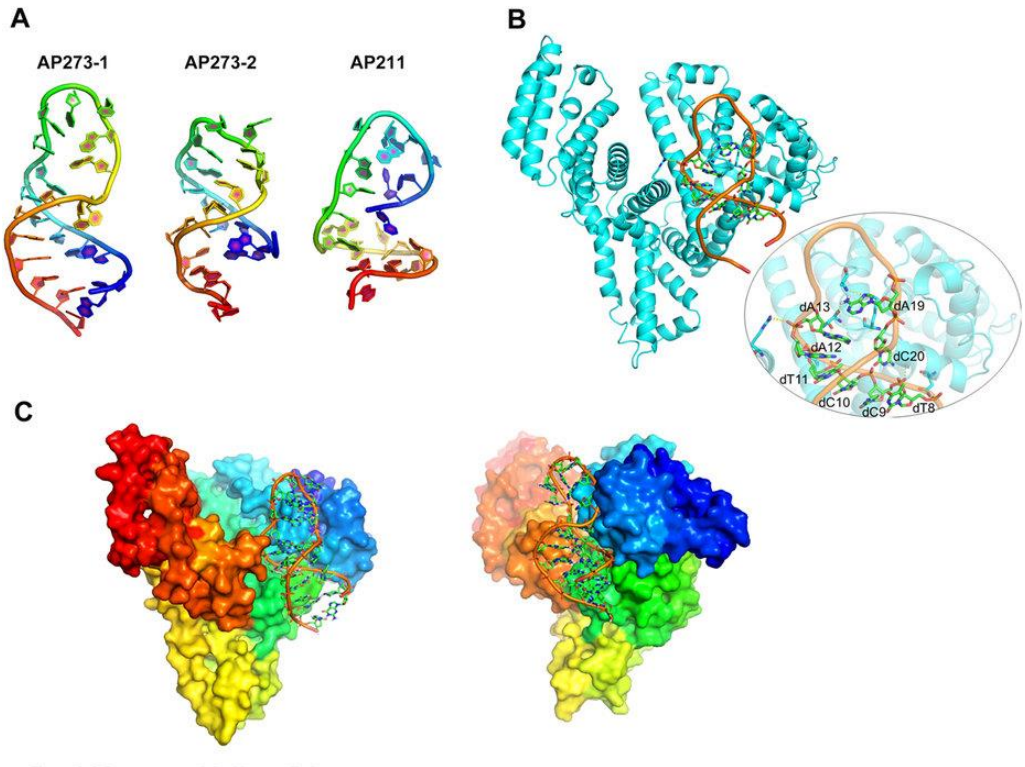

Figure 6.9: (A) Three-dimensional structures of AP273 and AP211. The motifs of AP273 can be folded into 2 kinds of structures, AP273-1 and AP273-2. (B,C) A docking model between AP273-1 and AFP protein. In particular, dC9, dC10, dT11, dA13, dA19, dC20 are in close contact with AFP. C, T and A represent the bases and the number represents the location of the base in the ssDNA sequence. (C) A 3-D interacting mode observed from two views.[15]

6.2.4 On-Chip Processing

The fabrication process presented in this thesis is fully scalable on the number of devices built into the chip. However, currently measurements of all transistors in the array, becomes significantly slower with increasing device number. While our current measurements are done with a switching matrix that rapidly changes from one device to the next, the process can become too slow for the time scale required for biomolecules. On-chip processing is one solution to this problem, where a full array of GFET devices could be probed using a single set of outputs. Signal averaging of the sensor responses is done directly on-chip.

A. APPENDIX: RECIPES

A.1. GRAPHENE GROWTH

Copper Foil Preparation

1. Cut a 99.9% Copper foil piece, such that it fits flat inside the furnace chamber (usually a quartz holder is needed)
2. Clean the foil in 5.4% HNO_3 for 40 sec
3. Transfer two DI water baths for 2 min and blow dry with N_2
4. Place the side of the foil (side NOT touching glassware) face down on the quartz holder. This bottom part of the copper will have the highest-quality Graphene

Graphene Growth

1. Ensure the furnace is placed such that there is enough space to slide it out of the sample area after the process is complete. Rapid cooling is vital for proper graphene growth
2. Load the holder and copper foil into the tube furnace
3. Pump vacuum in chamber down to 50 mTorr
4. Start a gas flow of 500 sccm Ar, and 80 sccm of H_2
5. Heat furnace up to 1020 ^oC
6. Anneal at 1020 ^oC for 30 min
7. Flow 5 sccm of CH_4 for 5 min, then increase to 10 sccm

8. After 20 min growth (5 min at 5 sccm and 15 min at 10 sccm of CH_4) cool the furnace by turning off the heating and slightly cracking open the furnace. CH_4 flow remains on
9. At 900 ^oC slide the furnace away from the sample area
10. At 500 ^oC fully open the furnace and turn off the CH_4 flow
11. At 80 ^oC the furnace can be return to atmospheric pressure and the copper/graphene removed and stored

A.2. METALIZATION PHOTOLITHOGRAPHY

Metal Contacts Pattern

1. Spin coat resist layer:
    a. PMGI – 4000 rpm, 1000 rpm/s, 45 s. Hotplate bake 210 °C for 5 min
    b. 1813 – 5000 rpm, 1000 rpm/s, 45 s. Hotplate bake at 115 °C for 2 min
2. Expose the Si/SiO2 wafer with the metal contact mask. Use Hard Contact Lithography and expose for 140 mJ/cm^2 (for a 50 mW/cm_2 362 nm lamp exposure time is 2.5 sec)
3. Drop into developer (typically MF319) bath, blow gently at chip with plastic pipette. Should develop in ~ 1 min but needs to be monitored
4. Move sample to running DI water bath for 30s, blow dry with N2

5. Evaporate 5 nm Cr and 40 nm Au in a metal evaporator, without removing vacuum to avoid oxidation. General rate is 0.1 A/s for chrome and 1 A/s for gold evaporation
6. Drop sample into resist remover (typically Remover PG or 1165) bath and sonicate for 10 m at 60 °C
7. Move to fresh remover bath and leave overnight
8. Drop in acetone bath for 5 m. Rinse clean with IPA

Metal Back Gate

1. Spin coat resist layer:
    a. 1813 – 5000 rpm, 1000 rpm/s, 45 s. Hotplate bake at 115 °C for 2 min
2. Etch the backside of the SiO2 by submerging in a BOE (6% Hydrofluoric Acid) for 6m, clean by submerging in a DI water circulating bath
3. Evaporate 40 nm Au in a metal evaporator, general rate is 1 A/s
4. Drop sample into resist remover (typically Remover PG or 1165) bath and sonicate for 10 m at 60 °C
5. Move to fresh remover bath and leave overnight
6. Drop in acetone bath for 5 m. Rinse clean with IPA
7. Use the dicing saw to cut the wafer into small chips to use later
8. Clean in an acetone bath, spraying with acetone before. Leave for 5 minutes. Rinse clean with IPA

A.3. GRAPHENE PHOTOLITHOGRAPHY

Graphene Photolithography

1. Starting with a fully transferred Graphene piece on a metal contacts wafer or chip. Spin coat resist layers:
    a. PMGI – 4000 rpm, 1000 rpm/s, 45 s. Hotplate bake 125 °C for 5 min
    b. 1813 – 5000 rpm, 1000 rpm/s, 45 s. Hotplate bake at 115 °C for 2 min
2. Align and expose the graphene-Si/SiO2 wafer with the channel mask. Use Soft Contact Lithography and expose for 140 mJ/cm^2 (for a 50 mW/cm_2 362 nm lamp exposure time is 2.5 sec)
3. Drop into developer (typically MF319) bath and gently agitate. Should develop in ~ 1 min but needs to be monitored
4. Move sample to running DI water bath, swirl gently for 30 s
5. Blow dry with N2
6. Plasma etch to clean graphene excess. 30 sec etch at 50W, oxygen flow is set such that pressure is 125 mTorr

Cleaning

1. Drop sample into a resist remover bath (typically Remover PG or 1165) for 2 min and gently agitate
2. Drop into a fresh remover for 10 min
3. Move sample to Acetone bath for 5 min

4. Rinse with IPA and dry with N2
5. Furnace anneal at 225 °C, 1000 sccm Ar, 250 sccm H2 for 1 h

A.4. CHEMICAL LINKERS

Pyrene Linker

1. Prepare the pyrene solution by weighing 2 mg of 1-Pyrenebutiryc acid N-hydroxysuccinimide ester (pyrene NHS) on a metal weighing dish, dilute with 25 ml of N,N-Dimethylformamide (DMF). Be sure to not use any plastic containers for the solvent
2. Sonicate the pyrene NHS solution for 10 sec to mix well
3. Take one or several annealed graphene FET arrays and place them on the linker solution for a time between 2 h
4. Place on a DMF bath for 5 min
5. Move to an Acetone bath for 5 min
6. Rinse with IPA and dry with N_2

Azide Linker

1. Under orange light (cleanroom recommended) prepare the azide solution by weighing 2mg of 4-Azido-2,3,5,6-tetrafluorobenzoic acid, succinimidyl ester] (azide NHS) on a metal weighing dish, dilute with 20 ml of N,N-

Dimethylformamide (DMF). Be sure to not use any plastic containers for the solvent

2. Sonicate the azide NHS solution for 10 sec to mix well
3. Take an annealed graphene FET chip (or several) and place them on the linker solution
4. Expose using mercury lamp to 3.5 J/cm2 keeping the dose consistent across different runs
5. Place on a DMF bath for 5 min
6. Move to an Acetone bath for 5 min
7. Rinse with IPA and dry with N_2

A.5. PROTEIN IMMOBILIZATION

Antibody Protein

1. Setup the humid chamber by putting a small petri dish bottom and a glass slide inside a large petri dish bottom with cover
2. Place the chips on the glass slide
3. Pipette about 10 μL of antibody (aprox. 20 μg/ml in 0.75mM of Buffer) to each region in the chip
4. Fill the small petri dish bottom with boiling water (careful not to spill any near the chips) and cover the large petri dish, this will keep the relative humidity at 100%. Refill with fresh boiling water every 1 h

5. Let it sit in the antibody solution for a total of 3 h
6. Place on 400 ml of DI water for 5 min
7. Dry with N2, very gently with a small amount of flow and at a steep angle (almost parallel to the chips surface)

Target Protein

1. Setup the humid chamber by putting a small petri dish bottom and a glass slide inside a large petri dish bottom with cover
2. Place the chips on the glass slide
3. Pipette about 5 μL of target (varying concentrations in 0.75mM of Buffer) to each region in the chip
4. Fill the small petri dish bottom with boiling water (careful not to spill any near the chips) and cover the large petri dish, this will keep the relative humidity at 100%
5. Let it sit in the antibody solution for a total of 1 h
6. Place on a 400 ml of DI water for 5 min
7. Dry with N2, very gently with a small amount of flow and at a steep angle (almost parallel to the chips surface)

BIBLIOGRAPHY

1. Lin, C.-Y.; Wu, J.-Y.; Ou, Y.-J.; Chiu, Y.-H.; Lin, M.-F., Magneto-electronic properties of multilayer graphenes. *Physical Chemistry Chemical Physics* **2015,** *17* (39), 26008-26035.

2. Steff Scanning Electron Microscope. https://en.wikipedia.org/wiki/Scanning_electron_microscope.

3. Nanofabrication AFM tip (Atomic Force Microscope). http://www.uwo.ca/fab/resources/Images/SEM/AFMtip.jpg.

4. Goodsell, D. Antibodies. https://pdb101.rcsb.org/motm/21.

5. Wikipedia DNA. https://en.wikipedia.org/wiki/DNA.

6. Song, S. M.; Cho, B. J., Contact resistance in graphene channel transistors. *Carbon letters* **2013,** *14* (3), 1976-4251.

7. Thermo-Fisher Amine-Reactive Crosslinker Chemistry. https://www.thermofisher.com/us/en/home/life-science/protein-biology/protein-biology-learning-center/protein-biology-resource-library/pierce-protein-methods/amine-reactive-crosslinker-chemistry.html.

8. Chua, C. K.; Pumera, M., Covalent chemistry on graphene. *Chemical Society Reviews* **2013,** *42* (8), 3222-3233.

9. Hakkinen, H., The gold-sulfur interface at the nanoscale. *Nat Chem* **2012,** *4* (6), 443-455.

10. Lin, Y.-C.; Lu, C.-C.; Yeh, C.-H.; Jin, C.; Suenaga, K.; Chiu, P.-W., Graphene Annealing: How Clean Can It Be? *Nano Letters* **2012,** *12* (1), 414-419.

11. Bechelany, M.; Maeder, X.; Riesterer, J.; Hankache, J.; Lerose, D.; Christiansen, S.; Michler, J.; Philippe, L., Synthesis Mechanisms of Organized Gold Nanoparticles: Influence of Annealing Temperature and Atmosphere. *Crystal Growth & Design* **2010,** *10* (2), 587-596.

12. Ping, J.; Vishnubhotla, R.; Vrudhula, A.; Johnson, A. T. C., Scalable Production of High-Sensitivity, Label-Free DNA Biosensors Based on Back-Gated Graphene Field Effect Transistors. *ACS Nano* **2016,** *10* (9), 8700-8704.

13. Chen, D. M.; Shenai, P. M.; Zhao, Y., Tight binding description on the band gap opening of pyrene-dispersed graphene. *Phys Chem Chem Phys* **2011,** *13* (4), 1515-20.

14. Malard, L. M.; Pimenta, M. A.; Dresselhaus, G.; Dresselhaus, M. S., Raman spectroscopy in graphene. *Physics Reports* **2009,** *473* (5–6), 51-87.

15. Dong, L.; Tan, Q.; Ye, W.; Liu, D.; Chen, H.; Hu, H.; Wen, D.; Liu, Y.; Cao, Y.; Kang, J.; Fan, J.; Guo, W.; Wu, W., Screening and Identifying a Novel ssDNA Aptamer against Alpha-fetoprotein Using CE-SELEX. *Scientific Reports* **2015,** *5*, 15552.

16. Choi, Y.; Olsen, T. J.; Sims, P. C.; Moody, I. S.; Corso, B. L.; Dang, M. N.; Weiss, G. A.; Collins, P. G., Dissecting Single-Molecule Signal Transduction in Carbon Nanotube Circuits with Protein Engineering. *Nano Letters* **2013,** *13* (2), 625-631.

17. Ho, C.; Robinson, A.; Miller, D.; Davis, M., Overview of Sensors and Needs for Environmental Monitoring. *Sensors* **2005,** *5* (1), 4.

18. Hunter, G. W.; Dweik, R. A., Applied breath analysis: an overview of the challenges and opportunities in developing and testing sensor technology for human health monitoring in aerospace and clinical applications. *J Breath Res* **2008,** *2* (3), 037020.

19. Korhonen, I.; Parkka, J.; van Gils, M., Health monitoring in the home of the future. *IEEE Eng Med Biol Mag* **2003,** *22* (3), 66-73.

20. Lee, T. M.-H., Over-the-Counter Biosensors: Past, Present, and Future. *Sensors (Basel, Switzerland)* **2008,** *8* (9), 5535-5559.

21. Caruthers, M. H., Gene synthesis machines: DNA chemistry and its uses. *Science* **1985,** *230* (4723), 281.

22. Holliger, P.; Hudson, P. J., Engineered antibody fragments and the rise of single domains. *Nat Biotech* **2005,** *23* (9), 1126-1136.

23. Moore, G. P., Genetically engineered antibodies. *Clinical Chemistry* **1989,** *35* (9), 1849.

24. Liu, S.; Guo, X., Carbon nanomaterials field-effect-transistor-based biosensors. *NPG Asia Mater* **2012,** *4*, e23.

25. Otsuji, T.; Tombet, S. A. B.; Satou, A.; Fukidome, H.; Suemitsu, M.; Sano, E.; Popov, V.; Ryzhii, M.; Ryzhii, V., Graphene-based devices in terahertz science and technology. *Journal of Physics D: Applied Physics* **2012,** *45* (30), 303001.

26. Sanchez, F.; Sobolev, K., Nanotechnology in concrete – A review. *Construction and Building Materials* **2010,** *24* (11), 2060-2071.

27. Shao, Y.; Wang, J.; Wu, H.; Liu, J.; Aksay, I. A.; Lin, Y., Graphene Based Electrochemical Sensors and Biosensors: A Review. *Electroanalysis* **2010,** *22* (10), 1027-1036.

28. Novoselov, K. S.; Geim, A. K.; Morozov, S. V.; Jiang, D.; Zhang, Y.; Dubonos, S. V.; Grigorieva, I. V.; Firsov, A. A., Electric Field Effect in Atomically Thin Carbon Films. *Science* **2004,** *306* (5696), 666.

29. Bolotin, K. I.; Sikes, K. J.; Hone, J.; Stormer, H. L.; Kim, P., Temperature-Dependent Transport in Suspended Graphene. *Physical Review Letters* **2008,** *101* (9), 096802.

30. Bolotin, K. I.; Sikes, K. J.; Jiang, Z.; Klima, M.; Fudenberg, G.; Hone, J.; Kim, P.; Stormer, H. L., Ultrahigh electron mobility in suspended graphene. *Solid State Communications* **2008,** *146* (9–10), 351-355.

31. Lee, C.; Wei, X.; Kysar, J. W.; Hone, J., Measurement of the Elastic Properties and Intrinsic Strength of Monolayer Graphene. *Science* **2008,** *321* (5887), 385.

32. Boisen, A.; Thaysen, J.; Jensenius, H.; Hansen, O., Environmental sensors based on micromachined cantilevers with integrated read-out. *Ultramicroscopy* **2000,** *82* (1–4), 11-16.

33. Culler, D.; Estrin, D.; Srivastava, M., Guest Editors' Introduction: Overview of Sensor Networks. *Computer* **2004,** *37* (8), 41-49.

34. Engin, M.; Demirel, A.; Engin, E. Z.; Fedakar, M., Recent developments and trends in biomedical sensors. *Measurement* **2005,** *37* (2), 173-188.

35. Kruss, S.; Hilmer, A. J.; Zhang, J.; Reuel, N. F.; Mu, B.; Strano, M. S., Carbon nanotubes as optical biomedical sensors. *Advanced Drug Delivery Reviews* **2013,** *65* (15), 1933-1950.

36. Walker, P. L.; Radovic, L. R., Chemistry and physics of carbon. M. Dekker etc. CRC Press: New York etc. Boca Raton, FL, 1965; p v.

37. Geim, A. K.; Novoselov, K. S., The rise of graphene. *Nat Mater* **2007,** *6* (3), 183-191.

38. Wallace, P. R., The Band Theory of Graphite. *Physical Review* **1947,** *71* (9), 622-634.

39. Reich, S.; Maultzsch, J.; Thomsen, C.; Ordejón, P., Tight-binding description of graphene. *Physical Review B* **2002,** *66* (3), 035412.

40. Mintmire, J. W.; White, C. T., Electronic and structural properties of carbon nanotubes. *Carbon* **1995,** *33* (7), 893-902.

41. Wilder, J. W. G.; Venema, L. C.; Rinzler, A. G.; Smalley, R. E.; Dekker, C., Electronic structure of atomically resolved carbon nanotubes. *Nature* **1998,** *391* (6662), 59-62.

42. Koswatta, S. O.; Valdes-Garcia, A.; Steiner, M. B.; Lin, Y. M.; Avouris, P., Ultimate RF Performance Potential of Carbon Electronics. *IEEE Transactions on Microwave Theory and Techniques* **2011,** *59* (10), 2739-2750.

43. Novoselov, K. S.; Falko, V. I.; Colombo, L.; Gellert, P. R.; Schwab, M. G.; Kim, K., A roadmap for graphene. *Nature* **2012,** *490* (7419), 192-200.

44. Meric, I.; Han, M. Y.; Young, A. F.; Ozyilmaz, B.; Kim, P.; Shepard, K. L., Current saturation in zero-bandgap, top-gated graphene field-effect transistors. *Nat Nano* **2008,** *3* (11), 654-659.

45. Kim, S.; Nah, J.; Jo, I.; Shahrjerdi, D.; Colombo, L.; Yao, Z.; Tutuc, E.; Banerjee, S. K., Realization of a high mobility dual-gated graphene field-effect transistor with Al2O3 dielectric. *Applied Physics Letters* **2009,** *94* (6), 062107.

46. Tiras, E.; Ardali, S.; Tiras, T.; Arslan, E.; Cakmakyapan, S.; Kazar, O.; Hassan, J.; Janzén, E.; Ozbay, E., Effective mass of electron in monolayer graphene: Electron-phonon interaction. *Journal of Applied Physics* **2013,** *113* (4), 043708.

47. Morozov, S. V.; Novoselov, K. S.; Katsnelson, M. I.; Schedin, F.; Elias, D. C.; Jaszczak, J. A.; Geim, A. K., Giant Intrinsic Carrier Mobilities in Graphene and Its Bilayer. *Physical Review Letters* **2008,** *100* (1), 016602.

48. Chen, J.-H.; Jang, C.; Xiao, S.; Ishigami, M.; Fuhrer, M. S., Intrinsic and extrinsic performance limits of graphene devices on SiO2. *Nat Nano* **2008,** *3* (4), 206-209.

49. Castro, E. V.; Ochoa, H.; Katsnelson, M. I.; Gorbachev, R. V.; Elias, D. C.; Novoselov, K. S.; Geim, A. K.; Guinea, F., Limits on Charge Carrier Mobility in Suspended Graphene due to Flexural Phonons. *Physical Review Letters* **2010,** *105* (26), 266601.

50. Dean, C. R.; Young, A. F.; MericI; LeeC; WangL; SorgenfreiS; WatanabeK; TaniguchiT; KimP; Shepard, K. L.; HoneJ, Boron nitride substrates for high-quality graphene electronics. *Nat Nano* **2010,** *5* (10), 722-726.

51. Lu, Y.; Goldsmith, B. R.; Kybert, N. J.; Johnson, A. T. C., DNA-decorated graphene chemical sensors. *Applied Physics Letters* **2010,** *97* (8), 083107.

52. Dean, C.; Young, A. F.; Wang, L.; Meric, I.; Lee, G. H.; Watanabe, K.; Taniguchi, T.; Shepard, K.; Kim, P.; Hone, J., Graphene based heterostructures. *Solid State Communications* **2012,** *152* (15), 1275-1282.

53. Pedroni, V. A., *Digital electronics and design with VHDL*. 1st ed.; Elsevier: 2008.

54. Russo, S.; Craciun, M. F.; Yamamoto, M.; Morpurgo, A. F.; Tarucha, S., Contact resistance in graphene-based devices. *Physica E: Low-dimensional Systems and Nanostructures* **2010,** *42* (4), 677-679.

55. Huard, B.; Stander, N.; Sulpizio, J. A.; Goldhaber-Gordon, D., Evidence of the role of contacts on the observed electron-hole asymmetry in graphene. *Physical Review B* **2008,** *78* (12), 121402.

56. Kosuke, N.; Akira, T., Density-of-States Limited Contact Resistance in Graphene Field-Effect Transistors. *Japanese Journal of Applied Physics* **2011,** *50* (7R), 070108.

57. Song, S. M.; Park, J. K.; Sul, O. J.; Cho, B. J., Determination of Work Function of Graphene under a Metal Electrode and Its Role in Contact Resistance. *Nano Letters* **2012,** *12* (8), 3887-3892.

58. Low, T.; Hong, S.; Appenzeller, J.; Datta, S.; Lundstrom, M. S., Conductance Asymmetry of Graphene p-n Junction. *IEEE Transactions on Electron Devices* **2009,** *56* (6), 1292-1299.

59. Slabaugh, M. R.; Seager, S. L., *Organic and Biochemistry for Today*. 6th ed.; Brooks Cole: Pacific Grove, 2007.

60. Vo-Dinh, T.; Tromberg, B. J.; Griffin, G. D.; Ambrose, K. R.; Sepaniak, M. J.; Gardenhire, E. M., Antibody-Based Fiberoptics Biosensor for the Carcinogen Benzo(a)pyrene. *Applied Spectroscopy* **1987,** *41* (5), 735-738.

61. Ekins, R.; Chu, F.; Biggart, E., Multispot, multianalyte, immunoassay. *Ann Biol Clin (Paris)* **1990,** *48* (9), 655-666.

62. Goldman, E. R.; Medintz, I. L.; Whitley, J. L.; Hayhurst, A.; Clapp, A. R.; Uyeda, H. T.; Deschamps, J. R.; Lassman, M. E.; Mattoussi, H., A Hybrid Quantum Dot−Antibody Fragment Fluorescence Resonance Energy Transfer-Based TNT Sensor. *Journal of the American Chemical Society* **2005,** *127* (18), 6744-6751.

63. Matsushita, M.; Meijler, M. M.; Wirsching, P.; Lerner, R. A.; Janda, K. D., A Blue Fluorescent Antibody−Cofactor Sensor for Mercury. *Organic Letters* **2005,** *7* (22), 4943-4946.

64. Murphy, K.; Weaver, C., *Janeway's Immunobiology*. 9th ed.; Garland Science: 2016.

65. Litman, G. W.; Rast, J. P.; Shamblott, M. J.; Haire, R. N.; Hulst, M.; Roess, W.; Litman, R. T.; Hinds-Frey, K. R.; Zilch, A.; Amemiya, C. T., Phylogenetic diversification of immunoglobulin genes and the antibody repertoire. *Mol Biol Evol* **1993,** *10* (1), 60-72.

66. Peterson, E.; Owens, S. M.; Henry, R. L., Monoclonal antibody form and function: manufacturing the right antibodies for treating drug abuse. *AAPS J* **2006,** *8* (2), E383-90.

67. Promab Custom Monoclonal Antibody Service. http://www.promab.com/index.php?main_page=page&id=56.

68. Masel, R., *Principles of Adsorption and Reaction on Solid Surfaces*. 1st ed.; Wiley-Interscience: 1996.

69. Langmuir, I., THE ADSORPTION OF GASES ON PLANE SURFACES OF GLASS, MICA AND PLATINUM. *Journal of the American Chemical Society* **1918,** *40* (9), 1361-1403.

70. Hill, A. V., PROCEEDINGS OF THE PHYSIOLOGICAL SOCIETY: January 22, 1910. *The Journal of Physiology* **1910,** *40* (suppl), i-vii.

71. Heller, I.; Janssens, A. M.; Männik, J.; Minot, E. D.; Lemay, S. G.; Dekker, C., Identifying the Mechanism of Biosensing with Carbon Nanotube Transistors. *Nano Letters* **2008,** *8* (2), 591-595.

72. Binnig, G.; Quate, C. F.; Gerber, C., Atomic Force Microscope. *Physical Review Letters* **1986,** *56* (9), 930-933.

73. García, R.; San Paulo, A., Attractive and repulsive tip-sample interaction regimes in tapping-mode atomic force microscopy. *Physical Review B* **1999,** *60* (7), 4961-4967.

74. West, P.; Starostina, N., Atomic force microscopy. *ADVANCED MATERIALS AND PROCESSES* **2004,** *ol.162* (.2), 35-37.

75. Smith, K. C. A.; Oatley, C. W., The scanning electron microscope and its fields of application. *British Journal of Applied Physics* **1955,** *6* (11), 391.

76. Swartz, W. E., X-ray photoelectron spectroscopy. *Analytical Chemistry* **1973,** *45* (9), 788A-800a.

77. Hollander, J. M.; Jolly, W. L., X-ray photoelectron spectroscopy. *Accounts of Chemical Research* **1970,** *3* (6), 193-200.

78. Streller, F.; Agarwal, R.; Mangolini, F.; Carpick, R. W., Novel Metal Silicide Thin Films by Design via Controlled Solid-State Diffusion. *Chemistry of Materials* **2015,** *27* (12), 4247-4253.

79. Gardiner, D. J.; Graves, P. R., *Practical Raman Spectroscopy*. Springer Berlin Heidelberg: 1989.

80. Ferrari, A. C.; Meyer, J. C.; Scardaci, V.; Casiraghi, C.; Lazzeri, M.; Mauri, F.; Piscanec, S.; Jiang, D.; Novoselov, K. S.; Roth, S.; Geim, A. K., Raman Spectrum of Graphene and Graphene Layers. *Physical Review Letters* **2006,** *97* (18), 187401.

81. Dresselhaus, M. S.; Jorio, A.; Hofmann, M.; Dresselhaus, G.; Saito, R., Perspectives on Carbon Nanotubes and Graphene Raman Spectroscopy. *Nano Letters* **2010,** *10* (3), 751-758.

82. Park, J. S.; Reina, A.; Saito, R.; Kong, J.; Dresselhaus, G.; Dresselhaus, M. S., G' band Raman spectra of single, double and triple layer graphene. *Carbon* **2009,** *47* (5), 1303-1310.

83. Bhattacharyya, P.; Basu, S., CVD Grown Materials for High Temperature Electronic Devices : A Review. *Transactions of the Indian Ceramic Society* **2011,** *70* (1), 1-9.

84. Vlassiouk, I.; Regmi, M.; Fulvio, P.; Dai, S.; Datskos, P.; Eres, G.; Smirnov, S., Role of Hydrogen in Chemical Vapor Deposition Growth of Large Single-Crystal Graphene. *ACS Nano* **2011,** *5* (7), 6069-6076.

85. Wu, B.; Geng, D.; Xu, Z.; Guo, Y.; Huang, L.; Xue, Y.; Chen, J.; Yu, G.; Liu, Y., Self-organized graphene crystal patterns. *NPG Asia Mater* **2013,** *5*, e36.

86. Luo, Z.; Lu, Y.; Singer, D. W.; Berck, M. E.; Somers, L. A.; Goldsmith, B. R.; Johnson, A. T. C., Effect of Substrate Roughness and Feedstock Concentration on Growth of Wafer-Scale Graphene at Atmospheric Pressure. *Chemistry of Materials* **2011,** *23* (6), 1441-1447.

87. Losurdo, M.; Giangregorio, M. M.; Capezzuto, P.; Bruno, G., Graphene CVD growth on copper and nickel: role of hydrogen in kinetics and structure. *Physical Chemistry Chemical Physics* **2011,** *13* (46), 20836-20843.

88. Ago, H.; Ogawa, Y.; Tsuji, M.; Mizuno, S.; Hibino, H., Catalytic Growth of Graphene: Toward Large-Area Single-Crystalline Graphene. *The Journal of Physical Chemistry Letters* **2012,** *3* (16), 2228-2236.

89. Li, X.; Cai, W.; An, J.; Kim, S.; Nah, J.; Yang, D.; Piner, R.; Velamakanni, A.; Jung, I.; Tutuc, E.; Banerjee, S. K.; Colombo, L.; Ruoff, R. S., Large-Area Synthesis of High-Quality and Uniform Graphene Films on Copper Foils. *Science* **2009,** *324* (5932), 1312.

90. Yan, Z.; Lin, J.; Peng, Z.; Sun, Z.; Zhu, Y.; Li, L.; Xiang, C.; Samuel, E. L.; Kittrell, C.; Tour, J. M., Toward the Synthesis of Wafer-Scale Single-Crystal Graphene on Copper Foils. *ACS Nano* **2012,** *6* (10), 9110-9117.

91. Reina, A.; Son, H.; Jiao, L.; Fan, B.; Dresselhaus, M. S.; Liu, Z.; Kong, J., Transferring and Identification of Single- and Few-Layer Graphene on Arbitrary Substrates. *The Journal of Physical Chemistry C* **2008,** *112* (46), 17741-17744.

92. Gao, L.; Ren, W.; Xu, H.; Jin, L.; Wang, Z.; Ma, T.; Ma, L.-P.; Zhang, Z.; Fu, Q.; Peng, L.-M.; Bao, X.; Cheng, H.-M., Repeated growth and bubbling transfer of graphene with millimetre-size single-crystal grains using platinum. *Nature Communications* **2012,** *3*, 699.

93. Lafkioti, M.; Krauss, B.; Lohmann, T.; Zschieschang, U.; Klauk, H.; Klitzing, K. v.; Smet, J. H., Graphene on a Hydrophobic Substrate: Doping Reduction and Hysteresis Suppression under Ambient Conditions. *Nano Letters* **2010,** *10* (4), 1149-1153.

94. Clemens, R.; Stefan, H.; Manfred v, S.; Siegfried, H., Laser scanner for direct writing lithography. *Appl. Opt.* **1989,** *28* (17), 3754--3758.

95. Xiao, H., *Introduction to Semiconductor Manufacturing Technology*. 2nd ed.; Spie Press Book: 2012.

96. He, Q.; Wu, S.; Yin, Z.; Zhang, H., Graphene-based electronic sensors. *Chemical Science* **2012,** *3* (6), 1764-1772.

97. Shi, R.; Xu, H.; Chen, B.; Zhang, Z.; Peng, L.-M., Scalable fabrication of graphene devices through photolithography. *Applied Physics Letters* **2013,** *102* (11), 113102.

98. Tung, V. C.; Allen, M. J.; Yang, Y.; Kaner, R. B., High-throughput solution processing of large-scale graphene. *Nat Nano* **2009,** *4* (1), 25-29.

99. Madou, M. J., *Fundamentals of microfabrication : the science of miniaturization.* 2nd ed.; CRC Press: Boca Raton, 2002.

100. Isaac, C.; Luis, A. J.; Jifa, T.; Yong, P. C., Effect of oxygen plasma etching on graphene studied using Raman spectroscopy and electronic transport measurements. *New Journal of Physics* **2011,** *13* (2), 025008.

101. Xie, W.; Weng, L.-T.; Ng, K. M.; Chan, C. K.; Chan, C.-M., Clean graphene surface through high temperature annealing. *Carbon* **2015,** *94*, 740-748.

102. Park, J.; Yan, M., Covalent Functionalization of Graphene with Reactive Intermediates. *Accounts of Chemical Research* **2013,** *46* (1), 181-189.

103. Borden, W. T.; Gritsan, N. P.; Hadad, C. M.; Karney, W. L.; Kemnitz, C. R.; Platz, M. S., The Interplay of Theory and Experiment in the Study of Phenylnitrene. *Accounts of Chemical Research* **2000,** *33* (11), 765-771.

104. Liu, L.-H.; Yan, M., Simple Method for the Covalent Immobilization of Graphene. *Nano Letters* **2009,** *9* (9), 3375-3378.

105. Liu, L.-H.; Yan, M., Functionalization of pristine graphene with perfluorophenyl azides. *Journal of Materials Chemistry* **2011,** *21* (10), 3273-3276.

106. Georgakilas, V.; Tiwari, J. N.; Kemp, K. C.; Perman, J. A.; Bourlinos, A. B.; Kim, K. S.; Zboril, R., Noncovalent Functionalization of Graphene and Graphene Oxide for Energy Materials, Biosensing, Catalytic, and Biomedical Applications. *Chemical Reviews* **2016,** *116* (9), 5464-5519.

107. Li, W.; Zhai, D.; Qiu, H.; Pang, H.; Pan, L.; Shi, Y., Self-assembly Synthesis of High-density Platinum Nanoparticles on Chemically Reduced Graphene Sheets. *Chemistry Letters* **2010,** *40* (1), 104-105.

108. Venkataraman, L.; Klare, J. E.; Tam, I. W.; Nuckolls, C.; Hybertsen, M. S.; Steigerwald, M. L., Single-Molecule Circuits with Well-Defined Molecular Conductance. *Nano Letters* **2006,** *6* (3), 458-462.

109. Pyykko, P., Relativistic effects in structural chemistry. *Chemical Reviews* **1988,** *88* (3), 563-594.

110. Ou, Y.-Y.; Huang, M. H., High-Density Assembly of Gold Nanoparticles on Multiwalled Carbon Nanotubes Using 1-Pyrenemethylamine as Interlinker. *The Journal of Physical Chemistry B* **2006,** *110* (5), 2031-2036.

111. Luo, X.; Morrin, A.; Killard, A. J.; Smyth, M. R., Application of Nanoparticles in Electrochemical Sensors and Biosensors. *Electroanalysis* **2006,** *18* (4), 319-326.

112. Mao, S.; Lu, G.; Yu, K.; Bo, Z.; Chen, J., Specific Protein Detection Using Thermally Reduced Graphene Oxide Sheet Decorated with Gold Nanoparticle-Antibody Conjugates. *Advanced Materials* **2010,** *22* (32), 3521-3526.

113. Abraham, S.; Nirala, N. R.; Pandey, S.; Srivastava, M.; Srivastava, S.; Walkenfort, B.; Srivastava, A., Functional graphene-gold nanoparticle hybrid system for enhanced electrochemical biosensing of free cholesterol. *Analytical Methods* **2015,** *7* (9), 3993-4002.

114. Turcheniuk, K.; Boukherroub, R.; Szunerits, S., Gold-graphene nanocomposites for sensing and biomedical applications. *Journal of Materials Chemistry B* **2015,** *3* (21), 4301-4324.

115. Dong, X.; Shi, Y.; Huang, W.; Chen, P.; Li, L.-J., Electrical Detection of DNA Hybridization with Single-Base Specificity Using Transistors Based on CVD-Grown Graphene Sheets. *Advanced Materials* **2010,** *22* (14), 1649-1653.

116. Yin, Z.; He, Q.; Huang, X.; Zhang, J.; Wu, S.; Chen, P.; Lu, G.; Zhang, Q.; Yan, Q.; Zhang, H., Real-time DNA detection using Pt nanoparticle-decorated reduced graphene oxide field-effect transistors. *Nanoscale* **2012,** *4* (1), 293-297.

117. Cai, B.; Huang, L.; Zhang, H.; Sun, Z.; Zhang, Z.; Zhang, G.-J., Gold nanoparticles-decorated graphene field-effect transistor biosensor for femtomolar MicroRNA detection. *Biosensors and Bioelectronics* **2015,** *74*, 329-334.

118. Zhang, H.; Wang, Y.; Zhao, D.; Zeng, D.; Xia, J.; Aldalbahi, A.; Wang, C.; San, L.; Fan, C.; Zuo, X.; Mi, X., Universal Fluorescence Biosensor Platform Based on Graphene Quantum Dots and Pyrene-Functionalized Molecular Beacons for Detection of MicroRNAs. *ACS Applied Materials & Interfaces* **2015,** *7* (30), 16152-16156.

119. Cai, B.; Wang, S.; Huang, L.; Ning, Y.; Zhang, Z.; Zhang, G.-J., Ultrasensitive Label-Free Detection of PNA–DNA Hybridization by Reduced Graphene Oxide Field-Effect Transistor Biosensor. *ACS Nano* **2014,** *8* (3), 2632-2638.

120. Lerner, M. B.; Matsunaga, F.; Han, G. H.; Hong, S. J.; Xi, J.; Crook, A.; Perez-Aguilar, J. M.; Park, Y. W.; Saven, J. G.; Liu, R.; Johnson, A. T. C., Scalable Production

of Highly Sensitive Nanosensors Based on Graphene Functionalized with a Designed G Protein-Coupled Receptor. *Nano Lett.* **2014,** *14* (5), 2709-2714.

121. Xu, G.; Abbott, J.; Qin, L.; Yeung, K. Y. M.; Song, Y.; Yoon, H.; Kong, J.; Ham, D., Electrophoretic and field-effect graphene for all-electrical DNA array technology. *Nat Commun* **2014,** *5*.

122. Yin, P. T.; Shah, S.; Chhowalla, M.; Lee, K.-B., Design, Synthesis, and Characterization of Graphene–Nanoparticle Hybrid Materials for Bioapplications. *Chemical Reviews* **2015,** *115* (7), 2483-2531.

123. Dong, X.; Huang, W.; Chen, P., In Situ Synthesis of Reduced Graphene Oxide and Gold Nanocomposites for Nanoelectronics and Biosensing. *Nanoscale Res Lett* **2010,** *6* (1), 1-6.

124. Huang, X.; Yin, Z.; Wu, S.; Qi, X.; He, Q.; Zhang, Q.; Yan, Q.; Boey, F.; Zhang, H., Graphene-Based Materials: Synthesis, Characterization, Properties, and Applications. *Small* **2011,** *7* (14), 1876-1902.

125. Gao, Z.; Kang, H.; Naylor, C. H.; Streller, F.; Ducos, P.; Serrano, M. D.; Ping, J.; Zauberman, J.; Rajesh; Carpick, R. W.; Wang, Y.-J.; Park, Y. W.; Luo, Z.; Ren, L.; Johnson, A. T. C., Scalable Production of Sensor Arrays Based on High-Mobility Hybrid Graphene Field Effect Transistors. *ACS Applied Materials & Interfaces* **2016,** *8* (41), 27546-27552.

126. Khamis, S. M.; Jones, R. A.; Johnson, A. T. C., Optimized photolithographic fabrication process for carbon nanotube devices. *Aip Advances* **2011,** *1* (2).

127. Luo, Z.; Somers, L. A.; Dan, Y.; Ly, T.; Kybert, N. J.; Mele, E. J.; Johnson, A. T. C., Size-Selective Nanoparticle Growth on Few-Layer Graphene Films. *Nano Letters* **2010,** *10* (3), 777-781.

128. Mangolini, F.; Åhlund, J.; Wabiszewski, G. E.; Adiga, V. P.; Egberts, P.; Streller, F.; Backlund, K.; Karlsson, P. G.; Wannberg, B.; Carpick, R. W., Angle-resolved environmental X-ray photoelectron spectroscopy: A new laboratory setup for photoemission studies at pressures up to 0.4 Torr. *Review of Scientific Instruments* **2012,** *83* (9), 093112.

129. Hurst, S. J.; Lytton-Jean, A. K. R.; Mirkin, C. A., Maximizing DNA Loading on a Range of Gold Nanoparticle Sizes. *Analytical Chemistry* **2006,** *78* (24), 8313-8318.

130. Heller, I.; Janssens, A. M.; Männik, J.; Minot, E. D.; Lemay, S. G.; Dekker, C., Identifying the mechanism of biosensing with carbon nanotube transistors. *Nano Lett.* **2008,** *8*, 591-595.

131. Chen, F.; Xia, J.; Ferry, D. K.; Tao, N., Dielectric Screening Enhanced Performance in Graphene FET. *Nano Letters* **2009,** *9* (7), 2571-2574.

132. Ping, J.; Xi, J.; Saven, J. G.; Liu, R.; Johnson, A. T. C., Quantifying the effect of ionic screening on protein-decorated graphene transistors. *Biosensors and Bioelectronics* **2015,** *in press*.

133. Yumitori, S., Correlation of C1s chemical state intensities with the O1s intensity in the XPS analysis of anodically oxidized glass-like carbon samples. *Journal of Materials Science* **2000,** *35* (1), 139-146.

134. Tournus, F.; Charlier, J. C., Ab initio study of benzene adsorption on carbon nanotubes. *Physical Review B* **2005,** *71* (16), 165421.

135. Liang, X.; Sperling, B. A.; Calizo, I.; Cheng, G.; Hacker, C. A.; Zhang, Q.; Obeng, Y.; Yan, K.; Peng, H.; Li, Q.; Zhu, X.; Yuan, H.; Hight Walker, A. R.; Liu, Z.; Peng, L.-m.; Richter, C. A., Toward Clean and Crackless Transfer of Graphene. *ACS Nano* **2011,** *5* (11), 9144-9153.

136. Wu, Y.; Jiang, W.; Ren, Y.; Cai, W.; Lee, W. H.; Li, H.; Piner, R. D.; Pope, C. W.; Hao, Y.; Ji, H.; Kang, J.; Ruoff, R. S., Tuning the Doping Type and Level of Graphene with Different Gold Configurations. *Small* **2012,** *8* (20), 3129-3136.

137. Shan, B.; Cho, K., First Principles Study of Work Functions of Single Wall Carbon Nanotubes. *Physical Review Letters* **2005,** *94* (23), 236602.

138. Johnson, R. R.; Johnson, A. T.; Klein, M. L., The nature of DNA base-carbon nanotube interactions. *Small* **2010,** *6*, 31-34.

139. Kybert, N. J.; Han, G. H.; Lerner, M. B.; Dattoli, E. N.; Esfandiar, A.; Johnson, A. T. C., Scalable arrays of chemical vapor sensors based on DNA-decorated graphene. *Nano Research* **2014,** *7* (1), 95-103.

140. Chen, R. J.; Bangsaruntip, S.; Drouvalakis, K. A.; Wong Shi Kam, N.; Shim, M.; Li, Y.; Kim, W.; Utz, P. J.; Dai, H., Noncovalent functionalization of carbon nanotubes for highly specific electronic biosensors. *Proceedings of the National Academy of Sciences* **2003,** *100* (9), 4984-4989.

141. Park, S.; Mohanty, N.; Suk, J. W.; Nagaraja, A.; An, J.; Piner, R. D.; Cai, W.; Dreyer, D. R.; Berry, V.; Ruoff, R. S., Biocompatible, Robust Free-Standing Paper Composed of a TWEEN/Graphene Composite. *Advanced Materials* **2010,** *22* (15), 1736-1740.

142. Lerner, M. B.; Resczenski, J. M.; Amin, A.; Johnson, R. R.; Goldsmith, J. I.; Johnson, A. T. C., Toward Quantifying the Electrostatic Transduction Mechanism in Carbon Nanotube Molecular Sensors. *Journal of the American Chemical Society* **2012,** *134* (35), 14318-14321.

143. Okahata, Y.; Kawase, M.; Niikura, K.; Ohtake, F.; Furusawa, H.; Ebara, Y., Kinetic measurements of DNA hybridization on an oligonucleotide-immobilized 27-MHz quartz crystal microbalance. *Analytical Chemistry* **1998,** *70*, 1288-1296.

144. Nelson, B. P.; Grimsrud, T. E.; Liles, M. R.; Goodman, R. M.; Corn, R. M., Surface plasmon resonance imaging measurements of DNA and RNA hybridization adsorption onto DNA microarrays. *Analytical Chemistry* **2001,** *73*, 1-7.

145. Rajesh; Gao, Z.; Vishnubhotla, R.; Ducos, P.; Serrano, M. D.; Ping, J.; Robinson, M. K.; Johnson, A. T. C., Genetically Engineered Antibody Functionalized Platinum Nanoparticles Modified CVD-Graphene Nanohybrid Transistor for the Detection of Breast Cancer Biomarker, HER3. *Advanced Materials Interfaces* **2016,** *3* (17), 1600124-n/a.

146. Brindle, K., New approaches for imaging tumour responses to treatment. *Nat Rev Cancer* **2008,** *8* (2), 94-107.

147. Fass, L., Imaging and cancer: a review. *Mol Oncol* **2008,** *2* (2), 115-52.

148. Mosmann, T., Rapid colorimetric assay for cellular growth and survival: application to proliferation and cytotoxicity assays. *J Immunol Methods* **1983,** *65* (1-2), 55-63.

149. Zhang, J.; Campbell, R. E.; Ting, A. Y.; Tsien, R. Y., Creating new fluorescent probes for cell biology. *Nat Rev Mol Cell Biol* **2002,** *3* (12), 906-18.

150. Cella, L. N.; Chen, W.; Myung, N. V.; Mulchandani, A., Single-Walled Carbon Nanotubes-Based Chemiresistive Affinity Biosensors for Small Molecules: Ultrasensitive Glucose Detection. *Journal of the American Chemical Society* **2010,** *132* (14), 5024-5026.

151. Haneul, Y.; Dong Jun, L.; Dong-guk, C.; Juhun, P.; Ki Wan, N.; Young Tak, C.; Jae Yeol, P.; Xing, C.; Seunghun, H., Magnetically-refreshable receptor platform structures for reusable nano-biosensor chips. *Nanotechnology* **2016,** *27* (4), 045502.

152. Lerner, M. B.; D'Souza, J.; Pazina, T.; Dailey, J.; Goldsmith, B. R.; Robinson, M. K.; Johnson, A. T. C., Hybrids of a Genetically Engineered Antibody and a Carbon Nanotube Transistor for Detection of Prostate Cancer Biomarkers. *ACS Nano* **2012,** *6* (6), 5143-5149.

153. Lerner, M. B.; Dailey, J.; Goldsmith, B. R.; Brisson, D.; Johnson, A. T. C., Detecting Lyme Disease Using Antibody-Functionalized Single-Walled Carbon Nanotube Transistors. *Biosensors & bioelectronics* **2013,** *45*, 163-167.

154. Tang, X.; Bansaruntip, S.; Nakayama, N.; Yenilmez, E.; Chang, Y. L.; Wang, Q., Carbon nanotube DNA sensor and sensing mechanism. *Nano Lett* **2006,** *6* (8), 1632-6.

155. Wei, G.; Xu, F.; Li, Z.; Jandt, K. D., Protein-Promoted Synthesis of Pt Nanoparticles on Carbon Nanotubes for Electrocatalytic Nanohybrids with Enhanced Glucose Sensing. *The Journal of Physical Chemistry C* **2011,** *115* (23), 11453-11460.

156. Mohanty, N.; Berry, V., Graphene-Based Single-Bacterium Resolution Biodevice and DNA Transistor: Interfacing Graphene Derivatives with Nanoscale and Microscale Biocomponents. *Nano Letters* **2008,** *8* (12), 4469-4476.

157. Lu, J.; Do, I.; Drzal, L. T.; Worden, R. M.; Lee, I., Nanometal-Decorated Exfoliated Graphite Nanoplatelet Based Glucose Biosensors with High Sensitivity and Fast Response. *ACS Nano* **2008,** *2* (9), 1825-1832.

158. Mao, S.; Yu, K.; Lu, G.; Chen, J., Highly sensitive protein sensor based on thermally-reduced graphene oxide field-effect transistor. *Nano Research* **2011,** *4* (10), 921.

159. Ohno, Y.; Maehashi, K.; Matsumoto, K., Label-Free Biosensors Based on Aptamer-Modified Graphene Field-Effect Transistors. *Journal of the American Chemical Society* **2010,** *132* (51), 18012-18013.

160. Park, K. H.; Kim, B. H.; Song, S. H.; Kwon, J.; Kong, B. S.; Kang, K.; Jeon, S., Exfoliation of Non-Oxidized Graphene Flakes for Scalable Conductive Film. *Nano Letters* **2012,** *12* (6), 2871-2876.

161. Shin, D.-W.; Lee, H. M.; Yu, S. M.; Lim, K.-S.; Jung, J. H.; Kim, M.-K.; Kim, S.-W.; Han, J.-H.; Ruoff, R. S.; Yoo, J.-B., A Facile Route To Recover Intrinsic Graphene over Large Scale. *ACS Nano* **2012,** *6* (9), 7781-7788.

162. Reina, A.; Jia, X.; Ho, J.; Nezich, D.; Son, H.; Bulovic, V.; Dresselhaus, M. S.; Kong, J., Large Area, Few-Layer Graphene Films on Arbitrary Substrates by Chemical Vapor Deposition. *Nano Letters* **2009,** *9* (1), 30-35.

163. Chen, C.-H.; Lin, C.-T.; Lee, Y.-H.; Liu, K.-K.; Su, C.-Y.; Zhang, W.; Li, L.-J., Electrical Probing of Submicroliter Liquid Using Graphene Strip Transistors Built on a Nanopipette. *Small* **2012,** *8* (1), 43-46.

164. Yin, P. T.; Kim, T.-H.; Choi, J.-W.; Lee, K.-B., Prospects for graphene-nanoparticle-based hybrid sensors. *Physical Chemistry Chemical Physics* **2013,** *15* (31), 12785-12799.

165. Claussen, J. C.; Kumar, A.; Jaroch, D. B.; Khawaja, M. H.; Hibbard, A. B.; Porterfield, D. M.; Fisher, T. S., Nanostructuring Platinum Nanoparticles on Multilayered Graphene Petal Nanosheets for Electrochemical Biosensing. *Advanced Functional Materials* **2012,** *22* (16), 3399-3405.

166. San, B. H.; Kim, J. A.; Kulkarni, A.; Moh, S. H.; Dugasani, S. R.; Subramani, V. K.; Thorat, N. D.; Lee, H. H.; Park, S. H.; Kim, T.; Kim, K. K., Combining Protein-Shelled Platinum Nanoparticles with Graphene to Build a Bionanohybrid Capacitor. *ACS Nano* **2014,** *8* (12), 12120-12129.

167. Vikash, S.; Nitin, K. P.; Ashok, M.; Rajesh, Platinum nanoparticles-single-walled carbon nanotubes hybrid based chemiresistive sensor array for myoglobin detection. *Materials Research Express* **2016,** *3* (3), 035006.

168. Yin, Z.; He, Q.; Huang, X.; Zhang, J.; Wu, S.; Chen, P.; Lu, G.; Chen, P.; Zhang, Q.; Yan, Q.; Zhang, H., Real-time DNA detection using Pt nanoparticle-decorated reduced graphene oxide field-effect transistors. *Nanoscale* **2012,** *4* (1), 293-297.

169. Tao, L.; Lee, J.; Chou, H.; Holt, M.; Ruoff, R. S.; Akinwande, D., Synthesis of High Quality Monolayer Graphene at Reduced Temperature on Hydrogen-Enriched Evaporated Copper (111) Films. *ACS Nano* **2012,** *6* (3), 2319-2325.

170. Wang, Y. y.; Ni, Z. h.; Yu, T.; Shen, Z. X.; Wang, H. m.; Wu, Y. h.; Chen, W.; Shen Wee, A. T., Raman Studies of Monolayer Graphene: The Substrate Effect. *The Journal of Physical Chemistry C* **2008,** *112* (29), 10637-10640.

171. D'Souza, J. W.; Reddy, S.; Goldsmith, L. E.; Shchaveleva, I.; Marks, J. D.; Litwin, S.; Robinson, M. K., Combining Anti-ERBB3 Antibodies Specific for Domain I and Domain III Enhances the Anti-Tumor Activity over the Individual Monoclonal Antibodies. *PLoS ONE* **2014,** *9* (11), e112376.

172. Ma, F.; Zhang, Z.; Jia, H.; Liu, X.; Hao, Y.; Xu, B., Adsorption of cysteine molecule on intrinsic and Pt-doped graphene: A first-principle study. *Journal of Molecular Structure: THEOCHEM* **2010,** *955* (1–3), 134-139.

173. Rajesh; Das, B. K.; Srinives, S.; Mulchandani, A., ZnS nanocrystals decorated single-walled carbon nanotube based chemiresistive label-free DNA sensor. *Applied Physics Letters* **2011,** *98* (1), 013701.

174. Horak, E.; Heitner, T.; Robinson, M. K.; Simmons, H. H.; Garrison, J.; Russeva, M.; Furmanova, P.; Lou, J.; Zhou, Y.; Yuan, Q.-A.; Weiner, L. M.; Adams, G. P.; Marks, J. D., Isolation of scFvs to In Vitro Produced Extracellular Domains of EGFR Family Members. *Cancer Biotherapy and Radiopharmaceuticals* **2005,** *20* (6), 603-613.

175. King, N.; Hittinger, C. T.; Carroll, S. B., Evolution of Key Cell Signaling and Adhesion Protein Families Predates Animal Origins. *Science* **2003,** *301* (5631), 361.

176. Wang, Z.; Huang, P.; Bhirde, A.; Jin, A.; Ma, Y.; Niu, G.; Neamati, N.; Chen, X., A nanoscale graphene oxide-peptide biosensor for real-time specific biomarker detection on the cell surface. *Chemical Communications* **2012,** *48* (78), 9768-9770.

177. Huang, Y.; Dong, X.; Shi, Y.; Li, C. M.; Li, L.-J.; Chen, P., Nanoelectronic biosensors based on CVD grown graphene. *Nanoscale* **2010,** *2* (8), 1485-1488.

178. Tran, P. D.; Le Goff, A.; Heidkamp, J.; Jousselme, B.; Guillet, N.; Palacin, S.; Dau, H.; Fontecave, M.; Artero, V., Noncovalent Modification of Carbon Nanotubes with Pyrene-Functionalized Nickel Complexes: Carbon Monoxide Tolerant Catalysts for Hydrogen Evolution and Uptake. *Angewandte Chemie* **2011,** *123* (6), 1407-1410.

179. Gann, J. P.; Yan, M., A Versatile Method for Grafting Polymers on Nanoparticles. *Langmuir* **2008,** *24* (10), 5319-5323.

180. Liu, L.-H.; Yan, M., Perfluorophenyl Azides: New Applications in Surface Functionalization and Nanomaterial Synthesis. *Accounts of Chemical Research* **2010,** *43* (11), 1434-1443.

181. Wang, H.; Zhang, Y.; Yuan, X.; Chen, Y.; Yan, M., A Universal Protocol for Photochemical Covalent Immobilization of Intact Carbohydrates for the Preparation of Carbohydrate Microarrays. *Bioconjugate Chemistry* **2011,** *22* (1), 26-32.

182. Zheng, G.; Patolsky, F.; Cui, Y.; Wang, W. U.; Lieber, C. M., Multiplexed electrical detection of cancer markers with nanowire sensor arrays. *Nat Biotech* **2005,** *23* (10), 1294-1301.

183. Rosman, C.; Prasad, J.; Neiser, A.; Henkel, A.; Edgar, J.; Sönnichsen, C., Multiplexed Plasmon Sensor for Rapid Label-Free Analyte Detection. *Nano Letters* **2013,** *13* (7), 3243-3247.

184. Castro Neto, A. H.; Guinea, F.; Peres, N. M. R.; Novoselov, K. S.; Geim, A. K., The electronic properties of graphene. *Reviews of Modern Physics* **2009,** *81* (1), 109-162.

185. Stankovich, S.; Dikin, D. A.; Dommett, G. H. B.; Kohlhaas, K. M.; Zimney, E. J.; Stach, E. A.; Piner, R. D.; Nguyen, S. T.; Ruoff, R. S., Graphene-based composite materials. *Nature* **2006,** *442* (7100), 282-286.

186. Kuila, T.; Bose, S.; Khanra, P.; Mishra, A. K.; Kim, N. H.; Lee, J. H., Recent advances in graphene-based biosensors. *Biosensors and Bioelectronics* **2011,** *26* (12), 4637-4648.

187. Schwierz, F., Graphene transistors. *Nat Nano* **2010,** *5* (7), 487-496.

188. Inaba, A.; Yoo, K.; Takei, Y.; Matsumoto, K.; Shimoyama, I., Ammonia gas sensing using a graphene field–effect transistor gated by ionic liquid. *Sensors & Actuators: B. Chemical* **2014,** *195* (Complete), 15-21.

189. Liu, Y.; Dong, X.; Chen, P., Biological and chemical sensors based on graphene materials. *Chemical Society Reviews* **2012,** *41* (6), 2283-2307.

190. Huang, Y.; Dong, X.; Liu, Y.; Li, L.-J.; Chen, P., Graphene-based biosensors for detection of bacteria and their metabolic activities. *Journal of Materials Chemistry* **2011,** *21* (33), 12358-12362.

191. Ahmad, Z. A.; Yeap, S. K.; Ali, A. M.; Ho, W. Y.; Alitheen, N. B. M.; Hamid, M., scFv Antibody: Principles and Clinical Application. *Clinical and Developmental Immunology* **2012,** *2012*, 15.

192. Robinson, M. K.; Hodge, K. M.; Horak, E.; Sundberg, A. L.; Russeva, M.; Shaller, C. C.; von Mehren, M.; Shchaveleva, I.; Simmons, H. H.; Marks, J. D.; Adams, G. P., Targeting ErbB2 and ErbB3 with a bispecific single-chain Fv enhances targeting selectivity and induces a therapeutic effect in vitro. *Br J Cancer* **2008,** *99* (9), 1415-1425.

193. Paulus, G. L. C.; Wang, Q. H.; Strano, M. S., Covalent Electron Transfer Chemistry of Graphene with Diazonium Salts. *Accounts of Chemical Research* **2013,** *46* (1), 160-170.

194. Plachinda, P.; Evans, D.; Solanki, R., Electrical conductivity of PFPA functionalized graphene. *Solid-State Electronics* **2013,** *79*, 262-267.

195. Suggs, K.; Reuven, D.; Wang, X.-Q., Electronic Properties of Cycloaddition-Functionalized Graphene. *The Journal of Physical Chemistry C* **2011,** *115* (8), 3313-3317.

196. Ha, T.-J.; Lee, J.; Chowdhury, S. F.; Akinwande, D.; Rossky, P. J.; Dodabalapur, A., Transformation of the Electrical Characteristics of Graphene Field-Effect Transistors with Fluoropolymer. *ACS Applied Materials & Interfaces* **2013,** *5* (1), 16-20.

197. Shin, W. C.; Seo, S.; Cho, B. J., Highly air-stable electrical performance of graphene field effect transistors by interface engineering with amorphous fluoropolymer. *Applied Physics Letters* **2011,** *98* (15), 153505.

198. Wettschureck, N.; Offermanns, S., Mammalian G Proteins and Their Cell Type Specific Functions. *Physiological Reviews* **2005,** *85* (4), 1159.

199. Kurganov, B. I.; Lobanov, A. V.; Borisov, I. A.; Reshetilov, A. N., Criterion for Hill equation validity for description of biosensor calibration curves. *Analytica Chimica Acta* **2001,** *427* (1), 11-19.

200. Wormser, G. P.; Dattwyler, R. J.; Shapiro, E. D.; Halperin, J. J.; Steere, A. C.; Klempner, M. S.; Krause, P. J.; Bakken, J. S.; Strle, F.; Stanek, G.; Bockenstedt, L.; Fish, D.; Dumler, J. S.; Nadelman, R. B., The Clinical Assessment, Treatment, and Prevention of Lyme Disease, Human Granulocytic Anaplasmosis, and Babesiosis: Clinical Practice Guidelines by the Infectious Diseases Society of America. *Clinical Infectious Diseases* **2006,** *43* (9), 1089-1134.

201. Moore, A.; Nelson, C.; Molins, C.; Mead, P.; Schriefer, M., Current Guidelines, Common Clinical Pitfalls, and Future Directions for Laboratory Diagnosis of Lyme Disease, United States. *Emerging Infectious Diseases* **2016,** *22* (7), 1169-1177.

202. Halpern, M. D.; Molins, C. R.; Schriefer, M.; Jewett, M. W., Simple Objective Detection of Human Lyme Disease Infection Using Immuno-PCR and a Single Recombinant Hybrid Antigen. *Clinical and Vaccine Immunology* **2014,** *21* (8), 1094-1105.

203. Lerner, M. B.; Dailey, J.; Goldsmith, B. R.; Brisson, D.; Johnson, A. T. C., Detecting Lyme disease using antibody-functionalized single-walled carbon nanotube transistors. *Biosensors and Bioelectronics* **2013,** *45*, 163-167.

204. Jang, C.; Adam, S.; Chen, J. H.; Williams, E. D.; Das Sarma, S.; Fuhrer, M. S., Tuning the Effective Fine Structure Constant in Graphene: Opposing Effects of Dielectric Screening on Short- and Long-Range Potential Scattering. *Physical Review Letters* **2008,** *101* (14), 146805.

205. Xia, F.; Perebeinos, V.; Lin, Y.-m.; Wu, Y.; Avouris, P., The origins and limits of metal-graphene junction resistance. *Nat Nano* **2011,** *6* (3), 179-184.

206. Bae, S.; Kim, H.; Lee, Y.; Xu, X.; Park, J.-S.; Zheng, Y.; Balakrishnan, J.; Lei, T.; Ri Kim, H.; Song, Y. I.; Kim, Y.-J.; Kim, K. S.; Ozyilmaz, B.; Ahn, J.-H.; Hong, B. H.; Iijima, S., Roll-to-roll production of 30-inch graphene films for transparent electrodes. *Nat Nano* **2010,** *5* (8), 574-578.

207. Gunho, J.; Minhyeok, C.; Sangchul, L.; Woojin, P.; Yung Ho, K.; Takhee, L., The application of graphene as electrodes in electrical and optical devices. *Nanotechnology* **2012,** *23* (11), 112001.

208. Moon, J. S.; Gaskill, D. K., Graphene: Its Fundamentals to Future Applications. *IEEE Transactions on Microwave Theory and Techniques* **2011,** *59* (10), 2702-2708.

209. Wu, Y. Q.; Farmer, D. B.; Valdes-Garcia, A.; Zhu, W. J.; Jenkins, K. A.; Dimitrakopoulos, C.; Avouris, P.; Lin, Y. M. In *Record high RF performance for epitaxial graphene transistors*, 2011 International Electron Devices Meeting, 5-7 Dec. 2011; 2011; pp 23.8.1-23.8.3.

210. Patchkovskii, S.; Tse, J. S.; Yurchenko, S. N.; Zhechkov, L.; Heine, T.; Seifert, G., Graphene nanostructures as tunable storage media for molecular hydrogen. *Proceedings of the National Academy of Sciences of the United States of America* **2005,** *102* (30), 10439-10444.

211. Wang, G.; Shen, X.; Yao, J.; Park, J., Graphene nanosheets for enhanced lithium storage in lithium ion batteries. *Carbon* **2009,** *47* (8), 2049-2053.

212. Lahiri, I.; Verma, V. P.; Choi, W., An all-graphene based transparent and flexible field emission device. *Carbon* **2011,** *49* (5), 1614-1619.

213. Kumar, S.; McEvoy, N.; Kim, H.-Y.; Lee, K.; Peltekis, N.; Rezvani, E.; Nolan, H.; Weidlich, A.; Daly, R.; Duesberg, G. S., CVD growth and processing of graphene for electronic applications. *physica status solidi (b)* **2011,** *248* (11), 2604-2608.

214. Kim, K. K.; Hsu, A.; Jia, X.; Kim, S. M.; Shi, Y.; Hofmann, M.; Nezich, D.; Rodriguez-Nieva, J. F.; Dresselhaus, M.; Palacios, T.; Kong, J., Synthesis of Monolayer Hexagonal Boron Nitride on Cu Foil Using Chemical Vapor Deposition. *Nano Letters* **2012,** *12* (1), 161-166.

215. Shi, Y.; Hamsen, C.; Jia, X.; Kim, K. K.; Reina, A.; Hofmann, M.; Hsu, A. L.; Zhang, K.; Li, H.; Juang, Z.-Y.; Dresselhaus, M. S.; Li, L.-J.; Kong, J., Synthesis of Few-Layer Hexagonal Boron Nitride Thin Film by Chemical Vapor Deposition. *Nano Letters* **2010,** *10* (10), 4134-4139.

216. Huang, X.; Zeng, Z.; Zhang, H., Metal dichalcogenide nanosheets: preparation, properties and applications. *Chemical Society Reviews* **2013,** *42* (5), 1934-1946.

217. Zhang, Y.; Tan, Y.-W.; Stormer, H. L.; Kim, P., Experimental observation of the quantum Hall effect and Berry's phase in graphene. *Nature* **2005,** *438* (7065), 201-204.

218. Bolotin, K. I.; Ghahari, F.; Shulman, M. D.; Stormer, H. L.; Kim, P., Observation of the fractional quantum Hall effect in graphene. *Nature* **2009,** *462* (7270), 196-199.

219. Dean, C. R.; Young, A. F.; Cadden-Zimansky, P.; Wang, L.; Ren, H.; Watanabe, K.; Taniguchi, T.; Kim, P.; Hone, J.; Shepard, K. L., Multicomponent fractional quantum Hall effect in graphene. *Nat Phys* **2011,** *7* (9), 693-696.

220. Wu, L.; Chu, H. S.; Koh, W. S.; Li, E. P., Highly sensitive graphene biosensors based on surface plasmon resonance. *Opt. Express* **2010,** *18* (14), 14395-14400.

221. Liang, J.; Chen, Z.; Guo, L.; Li, L., Electrochemical sensing of l-histidine based on structure-switching DNAzymes and gold nanoparticle-graphene nanosheet composites. *Chemical Communications* **2011,** *47* (19), 5476-5478.

222. Sun, S.; Wu, P., Competitive surface-enhanced Raman scattering effects in noble metal nanoparticle-decorated graphene sheets. *Physical Chemistry Chemical Physics* **2011,** *13* (47), 21116-21120.

223. Hamaguchi, N.; Ellington, A.; Stanton, M., Aptamer beacons for the direct detection of proteins. *Anal Biochem* **2001,** *294* (2), 126-31.

224. McCauley, T. G.; Hamaguchi, N.; Stanton, M., Aptamer-based biosensor arrays for detection and quantification of biological macromolecules. *Analytical Biochemistry* **2003,** *319* (2), 244-250.

225. Gao, L.; Li, Q.; Li, R.; Yan, L.; Zhou, Y.; Chen, K.; Shi, H., Highly sensitive detection for proteins using graphene oxide-aptamer based sensors. *Nanoscale* **2015,** *7* (25), 10903-10907.

226. Ke, X.; Xenia, M.; Barbara, M. N.; Eugene, Z.; Mitra, D.; Michael, A. S., Graphene- and aptamer-based electrochemical biosensor. *Nanotechnology* **2014,** *25* (20), 205501.

227. So, H.-M.; Park, D.-W.; Chang, H.; Lee, J.-O., Carbon Nanotube Biosensors with Aptamers as Molecular Recognition Elements. In *Carbon Nanotubes: Methods and Protocols*, Balasubramanian, K.; Burghard, M., Eds. Humana Press: Totowa, NJ, 2010; pp 239-249.

228. Gallina, M. E.; Zhou, Y.; Johnson, C. J.; Harris-Birtill, D.; Singh, M.; Zhao, H.; Ma, D.; Cass, T.; Elson, D. S., Aptamer-conjugated, fluorescent gold nanorods as potential cancer theradiagnostic agents. *Materials Science and Engineering: C* **2016,** *59,* 324-332.

229. Mao, X.; Phillips, J. A.; Xu, H.; Tan, W.; Zeng, L.; Liu, G., Aptamer-Nanoparticle Strip Biosensor for Rapid and Sensitive Detection of Cancer Cells. *Analytical chemistry* **2009,** *81* (24), 10013.